BROAD BAND ANTENNA ARRAYS AND NOISE COUPLING FOR RADIO ASTRONOMY

by

JAN PETER PEETERS WEEM

B.S. Mathematics, Oregon State University, 1994

M.S. Applied Mathematics, University of Colorado at Boulder, 1996

A thesis submitted to the
Faculty of the Graduate School of the
University of Colorado in partial fulfillment
of the requirements for the degree of
Doctor of Philosophy
Department of Electrical and Computer Engineering
2001

This thesis entitled:

Broad Band Antenna Arrays and Noise Coupling for Radio Astronomy

written by Jan Peter Peeters Weem

has been approved for the

Department of Electrical and Computer Engineering

Zoya Popović

Edward Kuester

Date

The final copy of this thesis has been examined by the signatories;

and we find that both the content and the form meet acceptable presentation

standards of scholarly work in the above mentioned discipline

Peter Peeters Weem, Jan (Ph.D., Electrical Engineering)

Broad Band Antenna Arrays and Noise Coupling for Radio Astronomy

Thesis directed by Professor Zoya Popović

In radio astronomy radio telescopes that use large spherical or parabolic reflector antennas are often used. They contain cryogenic cooling to lower the noise temperature of the antennas, which makes the antennas expensive to build and maintain. A next generation radio telescope that uses a phased array antenna instead of the reflector type antennas has been proposed. The collecting area of the telescope is proposed to be one square kilometer and the frequency range from 200 MHz to 2 GHz.

There are several advantages to a phased array radio telescope, as well as some potential difficulties that arise in its design. A phased array can have more than one beam, allowing astronomers to view multiple objects at the same time, and using analog and digital beam forming will allow for the active suppression of both mobile and stationary noise sources. Moreover, the large collecting area allows for higher noise temperature of the antenna, while still maintaining a high sensetivity. On the other hand, one disadvantage of the phased array is the potential for noise coupling that occurs when noise generated by LNAs in one antenna element is received by its neighboring elements, adding to the total noise of the telescope.

The first step in the design of the Square Kilometer Array (SKA) is the design of the sub-arrays. The sub-arrays are one square-meter dual polarized antenna arrays with an operating frequency from 200 MHz to 2 GHz. The sub-arrays elements must have broad beamwidth so that the array will have a large scan-angle and a low amount of coupling. The low coupling is important for the scan-impedance of the array, as well as its noise performance. In this thesis several antenna elements are studied, designed and built, including wire; log-periodic; slotline Vivaldi; and

antipodal Vivaldi antennas. A twenty-element sub-array using the antipodal Vivaldi antenna element is designed and fabricated.

Noise coupling in antenna arrays was first observed in the Westerbork Radio Synthesis Telescope (WRST). A higher noise power than was predicted was measured when the antenna was directed at a cold region of the sky. This noise power was attributed to noise coupling between two elements in the feed of the antennas parabolic reflector. In a phased array where all the array elements are placed close together the coupling between them can be large, which will also increase the noise coupling in the array. A detailed analysis of the noise coupling of a phased array is performed. This analysis will lead to an analytical solution for the noise coupling in a phased array.

DEDICATION

Dedication ...

This thesis is dedicated to my wife Lisa and my parents Jan and Liselotte. To my wife — graduate school would not have been possible without her love and support. And to my parents for never once giving up on me and always believing that I could do it.

The contemplation of celestial things will make man both speak and think more sublimely and magnificently when he descends to human affairs.

- Marcus Tullius Cicero

ACKNOWLEDGMENTS

Acknowledgments ... This work would not have been possible without the help and guidance of my advisor Professor Zoya Popović. Her support was both motivational and financial, giving me the ability perform my research in an environment that was always challenging. While I was not an experimentalist when I joined the group- my education was as a mathematician- I feel that I learned to be an engineer under her guidance.

I would like to thank the Netherlands Foundation for Research in Astronomy (NFRA) for their financial support. I would especially like to thank Arnold van Ardenne, Jaap Bergman, Dion Kant and Bart Smolders for all their help. The summer that I spent working in Dwingaloo was very educational and enjoyable.

There are also many members of Zoya's group that I would like to thank for their help, friendship and motivation. I want to thank Manoja Weiss who defended four hours before me, for always listening to my ramblings while working late into the night on our theses. Thanks to Joe Hagerty for despite all our petty bickering still managing to build the antenna chamber with me, with out once dropping a 2×4 on my head. I would like to thank Darko Popović for helping to glue so much absorber, and helping figure out the proper way to measure antenna patterns. For all the great bike rides early in the morning that kept me sane while writing my thesis, thanks to Jason Breitbarth. For all the great conversations about computers, lightning, and everything else I would like to thank Michael Forman, Todd Marshall and Jim Vian. And for keeping the lab a friendly place to work I would like to thank Naoyuki Shino (Nao) and Srdjan Pajic (Paja). A thanks to Paul Smith, the most cheerful person in the lab by about 10 dB. I would like to express my amazement at

the ability of Stefania Römisch for not taking a sledge hammer and smashing her briefcase after so much frustration that it caused. I would like to thank Helen Frey for all her help throughout my time in the electrical engineering department, and I would like to thank Rachael Tearle for her help and for always being cheerful.

I would also like to acknowledge some people from the Applied Mathematics Department. To Brian Bloechle, Rudy Horne, and Travis Austin thanks for the many "super terrific happy hours" that helped me to keep the proper perspective on life. And finally thanks to Markus Berndt, for being my good friend, and brother in-law.

I would like to apologize to any one that I have missed in this brief acknowledgment.

Finally a quote to Coffee, the liquid that made it all possible:

Coffee, which makes the politician wise, And see through all things with his half shut eyes.

- Alexander Pope

CONTENTS

TABLES

TABLE

FIGURES

FIGURE

CHAPTER 1

INTRODUCTION

The work in this thesis addresses several issues related to phased array radio telescopes. The goal of the research is to provide a design for a decade-bandwidth sub-array of antennas integrated with low-noise amplifiers (LNAs). The results of this research include new antenna elements, new array designs and a new theory for noise coupling in very low noise array radio telescopes.

There are two principal transparent bands of the earth's atmosphere: the

Figure 1.1. An artistic conception of a sub-station of the Square Kilometer Radio telescope

optical window, with wave lengths from about $0.4\,\mu$m to $0.8\,\mu$m; and the radio window, from about 1 mm to 150 m [1]. The bandwidth of the optical window is about one octave, while the bandwidth of the radio window is 17 octaves, opening more possibilities for scientific discoveries.

The world's first radio astronomer was Karl G. Jansky, a radio engineer from New Jersey. While trying to find the arrival direction of thunder-storm static, using a vertically polarized antenna array at 20.5 MHz, he found three different sources of static: (1) static from local thunder-storms; (2) static from distant thunder storms; and (3) noise from an unknown source. The unknown source was first thought to be the sun but after further study the origin of the noise was found to be the center of the Milky-way galaxy. This was the first radio-astronomically observed source, and the unit of spectral power density was named after Jansky::

$$1 \text{ Jansky} = 1 \text{ Jy} = \frac{10^{-26}\text{W}}{\text{m}^2\text{Hz}}. \tag{1.1}$$

Ever since the discovery of extraterrestrial radio-waves, astronomers and engineers have used larger aperture antennas with higher sensitivities and larger directivities. Many of the antennas that are used for radioastronomy are reflector antennas, with either parabolic or spherical reflector dishes. The largest of the single antennas is a spherical dish in Arecibo, Puerto Rico, with a diameter of 305 m and a movable feed [1]. To improve the resolution of radio telescopes, interferometers consisting of two or more antennas separated by a distance of several wavelengths are used. One such interferometer telescope is the VLA (Very Large Array) consisting of 27 25-m diameter parabolic dishes arrayed in a Y configuration.

1.1 The Square Kilometer Array

The next generation telescope is envisioned to have a large collecting area of $1\,\text{km}^2$ and is referred to as the Square Kilometer Array (SKA) [2]. This antenna

will have a decade bandwidth (200 MHz-2 GHz) and a collecting area of one square kilometer.

Astronomers want to use SKA for many different types of missions, ranging from imaging the interstellar medium to the detection of gravity waves. One important mission is to detect neutral hydrogen line emission, the so called 21-cm line. Antenna arrays developed in this thesis cover this wavelength. The area of the antenna is chosen to be very large for high sensitivity. The current design goals for SKA are given in the following table:

Quantity	Value
Frequency range	0.2-2 GHz
Beamwidths in two orthogonal planes	1 degree
Instantaneous bandwidth	(0.5 + 0.2 × operating frequency) GHz
Sensitivity	sub microJansky
Dual Polarization	Polarization isolation -20 dB

Currently there are five proposals for the square kilometer array, all actively pursued in the initial research stage.

- A set of large spherical reflectors, each of which can be dynamically shaped to form local parabolic patches, Figure 1.2(a), proposed by the *Beijing Astronomical Observatory.*
- A large, low-profile parabolic reflector of very long focal length, with the receiver supported by an aerostat at the prime focus, Figure 1.2(b), proposed by the *Herzberg Institute of Astrophysics* in Canada.
- An array of steer-able parabolic dishes, Figure 1.2(c), proposed by the *United States SKA consortium.*

- An array of spherical Luneburg lenses, Figure 1.2(d), proposed by the *Australia Telescope National Facility.*
- A fixed planar phased array, Figure 1.1, proposed by the *Netherlands Foundation for Research in Astronomy (NRFA).* This is the type of antenna that was researched for this thesis.

1.2 Antenna Noise and Signal Detection

Because of the extremely low levels of signals received from distant galaxies, noise in the antenna and receiver is a critical parameter in radio telescopes. Noise is often described by temperature, since the noise power of a resistor in a 1 Hz bandwidth is approximated by $P = kT$ at microwave frequencies. The noise temperature of a receiving antenna T_A pointed at a source S is:

$$T_A = \frac{1}{\Omega_A} \int \int T_S(\theta, \phi) P(\theta, \phi) d\Omega, \tag{1.2}$$

where $T_S(\theta, \phi)$ is the source temperature in Kelvin, $P(\theta, \phi)$ is the normalized antenna power pattern, and Ω_A is the antenna beam area (in Steradians), [3]. The temperature of the antenna is a function of the gain of the antenna, as well as the temperature of the source. The total temperature of an operating telescope also includes temperature contributions from sources such as cosmic background (T_{BG}), atmosphere (T_{atm}), temperature from the Amplifiers (T_{LNA}), and noise from the rest of the receiver (T_{rec}). The total noise temperature is the the sum of all the noises:

$$T_{sys} = T_A(T_S) + T_{BG} + T_{atm} + T_{LNA} + \frac{T_{rec}}{G_{LNA}}, \tag{1.3}$$

where G_{LNA}, the gain of the LNA, reduces the noise contribution of T_{rec}. It is important to note that the temperature of the antenna T_A is a function of the source temperature T_S.

The sensitivity of the radio telescope is proportional to the ratio, A_{eff}/T_{sys} where A_{eff} is the effective area of the telescope. From here it can be seen that

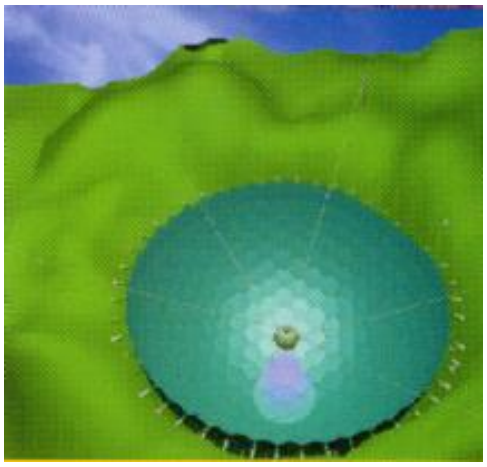

(a)

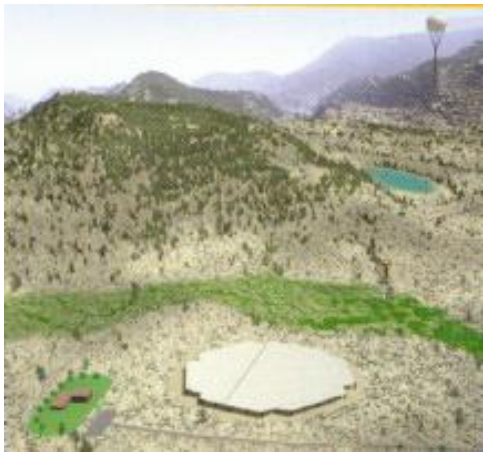

(b)

(c)

(d)

Figure 1.2. artistic conception of the proposed different types of antennas proposed for the Square Kilometer Array. a) large spherical array; b) low-profile parabolic reflector; c) array of steer-able small parabolic dishes; d) array of spherical Luneburg Lenses

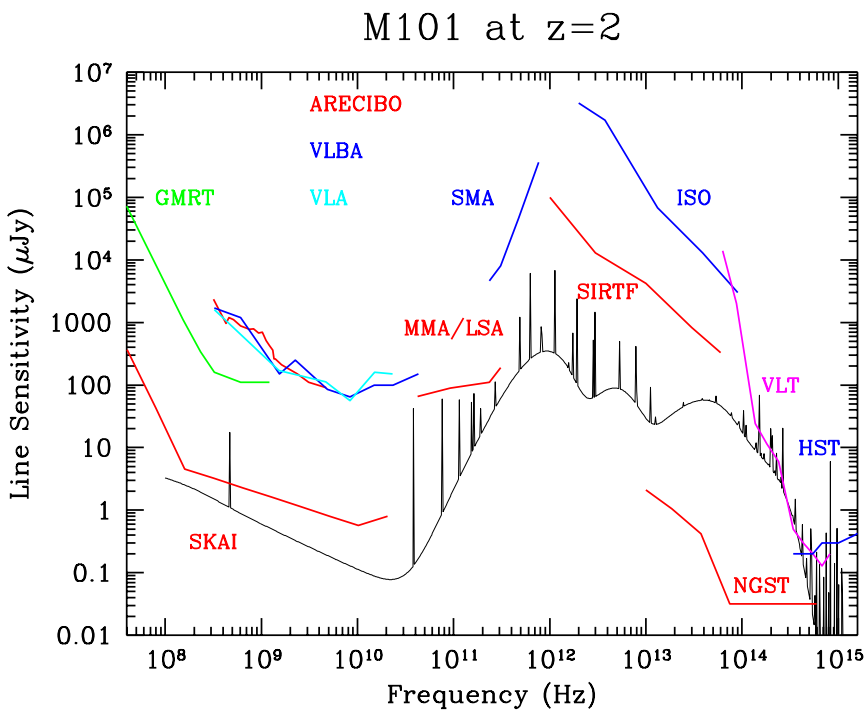

Figure 1.3. An impression of the capabilities of current and future telescopes. The black line is the spectral power from the spiral galaxy M101. The acronyms are as follows: NGST, Next Generation Space Telescope (2008); VLT, Very Large Telescope; ISO, Infrared Space Observatory; SIRTF, Space Infrared Telescope Facility (2002); SMA, Sub Millimeter Array; MMA, MilliMeter Array; LSA, Large Souther Array; VLBA, Very Long Baseline Array; VLA, Very Large Array; GMRT, Giant Meter Radio Telescope. This plot was used with permission from the NFRA.

there are two options for increasing the sensitivity: reducing T_{sys}, or increasing the effective area. Most commonly, radio telescope receivers are operated cryogenically at liquid helium temperatures ($\approx$4 K). The approach in SKA is non-cryogenic, making it imperative to increase the effective area of the antenna.

Figure 1.3 shows the sensitivity of both optical and radio telescopes. The black line in the figure represents the spectral power density from the spiral galaxy M101. The improvement of the proposed SKA telescope is three orders of magnitude over the best telescopes currently available.

1.3 Phased Array SKA

The *Netherlands Foundation for Research in Astronomy*, NFRA, has proposed that a ground-based phased array be used for SKA [2],[4]. The phased array would be comprised of one million one square meter sub-arrays. Each of the sub-arrays must be dual-polarized and operate from 0.2-2.0 GHz. Unlike standard radio astronomy receivers, which are cryogenically cooled to improve noise performance, SKA will operate at *room* temperature (290K). To optimize the noise performance of the antenna array, LNAs will be integrated into each antenna. Room temperature active antennas with noise temperatures as low as 35 K have been studied [5].

Several different types of antennas have been studied for the square meter sub-array. One antenna that has been proposed uses short Vivaldi antennas [6]. These antennas are electrically small, $0.09\lambda_o$ to $0.4\lambda_o$, and are arrayed in an "egg-carton" layout. The bandwidth of this antenna is from 1.3-6.0 GHz. Because the elements are small their radiation pattern is broad. The drawback to having such a small element and element spacing is that there will be high coupling between the elements. There is also a higher cost associated with close element spacing since more LNAs and phase shifters would be required.

1.4 Noise Performance of an Array

In the phased array approach, each antenna element is directly integrated with an LNA. LNAs are characterized by their noise figure, the ratio of the signal to noise ratio (SNR) at the input to the SNR at the output:

$$F = \frac{S_{in}/N_{in}}{S_{out}/N_{out}}, \tag{1.4}$$

where S_{in} is the signal power at the input of an LNA, S_{out} is the signal power at the output, N_{in} is the noise at the input, and N_{out} the noise at the output. When two

LNAs are cascaded, the resulting noise figure of the two is:

$$F_{total} = F_1 + \frac{F_2 - 1}{G_1}, \tag{1.5}$$

where G_1 is the gain of the first LNA, F_1 and F_2 are the noise figures of the first and second LNAs. It can be seen from this equation that the noise of a system is dominated by the noise of the first LNA, since the noise of the second element is reduced by the gain of the first. If the feed line connecting the antenna to the LNA is lossy, then G_1 becomes less then 1 $G_1 < 1$ and the noise figure increases. The optimal location for the LNAs in an antenna is therefore at the feed of the antenna.

One problem that can also occur in a low noise phased array is that of noise coupling. In noise coupling the noise present at the input port of an LNA radiates into the receive antenna. Because of the close spacing of a phased array this noise can be received by neighboring elements and amplified. This amplified noise is then added to the received signal. Since the noise coupling occurs before the gain stage of the first LNA, it has the potential of greatly effecting the total noise performance of the array. This is because the noise coupling value is not reduced by the gain of the LNA.

1.5 Simulation Tools Used

Three different electromagnetic simulation tools were used in the design of the antennas that are presented in this thesis. The first was *WireZeus*, this program simulates wire structures by solving the general *Hallén* type integral equation for the current density vector using the Method of Moments (MoM) with large domain basis functions [7]. A graphical interface for this program was written in *Matlab* to simplify the use of the program, and to improve the graphical output.

The second simulation tool that was used was GEM, General ElectroMagnetic simulator. GEM also uses a Method of Moments (MoM) algorithm to solve the

for the Electric Field Integral Equation (EFIE) for the current density vectors but with different basis functions [8]. GEM can simulate planar structures with arbitrarily shaped dielectric bodies, whereas *WireZeus* is limited to wire structures with only dielectric or magnetic covers and can include distributed or lumped elements. The third simulation tool that was used was IE3D, a commercial sub-domain basis function MoM simulation tool [9].

1.6 Organization of the Thesis

This thesis presents the design, simulation, and fabrication of several types of antenna elements and arrays, along with a theoretical analysis that gives design guidelines for minimizing noise coupling in an active array.

In Chapter 2, several types of dipole arrays are analyzed. Methods of increasing the bandwidths of these arrays are discussed, including an exponential loading of the dipole, as well as a broadband matching network. The concept of fractal spacing of arrays is also introduced.

In Chapter 3 the log-periodic antenna array is introduced. A two level fractal array of log-periodic antennas is simulated. Noise considerations of the log-periodic antenna are analyzed and the optimal location of the LNA is found. A new printed version of the log-periodic antenna is designed, built and tested.

In Chapter 4, the exponentially-tapered slot antenna, or Vivaldi antenna is introduced. The Vivaldi antenna is extremely broadband, with frequency ranges of up to 18:1. Different methods of feeding the antennas were studied and tested.

In Chapter 5, an anti-podal Vivaldi antenna that uses a antipodal-slotline instead of a slotline feed is introduced. This antenna has a broader bandwidth feed then the slotline fed Vivaldi antennas. Four different arrays of the anti-podal antennas were built and tested, including a 20-element two level fractal antenna array.

In Chapter 6, the concept of noise coupling is discussed. A method of simulating the noise coupling using a commercial CAD package Agilent ADS 1.3 is described. This method is found to be unsatisfactory for the prediction of noise coupling. An analytical solution to the noise coupling is then derived. This method includes a way to calculate the noise coupling in a phased array as a function of the scan angle of the main-beam of the array.

In the last chapter, some conclusions and directions for future work are briefly presented.

The contributions of this thesis are:

- A new approach to fractal broabband arrays.
- Several new types of broadband antenna elements and feeds
- A simple analytical theory that proves a direct relationship between the noise coupling in an array and directly measurable quantities, such as Γ_{opt}, R_{min} and NF of the LNA, and $\Gamma(\phi, \theta)$ of the antenna array.

CHAPTER 2

WIRE ANTENNAS

2.1 Introduction

Wire antennas are a class of antennas that are made of conductive wire elements. These antennas can be analyzed using a one dimensional Method of Moments (MoM) simulation for solving the integral equation for the current density vector on the wire elements. Since the current in the equation is one dimensional, using the Method of Moments to analyze wire antennas is extremely efficient, even for a large number of wire elements. Wire antennas also have the benefit of easy integration with lumped loads along the radiating portion of that antenna, as well as ease and cost of fabrication.

2.2 Fractal Array Layout

In a phased array the ideal spacing between array elements for horizon-to-horizon scanning of the main beam is half a wavelength ($\lambda_o/2$) or smaller. A spacing larger than half wavelength can lead to grating lobes in the radiation pattern. Grating lobes are side lobes that have amplitudes as large as the main beam, but directed in a different direction. A broadband antenna array consisting of identical antenna elements with an element spacing (period) of half wavelength at the highest frequency will have a spacing of much less then half a wavelength at the lower frequencies. Having a small element spacing at the low frequencies causes inter element coupling and places a constraint on the physical size of the antenna, with the

size of the antenna being no larger than the spacing. In the square kilometer array, a half wavelength spacing at the highest frequency, 2.0 GHz would be 7.5 cm. If all antenna elements were spaced at this interval, then the electrical length between elements at the low-frequency edge (200 MHz) would be one twentieth of a wavelength ($\lambda_o/20$), the highest frequency.

This small spacing of the antennas at the lower operating frequencies of the antennas would require the use of electrically small antennas, implying poor radiation efficiency [10] and high inter-element coupling [11]. Inter-element coupling can lead to poor noise performance of the array because of noise coupling, as will be discussed in detail in Chapter.6.

One solution to the problem described above is to use a fractal layout for the antenna array, Figure 2.1. Several elements of different sizes are used and placed in a periodic, self-scaling arrangement. In a fractal array several different sized antennas are used so that elements of a certain size are used for only a portion of the bandwidth of the array, this is the same basic idea as for most "frequency-independent" antennas. The spacings of the different antenna elements are then also optimal for each frequency band, with each frequency band having the optimal half wavelength spacing ($\lambda_o/2$). The antennas in a fractal array can in this case be designed to be efficient radiators over their individual frequency bands and coupling can be designed to be low, because the distance between the significant elements is always larger then half a wavelength. In a fractal array, elements of different sizes are placed in an array with small spacing. The smaller elements of the fractal array are in the near-field radiation pattern of the larger elements. These smaller elements will then act as scatterors of the larger antennas. They will also load the larger antennas and possibly affect the impedance bandwidth of the antenna. Care must be taken when designing a fractal array so that the coupling between the elements is minimized and the radiation pattern is not greatly affected.

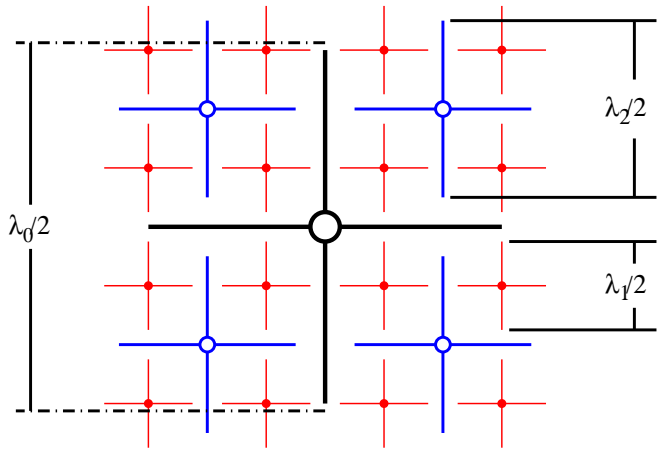

Figure 2.1. A crossed-dipole fractal array layout. The fractal layout offers the maximum antenna size and the optimal antenna spacing for scanning of the array. The antennas are spaced at the optimal spacing for all antenna elements, over a broad bandwidth. The circles represent a dual-polarized feed.

2.3 Dipole Antenna Arrays

A simple example of a dual-polarized fractal array is the crossed dipole array shown in Figure 2.1. A short dipole is essentially a broadband radiator, in the sense that its radiation pattern is uniform over a large frequency range. This is because the current distribution in a dipole is virtually the same for all frequencies where the length of the dipole is less than half a wavelength. The bandwidth of a dipole is limited by the impedance-matched (VSWR) bandwidth. It is difficult to design a broadband match for a short dipole antenna. The power match bandwidth of a dipole is narrow, typically less then 15 % (2:1 VSWR), and can possibly be increased by loading the antennas with reactive loads, designing LNAs to match the impedance of the dipoles or by designing a broadband matching network for the dipoles.

A dual band fractal crossed dipole array above ground was designed using *Wire Zeus*, with a Matlab interface developed specifically for this project. The Matlab interface allows for the fast simulation and optimization of the antenna elements. It also includes extensive visualization software to view radiation patterns, coupling,

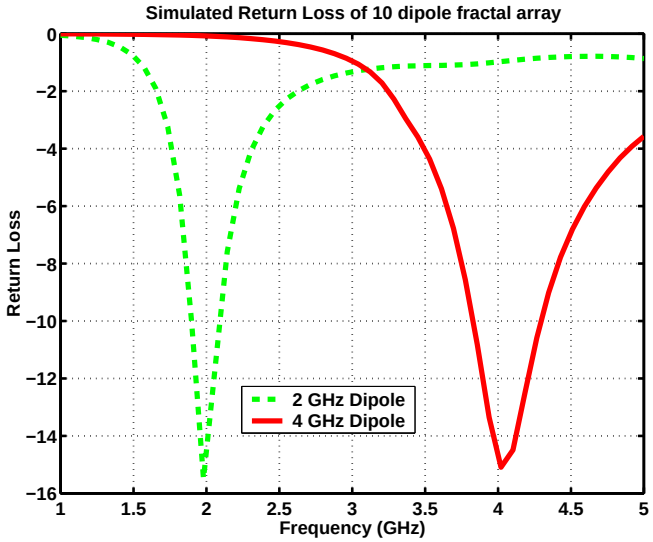

Figure 2.2. The simulated return loss (w.r.t. 50Ω) of the fractal dipole array. The dashed line is the return loss of the larger 2.0 GHz dipole, and the solid line is the return loss of the 4.0 GHz dipole.

insertion loss, and animated current plots.

The operating frequencies were chosen as 2.0 GHz and 4.0 GHz. One 2.0 GHz half wavelength resonant crossed dipole, and four resonant 4.0 GHz crossed dipoles were used in a 10-element array, eight 4.0 GHz dipoles configured in 4 dual-polarized crossed dipole antennas, and two 2.0 GHz crossed dipoles in the center of the array. This array was simulated and optimized using the *Matlab-WireZeus* package. The 10-element array was defined by five parameters: the sizes of the two antennas l_1 and l_2; the heights above the ground plane h_1 and h_2; and the spacing of the smaller antennas d_1. These parameters were then used in a *simplex* [12] optimization routine to find the optimal values, resulting in a low insertion loss for the two frequency bands of the antenna.

A plot of the simulated return loss of the antennas is shown in Figure 2.2. The low frequency dipoles have a -16 dB match at 2.0 GHz, and the small dipoles have a -15 dB match at 4.0 GHz. The coupling between the elements is lower than -15 dB for all the elements.

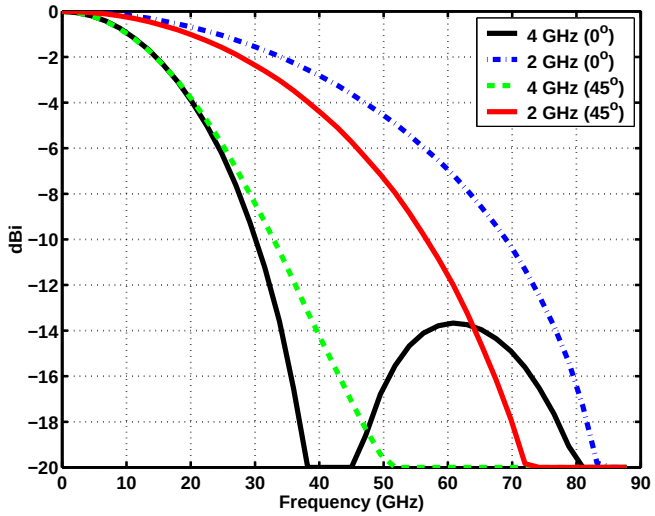

Figure 2.3. Simulated radiation patterns of the fractal crossed dipole array. The array has a dual polarization, so the standard E-plane and H-plane cannot be defined. The increased gain of the 4 GHz pattern is due to the array factor of a four element array

Both frequency ranges have a bandwidth of 10%, 1.9-2.1 GHz for the low-frequency, and 3.8-4.2 GHz for the high-frequency band. The radiation pattern of the array was also calculated at the two different operating frequencies, Figure 2.3. The half power beamwidth of the 2.0 GHz pattern is 86°, the half power beamwidth of the 4.0 GHz antenna is 34°. The gain is larger and the pattern is more directive, for the higher frequency dipoles because the simulation contained 4-elements array in the higher frequency band, increasing the gain because of the array factor of a 2×2 array.

2.4 Loaded Dipoles

Antenna elements in the above fractal array differ in size from elements on a different level in the fractal array by a factor of two. The elements that are used in the fractal array therefore must have a bandwidth of at least 2:1 or 66% in order to preserve the optimal array spacing. It is clear from Figure 2.2 that the power

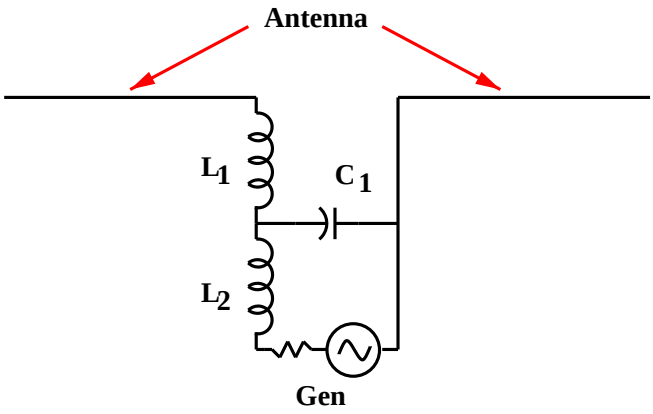

Figure 2.4. A matching network consisting of two inductors and a capacitor. This type of network was able to improve the bandwidth of a dipole antenna. Both inductors and capacitors were used in the optimization of the matching network.

matched bandwidth of the dipole antenna is too small for a fractal array. One way of improving the bandwidth of the dipole arrays is through the use of a broadband matching network, consisting of lumped inductors and capacitors, e.g. as in Figure 2.4. Resistors generate noise, and thus are not used in a low-noise receiving array design and since they are lossy they will lower the gain of an antenna.

The T-network match in Figure 2.4 was designed using *Matlab-WireZeus* and consists of three reactive lumped elements. Lumped elements are easily modeled, and can also be used in the optimization algorithm. An antenna with integrated lumped elements was simulated. The elements were then optimized to minimize the return loss of the antenna. The 2:1 VSWR bandwidth of the dipole without the integrated loads is from 450 MHz to 550 MHz, while the bandwidth of the antenna using the lumped matching network is 500 MHz to 1.8 GHz, Figure 2.5. The increase in bandwidth is from 20% to 120%, a large enough bandwidth for the fractal layout. Lumped matching networks were calculated with capacitors, inductors and a combination of the two. The optimal match was found when two inductors and one capacitor are used, as shown in Figure 2.4. The values of the capacitor and inductors

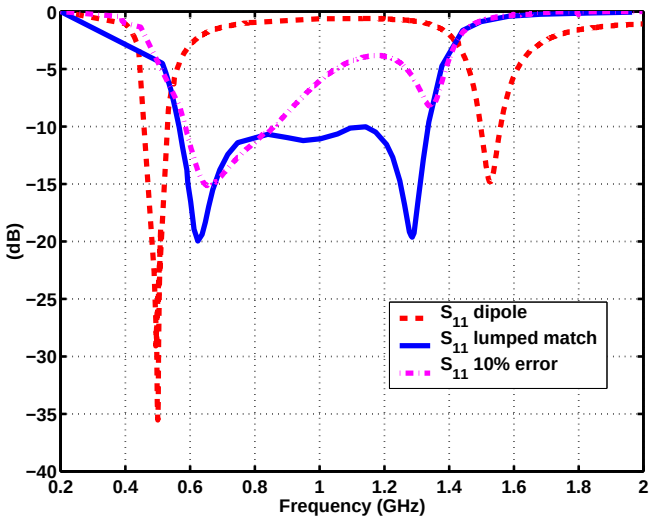

Figure 2.5. The simulated return loss of several dipole antennas. The red dashed line shows the return loss with no broadband matching, the solid blue line shows the return loss with a broadband matching network. The network is very sensitive to the values of the lumped loads, and modifying the values of the loads by as little as 10% changes the bandwidth significantly (purple dot-dashed).

were $L_1 = 41\,\text{nH}$ and $L_2 = 1.15\,\text{nH}$ for the two inductors and $C_1 = 61\,\text{pF}$ for the capacitor. A perturbation analysis of the match showed that it was extremely sensitive to the values of the capacitors, and a change in capacitance of 10% would significantly degrade the match, as shown in Figure 2.5. The error tolerance of typical capacitors or inductors in this range is about 10-20%.

An alternative to increasing the bandwidth of the dipole antenna is to use capacitors and inductors distributed in series along the radiating portion of the antenna [13]. Placing reactive components along the dipole changes the current distribution along the antenna, which changes the input impedance, and therefore the power match at the feed. One method for large improvement in bandwidth is to use distributed impedances, reactances along the radiating arms of the dipole as proposed in [14].

$$Z(x,\omega) = -\frac{j0.3\omega\mu_o}{40\pi}e^{(\beta x)^2}, \tag{2.1}$$

where x is the distance from the center of the dipole, $\omega = 2\pi f$, and $\beta = \omega\sqrt{\epsilon_o\mu_o}$.

As the frequency is increased in Eq.2.1, the inductors limit the current distribution along the antenna, Figure 2.6. This effectively turns off the parts of the dipole which are further than $\lambda_o/4$ away from the feed point of the antenna. In the simulation the continuous loading was replaced with 20 lumped element loads distributed evenly along the dipole. The principle behind this frequency independent antenna is that at the lower frequencies the impedance at the ends of the dipole is low, and the current is able to flow through the entire dipole, Figure 2.6a. At the higher frequencies the impedance at the ends of the dipole becomes large, so that the current at these frequencies is restricted to the center part of the dipole Figure 2.6b. In both figures, the solid lines indicate the real part, and the dashed lines the imaginary part of the current. Since the current distribution is similar to that of a standard dipole, the pattern is the close to that of a dipole.

A two staged crossed dipole layout of the loaded antennas was also modeled using GEM, a Method of Moments electromagnetic simulator [8]. In this simulation there was one large crossed dipole above a ground plane, and four smaller crossed dipoles above elevated ground planes as shown in Figure 2.7. Two different cases were simulated: one with inductive loading as given by Eq.2.1, and one with resistive loading, by Eq.2.1 again but with out the j. The S-parameters are shown in Figure 2.8.

The total bandwidth of the two antennas is from 0.5 to 4.5 GHz. The low-frequency dipole bandwidth is from 0.5 to 1.7 GHz and the high-frequency is from 1.2 to 4.5 GHz. This has an overlap from 1.2 to 1.7 GHz where both antennas work well. Such a large bandwidth over which both antennas work could lead to higher coupling.

Since the loads are frequency dependent, it is not clear as to whether this type of loading can be practically realized using lumped elements. The bandwidth of the loaded fractal array is from 0.5 GHz to 4.5 GHz. The simulations of the array were

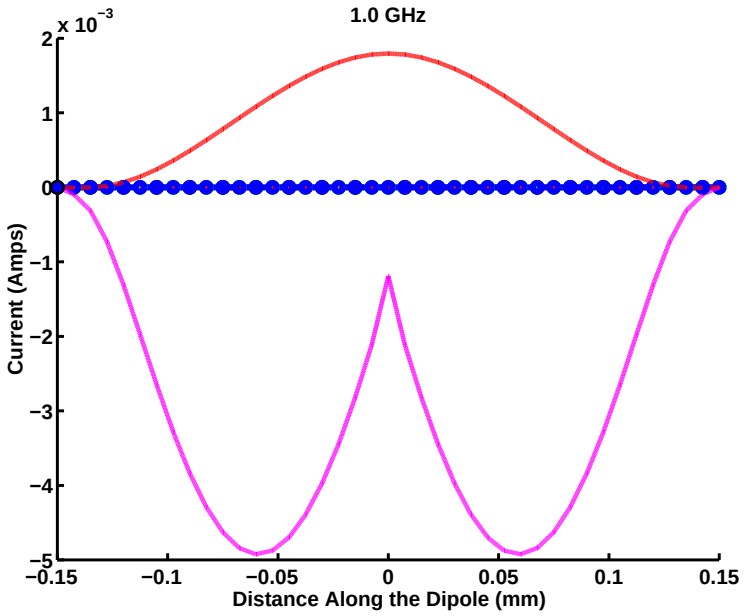

(a)

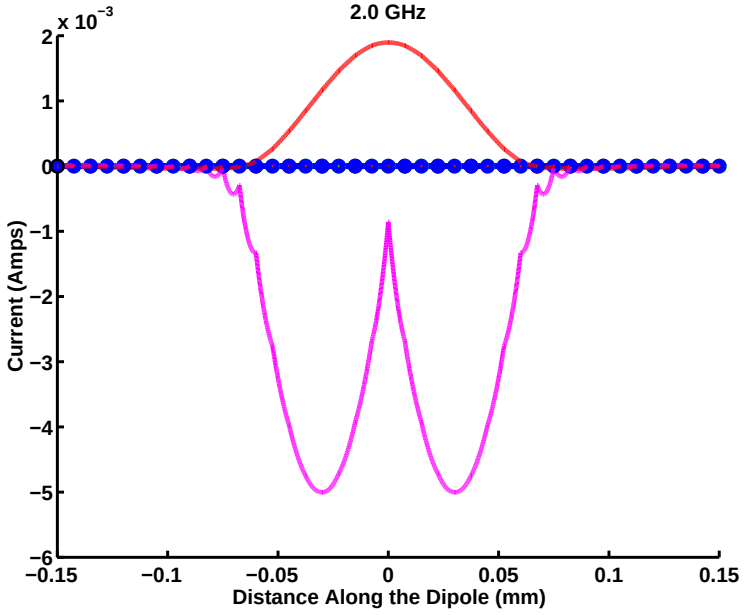

(b)

Figure 2.6. The current distribution on a loaded dipole at (a) 1.0 GHz. and (b) 2.0 GHz. The current is limited at the higher frequencies to the inter-portion of the antenna. The horizontal axis is the location along the dipole in meters. The vertical axis is the current in amps

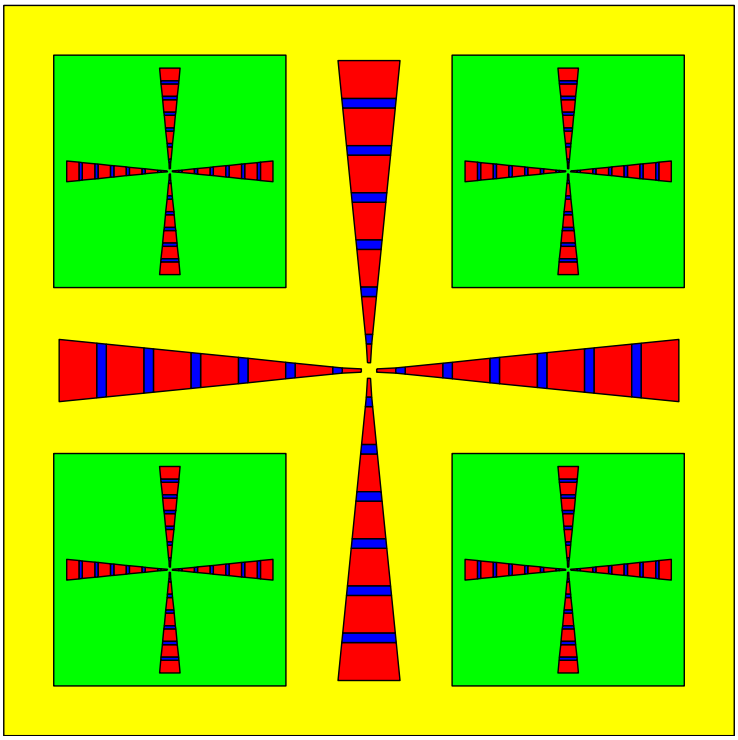

Figure 2.7. Top view of a nested planar horizontal antenna sub-array with horizontal finite ground planes and vertical two-wire feed lines

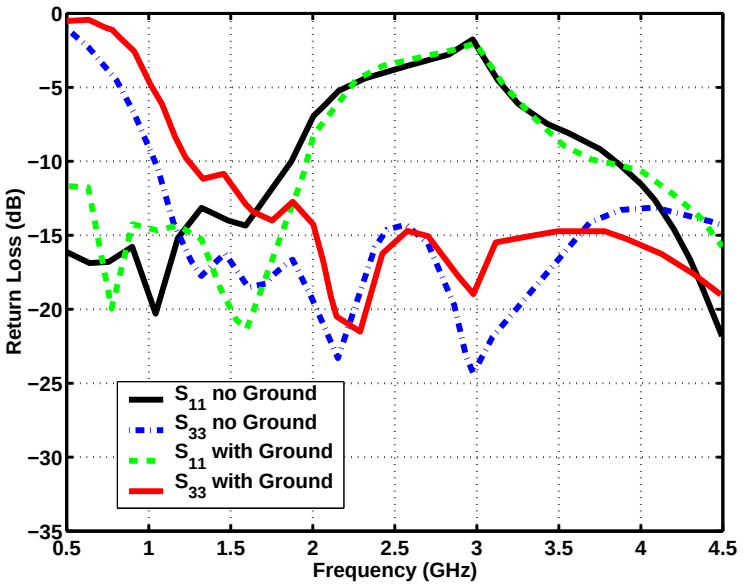

Figure 2.8. The return loss of the loaded fractal array, with and without ground planes. The two elements cover the range from 500 MHz to 4.5 GHz with the low frequency element covering 500-1700 MHz and the high frequency element covering from 1.3 GHz to 4.5 GHz

performed using both *Matlab-WireZeus* as well as *GEM*, General ElectroMagnetic simulator.

2.5 Summary

The use of wire antennas integrated with lumped loads, in either the radiating portion of the antenna or as a matching network has been discussed. Fractal arrays are proposed, and several types of fractal arrays were analyzed. The use of dipole antennas as a candidate for the fractal array was studied. Because of the sensitivity of the loads in the matching network, using the lumped loads was ruled out as an ineffective way to improve the power match of the narrow-band dipole antennas.

CHAPTER 3

LOG-PERIODIC DIPOLE ANTENNAS

3.1 Introduction

Log-periodic antennas are closely related to a class of antennas known as frequency independent antennas. Frequency independent antennas are antennas whose ideal geometry is defined solely by angles. Such antennas have been built in practice with bandwidths up to 40:1 [15]. Spiral and conical antennas are common examples of frequency independent antennas. The bandwidth of frequency independent antennas is theoretically infinite, although in practical applications the lower frequency operation is limited by the size of the antenna, and the upper limit by the feed.

Log-periodic antennas cannot be entirely described by angles, and are therefore not strictly frequency independent, although they can be designed to cover any desired frequency range [16]. In a log-periodic antenna, the physical characteristics of the antenna change in discrete steps, these steps occur logarithmically with frequency. For a given frequency range the antennas properties do not change, however as the frequency range gets too large the structure repeats itself [17]. The period of the repetition is logarithmic with frequency. The frequency range of a logarithmic antenna is determined by the physical size of the antenna.

3.2 Log-Periodic Dipole Antennas

The log-periodic dipole antenna (LPD) has a two-wire feed. To each of these feed lines are connected radiating elements of different lengths and diameters, with

a logarithmic spacing, Figure 3.1. The radiating elements are placed at alternating sides of the feed lines, which produces a 180° phase between adjacent elements. The phases between the adjacent close elements are in opposition. There is also a phase progression so that the energy is radiated in the direction of the small radiating elements. The generator feeding the LPD array is at the vertex of the antenna, the end with the smaller radiating elements, which is also the direction of the main beam of the LPD array. The feed is brought through one of the hollow center conductors, Figure 3.2. The front-to-back ratio of log periodic antenna, is the ratio of the gain at the front of the antenna, to the gain at the back of the antenna. LPDAs can be designed with high front-to-back ratios greater than 20 dB. Such a large front-to-back ratio is a benefit to SKA because it would negate the use of ground-planes. The elimination of ground-planes would be a significant cost saving for SKA.

3.2.1 Noise Performance of an LPD Array This feed provides an ideal way to integrate an LNA into the LPD antenna array. An LNA placed at the feed, would have an optimal noise performance since it minimizes the distance between the radiators and the LNAs especially at the higher frequencies of operation of the antenna. The skin depth in a uniform conductor with a large radius of curvature, is a function of the frequency.

$$\delta_s = \sqrt{\frac{2}{\omega\mu\sigma}}, \tag{3.1}$$

where σ is the conductivity, μ the permeability and $\omega = 2\pi f$. The approximate surface resistance is given by:

$$R_s = \sqrt{\frac{2\pi f\mu}{2\sigma}} \propto \sqrt{f}. \tag{3.2}$$

Since the loss is proportional to the square root of the frequency, so is the noise added to the signal. This is because the noise voltage of a resistor is proportional to the square root of the resistance. The high frequency of operation of the antenna is f_{hi} corresponding to the shortest dipole, and lowest frequency of operation is f_{low},

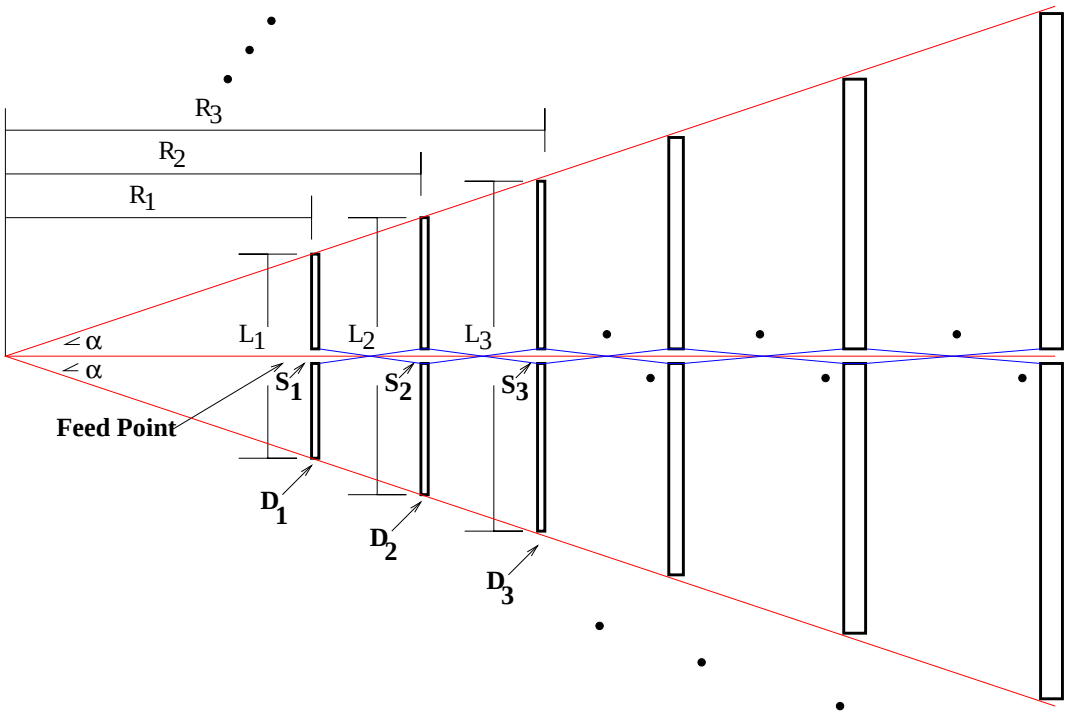

Figure 3.1. A sketch of a log periodic dipole antenna. The parameters in the design of a LPD array are the radiating element lengths L_n, diameters D_n, the distance between radiating elements R_n, and the separation of the feed S_n. The feed lines are crossed to schematically show the alternating phases between neighboring elements.

corresponding to the longest dipole. A wave at frequency f_i will be received primarily by the dipole element with a length closest to the half wavelength of the incident wave, $\lambda_i/2$. Two different antennas will be analyzed, one with a feed at the shortest dipole, the front feed, and one with the feed at the largest dipole, the back feed. The distance from incident point of the wave to the back feed is:

$$l_{low} = \frac{1}{\tan(\alpha)}\left(\frac{\lambda_{low}}{4} - \frac{\lambda_i}{4}\right) = \frac{c}{4\tan(\alpha)}(f_{low}^{-1} - f_i^{-1}) \tag{3.3}$$

and for the front feed:

$$l_{hi} = \frac{1}{\tan(\alpha)}\left(\frac{\lambda_i}{4} - \frac{\lambda_{hi}}{4}\right) = \frac{c}{4\tan(\alpha)}(f_i^{-1} - f_{hi}^{-1}). \tag{3.4}$$

The two resistances can then be calculated:

$$R_{low} = R_s l_{low} = \sqrt{\frac{\mu}{2\sigma}}\frac{c}{4\tan(\alpha)}\sqrt{f_i}(f_{low}^{-1} - f_i^{-1}) = M_{back}(f_i)\sqrt{\frac{\mu}{2\sigma}}\frac{c}{4\tan(\alpha)} \tag{3.5}$$

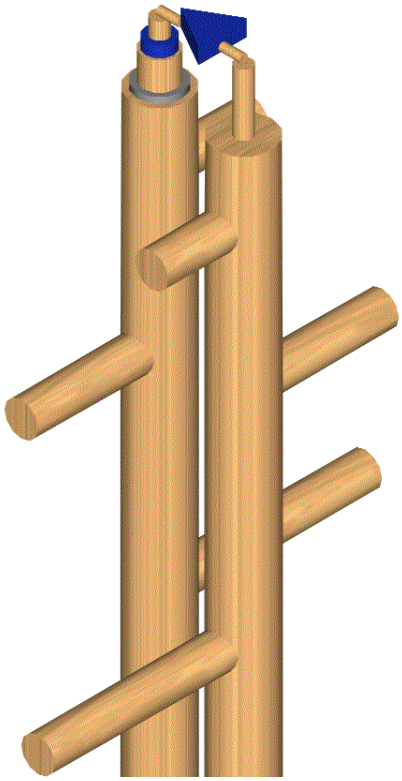

Figure 3.2. A sketch of the feed of an LPD array, the coaxial cable is routed through one of the center conductors of the antenna to prevent its interference with the radiation of the antenna. An integrated amplifier is also shown in the sketch. This is the proposed location of the LNA (at least the first stage LNA) to minimize the noise in the LPD array. The L_i's and R_i' are lengths, the D_i's are the wire diameters and the S_i's are the gap spaces.

where the multiplier $M_{back}(f_i)$ is:

$$M_{back}(f_i) = \left(\frac{\sqrt{f_i}}{f_{low}} - \frac{1}{\sqrt{f_i}}\right). \tag{3.6}$$

For front feed, the resistance is:

$$R_{hi} = R_s l_{hi} = \sqrt{\frac{\mu}{2\sigma}} \frac{c}{4\tan(\alpha)} \sqrt{f_i}(f_i^{-1} - f_{hi}^{-1}) = M_{front}(f_i)\sqrt{\frac{\mu}{2\sigma}} \frac{c}{4\tan(\alpha)} \tag{3.7}$$

where the multiplier M_{front} is:

$$M_{front}(f_i) = \left(\frac{1}{\sqrt{f_i}} - \frac{\sqrt{f_i}}{f}_{hi}\right) \tag{3.8}$$

The resistances of both feeds are the same except for the resistance multipliers, which are both functions of the frequency of the incident wave f_i. In Figure 3.3, the resistance multipliers are plotted for both the front and back fed antenna, the frequency range of the antenna is 2.0-4.0 GHz. The front feed has a resistance which is much lower at the high frequencies and the back feed has a lower resistance at the low frequencies. The maximum resistance multiplier of the front feed is 0.35 which is lower then the maximum of the back feed, 0.5. The average of the resistance multiplier from 2.0-4.0 GHz is 0.16 while the average of the back fed LPD is 0.28. Since noise power is proportional to resistance, the feed which has a lower average loss will also have a lower average noise power added to the signal. Any noise that is present in the system before the LNA will add more significantly to the noise than loss after the LNA, this is because:

$$T_{cas} = T_a + T_{A1} + \frac{T_{A2}}{G_{A1}} \tag{3.9}$$

where the T_{cas} is the total noise temperature of the antenna and LNAs, T_a is the noise temperature of the antenna, T_{A1} and T_{A2} are the temeratures of the LNAs. The noise after the first LNA will be reduced by the gain of the LNA, the noise before the LNA will be added to the total system noise. For this reason it is beneficial in a low-noise array, to integrate the LNA at the front of the LPD antenna.

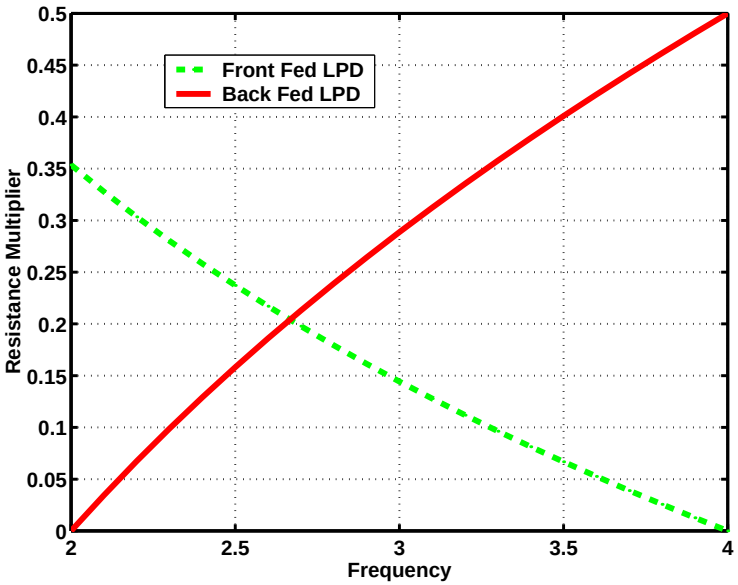

Figure 3.3. A plot of the resistance multipliers for an LPD array from 2.0-4.0 GHz. The resistance multipliers determine the value of the resistance are encountered by a signal before it arrives at the feed point of the antenna.

3.2.2 Physical Description of an LPD Array The LPD antenna has two electrical characteristics that are broadband, the impedance and the radiation pattern. The impedance of a LPD antenna is periodic when plotted vs. the logarithm of the frequency. The radiation pattern of the antenna is relatively uniform over the frequency range, with the gain increasing slightly with frequency.

The antenna is defined by four variables [18]: the length of the radiating elements l_n; the spacing of the elements R_n; the gap distance s_n; and the diameters of the radiating elements d_n, Figure 3.1. The LPD is defined by the geometric ratio τ

$$\tau = \frac{l_n}{l_{n+1}} \tag{3.10}$$

$$= \frac{R_n}{R_{n+1}} \tag{3.11}$$

$$= \frac{s_n}{s_{n+1}} \tag{3.12}$$

$$= \frac{d_n}{d_{n+1}} \tag{3.13}$$

the second parameter that defines the LPD array is the spacing factor σ:

$$\sigma = \frac{R_{n+1} - R_n}{2l_{n+1}} \tag{3.14}$$

The lines that connects the ends of the radiating arms form an angle 2α:

$$\tan(\alpha) = \frac{1-\tau}{4\sigma} \tag{3.15}$$

The values of τ and σ determine the gain of the antenna.

The length of the radiating arms of the LPD antenna determines the operating frequency of the antenna, with the lower frequency determined by:

$$f_{low} = \frac{c}{\lambda_{low}} = \frac{c}{2l_n} \tag{3.16}$$

and the upper frequency by:

$$f_{hi} = \frac{c}{\lambda_{hi}} = \frac{c}{2l_1} \tag{3.17}$$

where l_1 and l_n are as shown in Figure 3.1.

3.3 Simulation of the LPD antenna

The LPD antennas were simulated using several different Method of Moments simulation tools. The wire LPD antennas were simulated using *Matlab-WireZeus*. The commercial MoM package IE3D, from Zeland [9], was used to simulate a printed LPD antenna, Section.3.4. Because of the speed of *Matlab-WireZeus*, many simulations could be made. This allowed for the optimization of the antenna using several criteria for the goals of the optimization. The return loss of a LPD that was designed using this method is shown in Figure 3.4, and its 2:1 VSWR bandwidth is from 1.7-4.2 GHz.

The radiation patterns could also be easily calculated and used as one of the criteria in the optimization algorithm. Simulated three-dimensional patterns of the LPD antenna are shown in Figure 3.5 and Figure 3.6. Two dimensional slices of

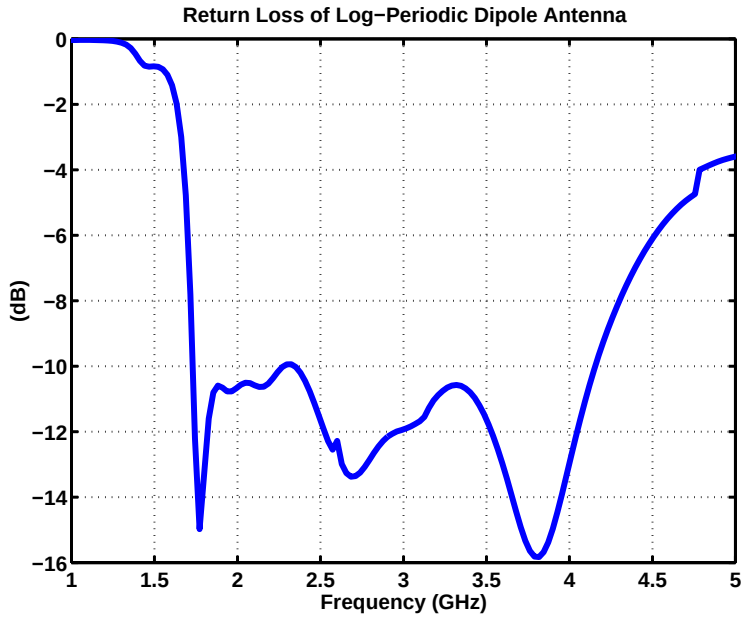

Figure 3.4. Simulated return loss of a LPD antenna with respect to 100Ωs. The LPDA was simulated using *WireZeus*, the simulation time was less the 0.5 seconds per frequency point at the highest frequency on a 400 MHz Pentium II.

the patterns are shown in Figure 3.7(a)-3.7(d). The beamwidths of the antenna are uniform over the operating frequency of the antenna. The 3-dB H-plane beamwidth of the LPD antenna is 50° at 2.0,3.0, and 4.0 GHz. The pattern at 5.0 GHz develops more side lobes because the frequency is out of the operating range of the antenna. The front-to-back ratio of the antenna was -18 dB for the antenna at 2.0 GHz and 3.0 GHz, it dropped to -10 dB and -9 dB at 4.0 GHz and 5.0 GHz.

Using the optimized LPD antennas, a fractal array was also simulated. In the fractal array there are two distinct frequency bands of operation 1-2 GHz and 2-4 GHz. There is also an overlap of 0.2 GHz from 1.9 GHz to 2.1 GHz. The array spacing of the LPD array is $0.5\lambda_o$ at the low frequency of operation of each antenna element. It has been demonstrated through numerical modeling that the LPD antenna could be a good candidate for a broadband antenna array. The one concern of the LPD antenna is the cost of fabrication, because it is a wire antenna, there is not an inexpensive way to fabricate it, like there is for many printed antennas.

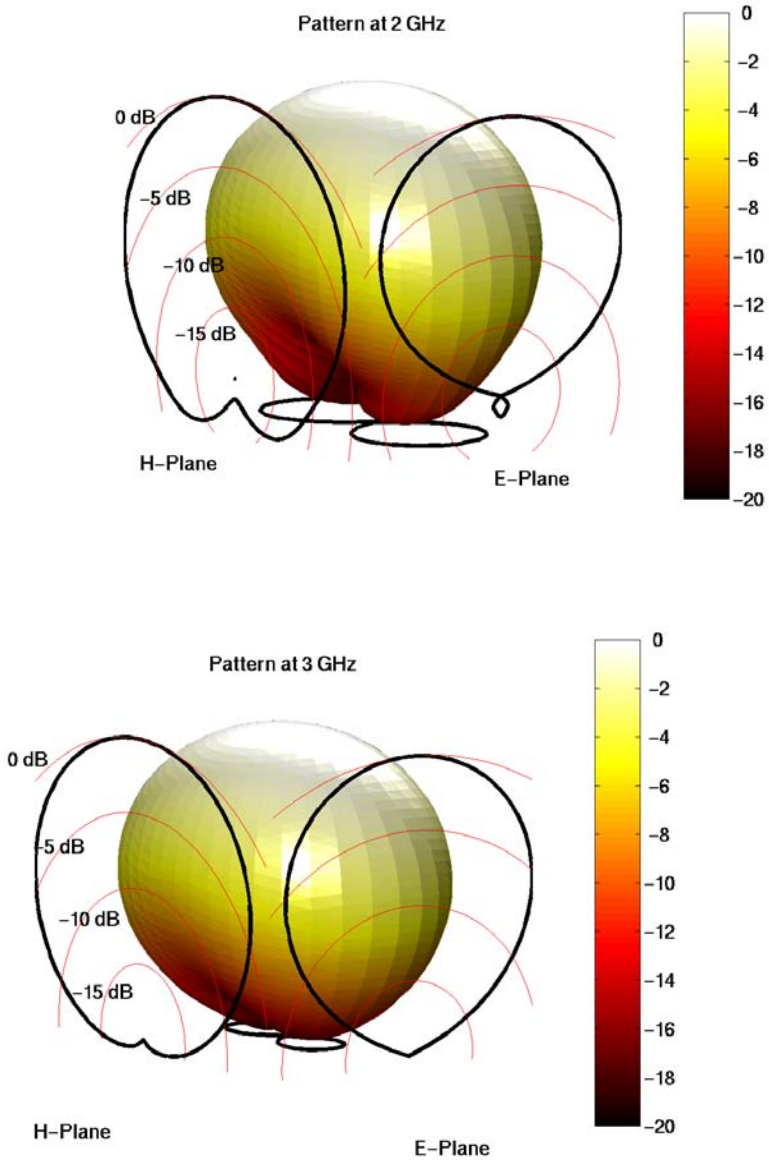

Figure 3.5. Simulated 3-D plot of the radiation pattern of a log-periodic dipole antenna. The 2-D plot in the z-y plane is the H-plane pattern, the E-plane pattern is drawn in the z-y plane. The pattern at 2.0 GHz is shown in (a), and at 3.0 GHz in (b)

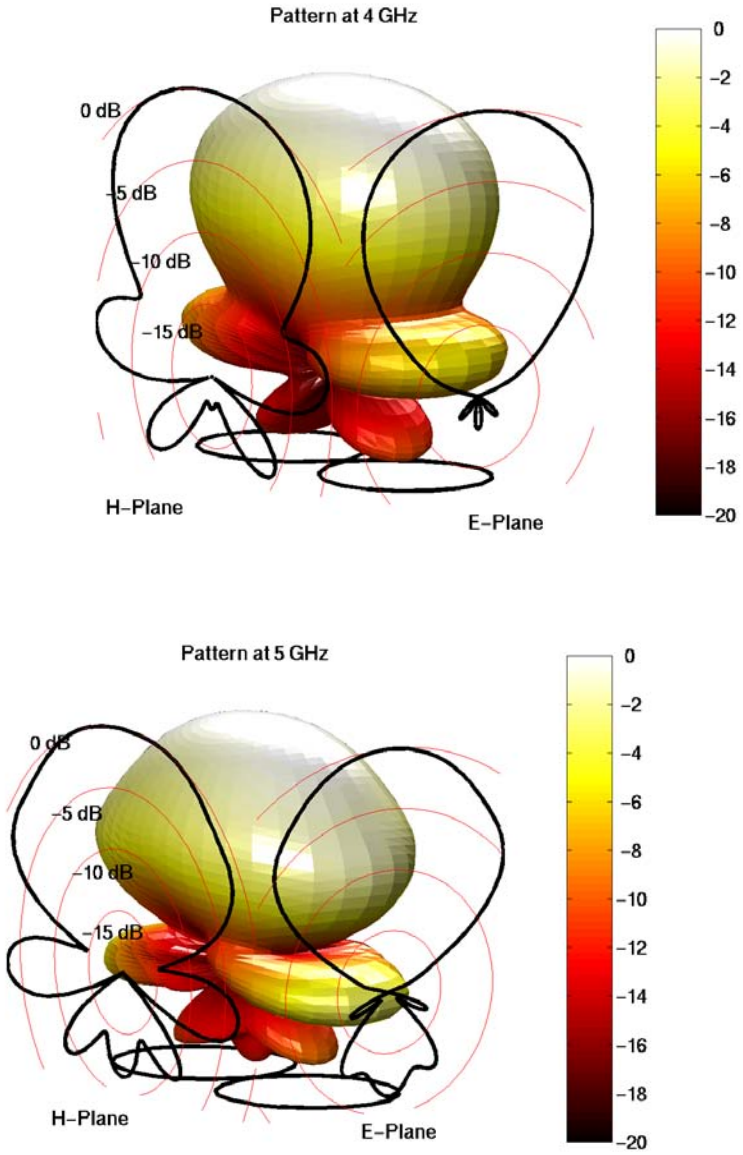

Figure 3.6. Simulated 3-D plot of the radiation pattern of a log-periodic dipole antenna. The 2-D plot in the z-y plane is the H-plane pattern, the E-plane pattern is drawn in the z-y plane. The pattern at 4.0 GHz is shown in (a), and at 5.0 GHz in (b)

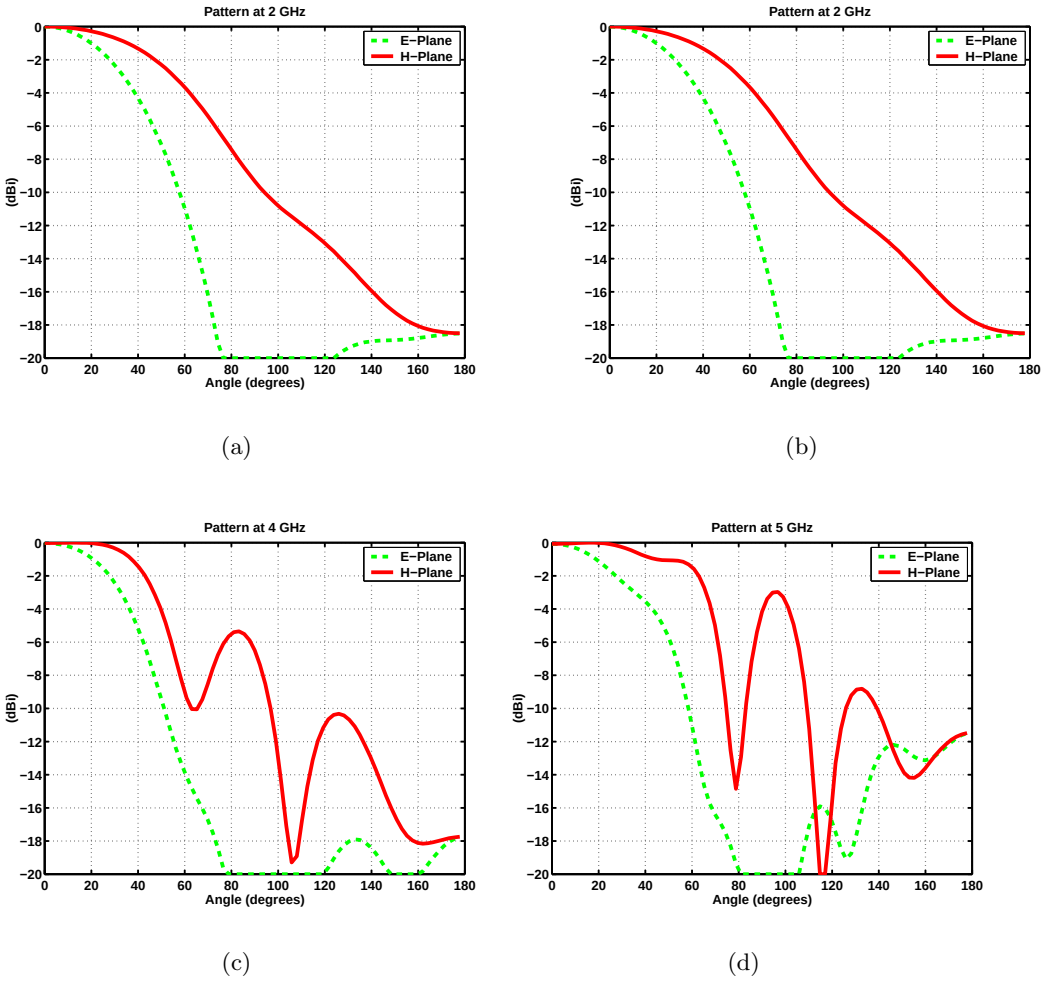

Figure 3.7. Simulated radiation patterns of a the LPD array, (a) 2.0 GHz,(b)3.0 GHz, (c) 4.0 GHz (d) 5.0 GHz. The beamwidth of the antennas is uniform of the first three frequencies, the 5.0 GHz pattern begins to deform because it is out of the operating range of the antenna.

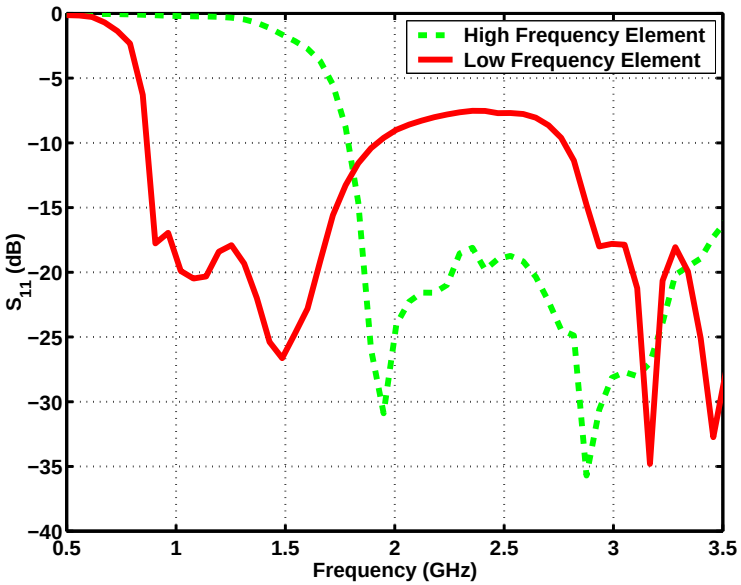

Figure 3.8. Simulated return loss of a fractal LPD array. Two distinct frequency bands correspond to the two different sized elements.

3.4 Printed Log Periodic Array

Since the LPD antenna is not a printed antenna, the cost to mass produce the antenna can be high, relative to a printed antenna. Printed antennas can be etched chemically **en masse**, while wire antennas need to be fabricated using mechanical methods. A printed log periodic dipole antenna with a novel feed is presented, Figure 3.11. The feed of the antenna is a strip-line feed that is routed through the center conductor of the antenna. The printed log periodic antenna is optimal for broad-band low noise applications because an LNA can be integrated into the antenna feed, with no extra biasing lines required. The presented antenna is a printed log periodic dipole antenna, with all the same characteristics of the standard LPD antenna, but with a lower cost of production, since it is printed it can be mass produced easily. Measured and simulated results of the antennas are presented, showing a radiation pattern that is constant over the frequency range of the antenna. The printed LPD antenna also has the benefit of easy integration of an LNA, as well as built in biasing.

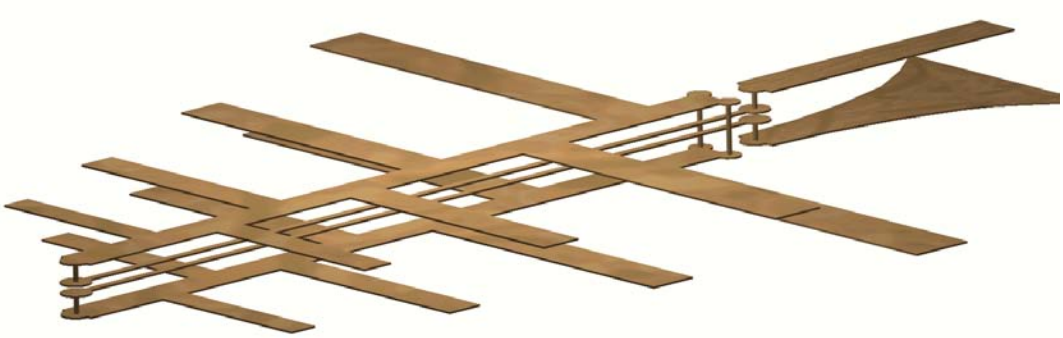

Figure 3.9: A drawing of the printed log periodic dipole antenna

3.5 Design of the Printed Log Periodic Dipole Antenna

The principle of the printed log periodic dipole antenna is the same as that of the standard LPD antenna. The design of the radiating portion of the printed LPD antenna follows the same guidelines as that of the standard LPD antenna. The shape of the radiating portion of the antenna is determined by four factors: τ, σ, l_1, and R_1, Figure 3.1 [16].

The value of l_1 is defined by the upper limit of the bandwidth $\lambda_{high}/2 = l_1$, Once l_1 has been defined, the values of l_i and R_i are derived using a simple recursive formula. The lower frequency of operation is the frequency whose wave length is double the length of the longest radiating element $l_n = \lambda_{high}$.

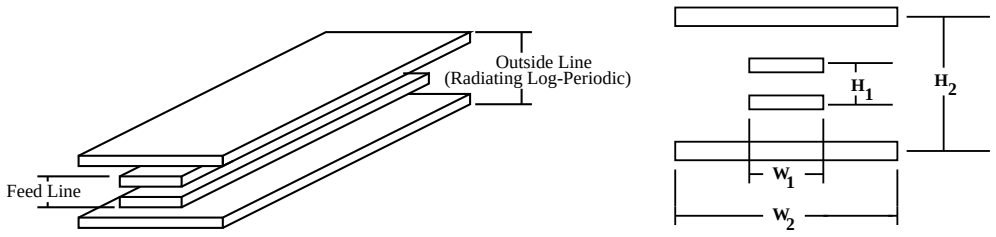

Figure 3.10. An isometric view (a) and a cross section view (b) of the shielded stripline transmission line. The two smaller center conductors form the stripline, the large outer conductors are part of the radiating portion of the printed log periodic antenna

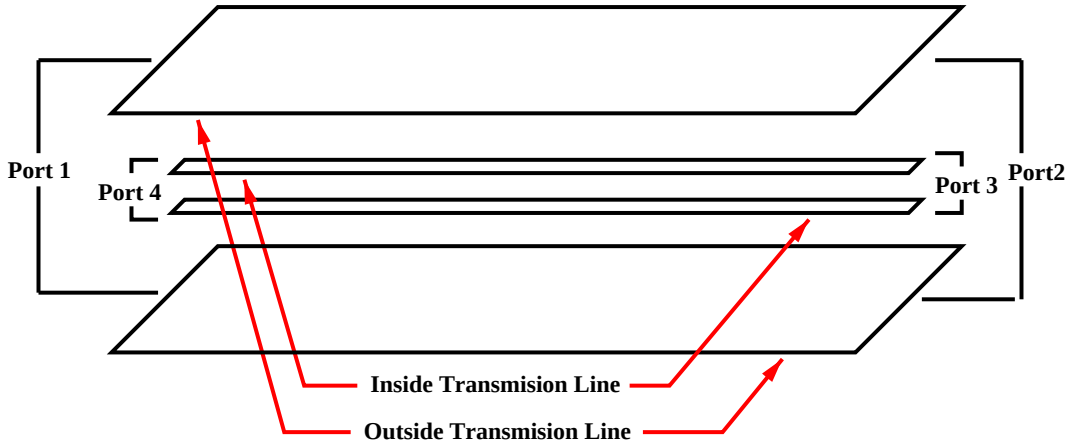

Figure 3.11. A drawing of the dual printed transmission line. There are a total of 4 ports, the outside line is connected to ports 1 and 2, the inside line is connected to ports 3 and 4. These were defined so that the isolation and transmision between the lines could be simulated.

In the standard LPD antenna the transmission line feed, a coaxial cable, is fed through one of the center tubes of the antenna. This is because the optimal feed point of a LPD antenna is at the radiating end of the antenna, the end with the smaller dipoles. Using a coax feed electrically isolates the feed from the rest of the antenna. By routing the coax through one of the center conductors it minimizes the interference with the radiation pattern. In the printed LPD antenna, the feed is brought to the front of the antenna as a microstrip line that is sandwiched between the two center arms of the antenna, Figure 3.11. The antenna was designed and optimized using two different software packages: GEM, an entire domain Method of Moments (MOM) code [19], and Zeland software's IE3D a commercial MOM code.

3.5.1 Shielded Microstrip Transmission Line In the printed log periodic dipole antenna, the feed line is a shielded microstrip line. The shielding of the line is the center conductor of the LPD antenna, Figure 3.10(b). The shielded stripline feed, can be optimized to minimize the coupling between the interior transmission line and outside conductors. The four variables in the optimization are the widths of the two lines, W_1 and W_2, and the separation of the two lines, h_1 and h_2,

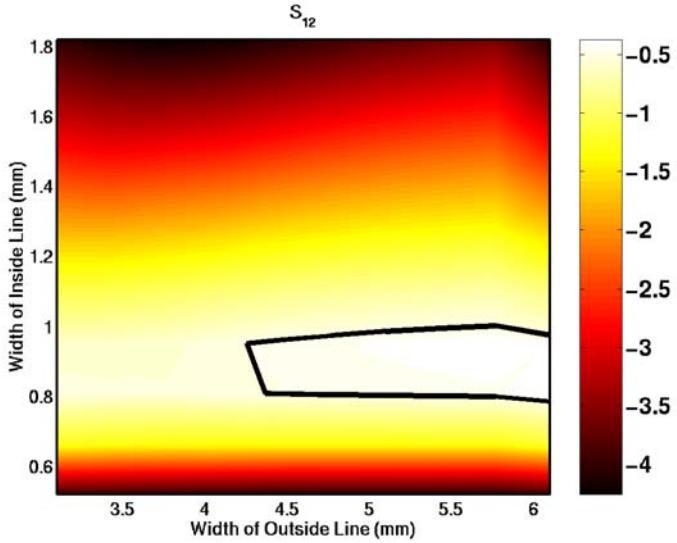

(a)

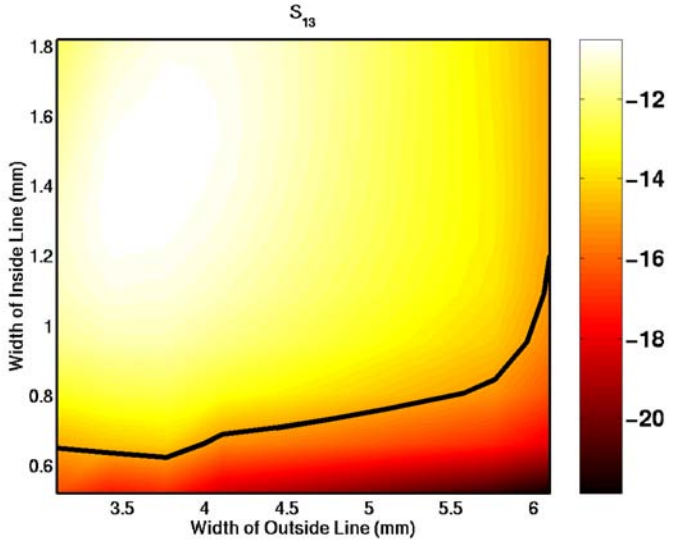

(b)

Figure 3.12. A parameters sweep of a four conductor printed transmission line. (a) S_{21} the transmission coefficient and (b) S_{31} the forward coupling. The lines were simulated using Zeland's IE3d. The separation of the outer two lines was 1.27 mm the separation of the inner-line was .25 mm. The vertical axis is the width of the inner conductor, the horizontal axis is the width of the outer conductor. The black line in (a) indicates the 0.5 dB and in (b) -17 dB

Figure 3.10(b). Since the heights are determined by the choice of substrates, only widths were used in the optimization. The lines are built using two different height substrates, 0.508 mm (20 mil) substrate for the outside two substrates, and 10 mil substrate for the substrate separating the inner conductors.

One concern in the design of the printed LPD antenna is the amount of coupling between the inner transmission line and the radiating portion of the antenna. Minimization of the coupling is important when an LNA is integrated into the antenna because high coupling between the transmission line and the radiating portion of the antenna will provide feedback to the LNA causing it to oscillate. A parameter sweep is done for the width of the inner and outer conductors, and coupling and transmission coefficients were computed, Figure 3.12. The optimal values, where the through was high and the coupling low, were chosen and are shown in Figure 3.13. The optimal values for the width were 0.8 mm for the inside transmission line, and 6.0 mm for the outside line.

A coupling of less than -17 dB was achieved both in simulations and measurements using a 0.8 mm inner conductor and a 6.0 mm outer conductor. The smaller the ratio of h_2/h_1, the less the coupling. As the distance between the inner conductors is decreased the fields will become confined to the smaller region around the inner conductors, and therefore the coupling will be smaller. As the size of the line is decreased, the ohmic losses of the line will increase thus there is a practical limit to the minimum coupling that can be achieved.

3.6 Measured and Simulated Results

The antenna was built on a $2.2\epsilon_o$ substrate with h_1=0.254 mm, h_2=1.27 mm. A rendered version of the antenna is shown in Figure 3.11 The simulated -10 dB bandwidth of the antenna is from 1.5 GHz, to 2.7 GHz, Figure 3.14. This was verified using both IE3D and GEM [19]. The measured results of the antenna match the trend of

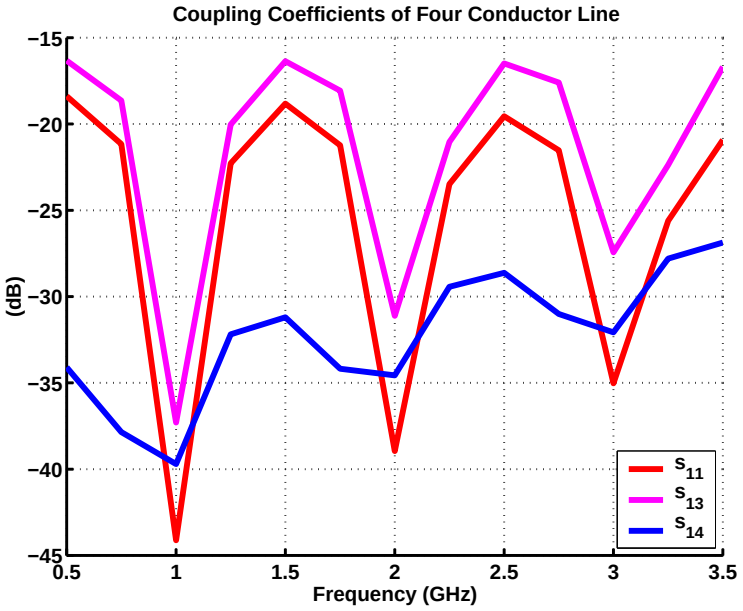

Figure 3.13. The simulated the coupling coefficients of a 10 cm four conductor transmission line. The coupling was lower the -17dB and the transmission is lower then -0.5 dB. Discrete points 250 MHz apart were simulated and the points are connected with lines for clarity.

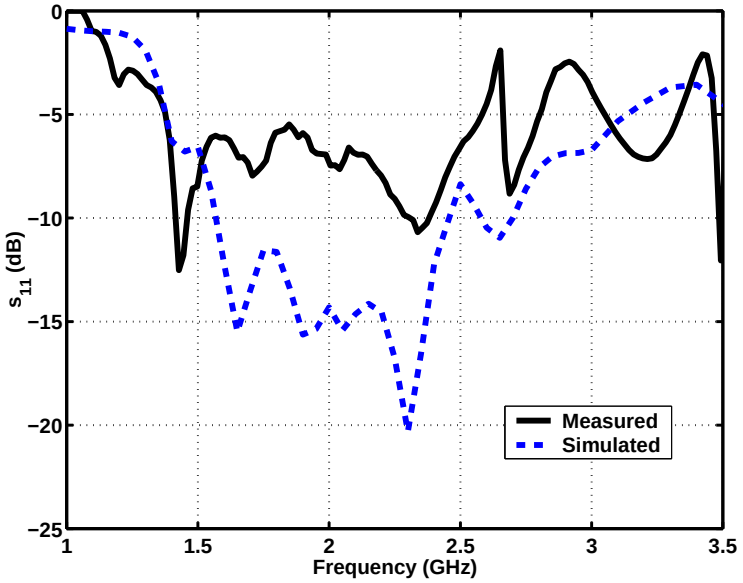

Figure 3.14. Measured vs. simulated return loss of the printed log periodic dipole antenna. The simulation was done using Zeland's IE3D.

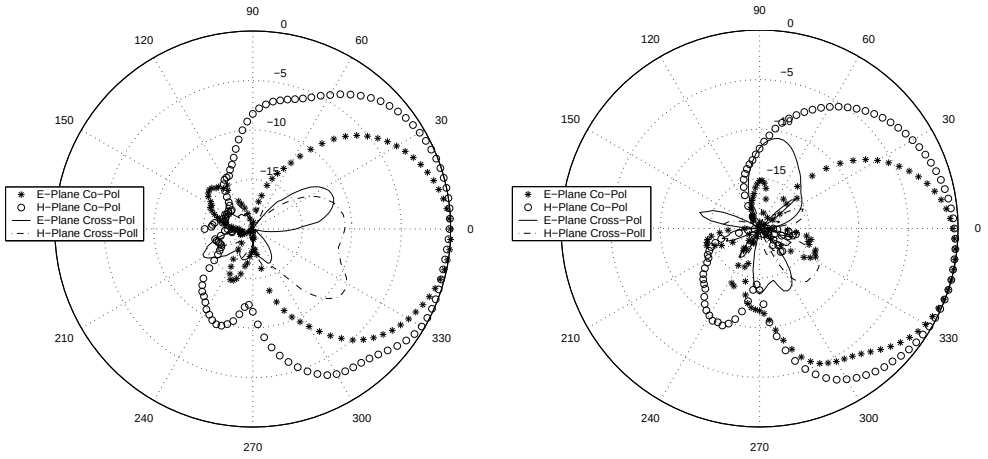

(a) (b)

Figure 3.15. Co-polar and Cross-polar E-plane and H-plane Radiation patterns, of the printed log periodic dipole antenna, at 2.0 GHz(a) and 2.5 GHz (b)

the simulated results well, with a sharp drop in the reflection coefficient at 1.5 GHz, and another at 2.6 GHz. The measurement agrees well with the simulated frequency behavior, but differs with the simulated value for the return loss. A difference of 4 dB in the reflection coefficient means that the simulated antenna will radiate 15% with an identical incident wave. The difference between the simulated and fabricated antenna may be due to an overly simplified model used in the simmulation. In the simulation we assumed a perfectly uniform substrate that contained no air gaps between two laminated substrates or warping of the substrates. The fabricated antenna contained small airgaps between the laminated substrates, because we did not have the ability to properly laminate substrates. An other source for error could be in the alignement of the substrates, the simulation assued a prefect alignement, in the fabricated antenna, the alignement was off by about $+/-0.2/$,mm.

The radiation patterns of the antennas were measured at two different frequency points 2.0 GHz and 2.5 GHz. The radiation patterns of the antenna are shown in Figure 3.15(a) and Figure 3.15(b).

The -3 dB E-plane beam width is 90° degrees for both frequencies. The H-plane beam width is 120° for both measurements. It is common for dipole type antennas to have a broader beam width in the H-plane than the E-plane because as the antenna is scanned in the E-plane the effective length of line on which the current is significent gets shorter. The polarization isolation of the antennas is lower then -15 dB over all angles for both antennas. The antenna had a slightly better polarization isolation at 2.0 GHz than at 2.5 GHz. The front to back ratio of the antenna is less then -15 dB which is within the standard for a log periodic dipole antenna.

3.7 Conclusion

The LPD antenna was shown to be a good candidate for SKA. The radiation pattern of the antenna is broadbeam over the operating frequency of the antenna. The front-to-back ratio of the antenna also makes it an ideal antenna to be used for a large phased array since no ground plane is necessary, thereby lowering the cost of the array. It was also shown that by integrating an LNA into a feed point at the front of the LPDA, the noise figure of the antenna is minimized. The simulated results of a wire-LPDA showed a broad bandwidth antenna with uniform radiation patterns.

A new design for the LPDA was proposed, a printed version of the LPDA. Because the antenna was printed, it is felt that the cost of production would be lower than for a wire LPDA. The printed log periodic dipole antenna, shows a good radiation pattern, over its frequency range, as well as a large (simulated) bandwidth. We feel that this antenna would be an ideal candidate for the Square Kilometer Array antenna, because of its broad bandwidth, wide beam width, low cost of fabrication as well as the ease of integration of an LNA.

CHAPTER 4

TAPERED SLOT VIVALDI ANTENNAS

4.1 Introduction

Vivaldi antennas are a type of tapered slot antenna, they are aperiodic and continuously scalable. The Vivaldi antenna is a traveling wave antenna, where the radiating mechanism of the antenna is produced by a wave traveling down the slotline. The antenna is fed by a slotline transmission line, which consists of two co-planar conductors separated by a narrow gap. In a Vivaldi antenna, the gap between the conductors increases exponentially as a function of the distance from the feed, Figure 4.1. A wave propagating along the slotline is tightly bound to the conductors. As the gap increases, the fields become less bound to the conductors, and the energy couples to the radiating field of the antenna [20].

Unlike the log-periodic dipole antenna, which consisted of a finite number of frequency bands, continuously scaled antennas have a smooth continuous transition between frequency bands. The bandwidth of a Vivaldi antenna of infinite extent is theoretically infinite; the physical size of an actual antenna determines the low frequency of operation $f_{low} = c/2h$. The method we used for feeding the slot line was a microstrip to slotline transition. In practice, we have found that the bandwidth of the transition determines the bandwidth of the antenna, at the high frequency limit.

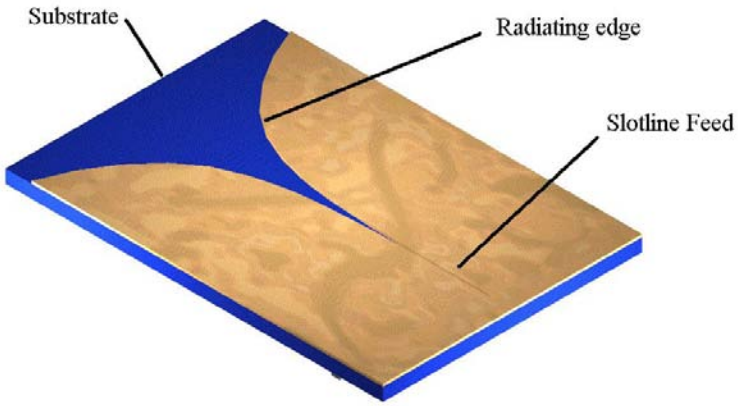

Figure 4.1. A sketch of a Vivaldi antenna, the slotline transmission line tapers exponentially. The transition to the slotline is not shown.

4.2 Slotline transmission line

The slotline transmission line consists of a narrow slot or gap in a thin conductor on one side of a dielectric substrate, with no metalization on the other side, Figure 4.2. In simulations of the slotline, the semi-ground-planes on either side of the slot are assumed to be infinite where as in practice a size of half a wavelength is usually sufficient.

For most applications of the slotline, the dielectric constant of the substrate is generally quite high ($\epsilon_r > 9$). This is because a low impedance ($Z_o < 50\Omega$) slotline requires a large dielectric constant and a small gap. The high dielectric substrate will confine the fields to the slot region and cause the slot-wavelength (λ_{slot}) to be

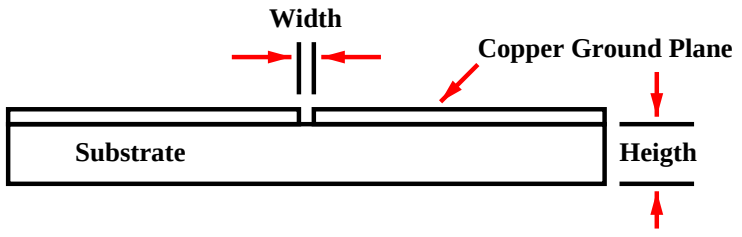

Figure 4.2. A sketch of the slotline transmission line. The circuit has a metalization on one side, with a small slotline gap transmission line.

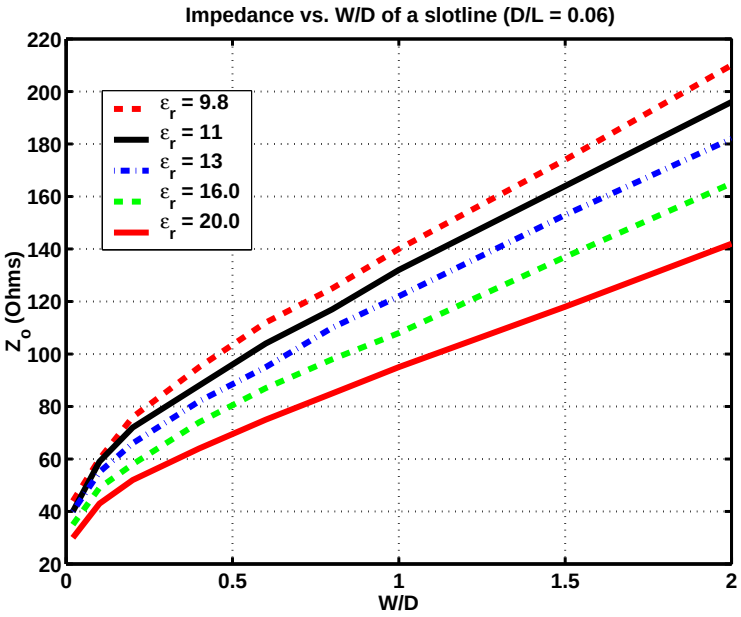

Figure 4.3. A plot of impedance as a function of W/D (slot width / substrate height), since the slotline is a quasi-TEM line the impedance is not constant with respect to W/D but also varies slightly with the substrate height (D) of the slot as a function of λ. A value of $D/\lambda = 0.06$ was chosen for this plot.

much smaller then the free space wavelength (λ_o), lowering the radiation loss of the slotline. The slotline is a non-TEM transmission line, so its characteristics Z_o and v_{ph} will vary (slowly) with frequency. The impedance as a function of slotline width to substrate height (W/D) is plotted for several different substrates in Figure 4.3, the data was taken from [21].

4.3 Microstrip-to-Slotline Transitions

The first phase in the design of this tapered slot antenna was the study of different ways of feeding the antenna. Two different methods were considered: a coaxial-line to slotline transition; and a microstrip-to-slotline transition. The design chosen was a microstrip coupled to a slotline. This design was chosen because it is simple to fabricate. It does not require any soldering or vias, while the coax-to-slotline has a solder connection which in a large scale production that would be

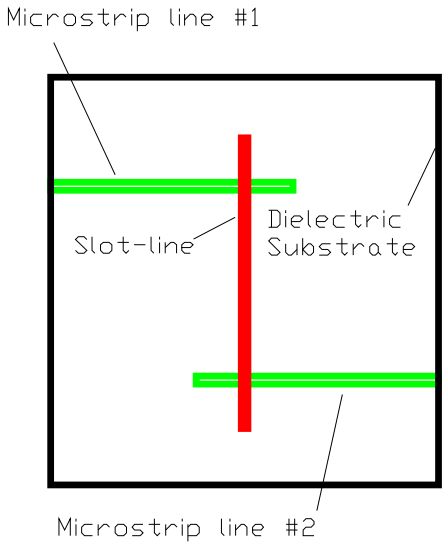

Figure 4.4. Sketch of a microstrip-to-slotline coupler. This was one of the types of couplers that was used to test the bandwidth of the microstrip-to-slotline transition.

required for SKA would be cost prohibitive. In order to test the feed, we designed and built three different transitions, consisting of a microstrip coupled to a slotline then back to a microstrip. This was done so that the reflection and transmission coefficients of the coupler could be measured.

The couplers consist of a ground plane backed substrate. Etched on one side of the substrate are two 50 Ω microstrip lines. On the back side of the substrate is a ground plane with a slotline milled into it. The coupler design is shown in Figure 4.4. The lines extend a quarter wave beyond their point of intersection. The microstrip is terminated in an open circuit, and the slotline is terminated in a short, the combination of two lines looks like a through at the center frequency. The bandwidth of this type of transition is generally about 30% [21]. The transmission coefficient of the coupler is shown in Figure 4.6.

Three different couplers were built, to try and increase the bandwidth of

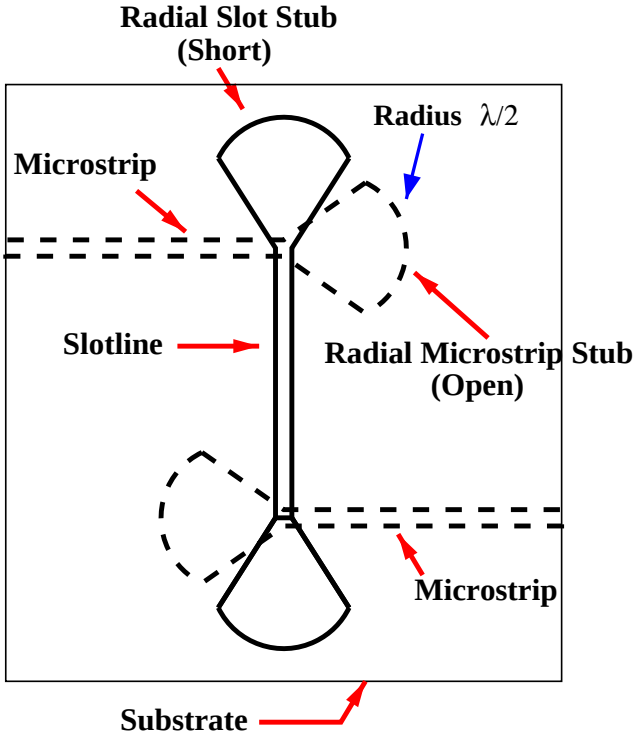

Figure 4.5. Sketch of a radial microstrip-to-slotline transition. The solid lines represent a slot on the front side of the substrate, and the dashed lines represent a microstrip line on the back side of the substrate. The radii of the radial stubs are one half of the guided wavelengths.

the microstrip-to-slotline transition. Each of these has a different type of transition. These were designed to improve the bandwidth of the transition by using a broadband transition. The use of a radial stub transition was suggested by [22]. This design uses a radial stub with an internal angle of 90° and radius of $\lambda_{slot}/2$ for the slotline stub, and $\lambda_{ms}/2$ for the microstrip line stub, Figure 4.5. Two radial stub transitions were fabricated and tested: a 5 GHz coupler, where the radius of the stub is $\lambda/2$ at 5.0ĠHz; and a 2.5 GHz coupler. An experimental transition was also built. This transition used a varying radius tapered stub. The graphs for the four different transitions are shown in Figure 4.6, the bandwidths are also shown in Table 4.3.

The standard microstrip-to-slotline transition has a bandwidth of only 75% (2.2:1). The bandwidth of the radial-stub transition is the largest, with a bandwidth

Transition	F_{low}	F_{hi}	Bandwidth	Percentage BW
Normal Stub	2.63 GHz	5.81 GHz	2.2:1	75%
Radial Stub (2.5 GHz)	0.63 GHz	4.13	6.5:1	147%
Radial Stub (5.0 GHz)	0.95 GHz	7.0 GHz	7.4:1	152%
Exponential Stub	0.88 GHz	4.34 GHz	4.9:1	132%

Table 4.1. Bandwidths of the four different microstrip-to-slotline transitions. The definition of the bandwidth was 0.6 dB of loss per transition. The plots are shown in Figure 4.6.

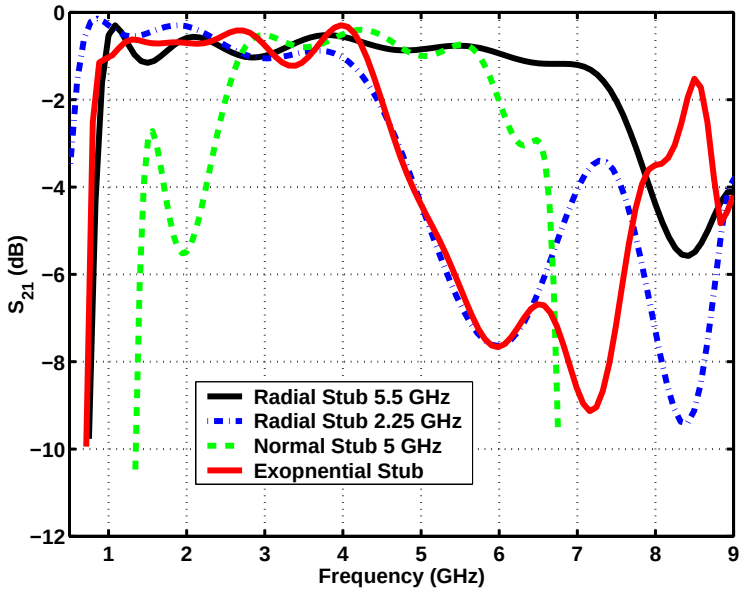

Figure 4.6. Measured transmission coefficients of microstrip to slotline transitions. Four different transitions were measured. The bandwidth of the transitions ranged from 152% for the 5.0 GHz radial stub to 75% for the normal transition. The bandwidth are shown in Table 4.3.

of 147% (6.5:1) for the 2.5 GHz transition, and 152% (7.4:1) for the 5.0 GHz transition. The bandwidth of the exponentially tapered stub is 132% (4.9:1), which was smaller than both of the radial stubs. Because of the large bandwidth of the radial stubs, these are the transitions that were used for the Vivaldi antennas.

4.4 Vivaldi Antennas

Once the design of the transitions was understood, we preceded to use the transitions in the design of several slot fed Vivaldi antennas. The first antenna that was built used the straight quarter wave microstrip-to-slotline transition. This antenna is built on RT/Duroid®6010, a substrate with $\epsilon_r = 10.2$, a substrate height of 0.508 mm (20 mil). The antenna was built on a $\epsilon_r = 10.2$ substrate. The design was a microstrip coupled to a slotline that flared in to an exponential taper, the taper chosen was one that was give by [20]. The values were changed to scale the new frequency range 3-5 GHz. The form of the exponential taper is given by:

$$y = 1.0189(e^{62x} - 1) \tag{4.1}$$

where x is the distance from the feed (in meters), and $2y$ is the width of the slot (in meters). The antenna was simulated using *GEM*. The insertion loss of the antenna was lower than -10 dB from 2.0 to 3.7 GHz, Figure 4.8. There is an excellent agreement between the measured return loss and the simulated return loss. The radiation patterns of the antenna are shown in Figure 4.9. The E-plane pattern of the antenna has a beam-width of 60°, the H-plane has a beam-width of 120°. Both the E-plane and the H-plane have large back lobes that are -4dB down form the main beam in the H-plane, and -6dB down from the main beam in the E-plane. These are due to the feed of the antenna radiating. These lobes could be suppressed using a shielding over the microstrip to slotline transition. There are also a lot of ripples in the antenna pattern. These ripples are variations in the power of the antenna of

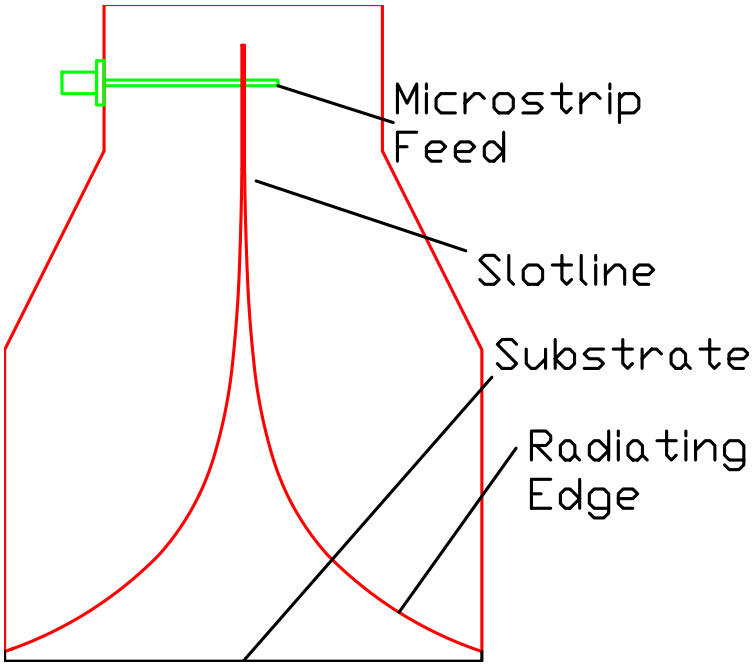

Figure 4.7. Vivaldi antenna with microstrip feed. This antenna was built on Duroid®with $\epsilon_r = 10.2$.

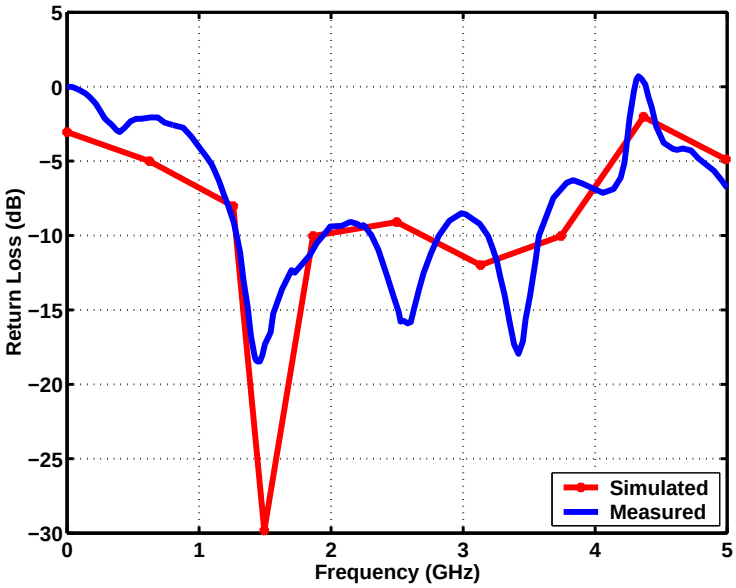

Figure 4.8. Measured return loss of Vivaldi Antenna, the blue line denotes the measured data the red is the simulated data. The 2:1 VSWR bandwidth of the antenna is from 2.0-3.7 GHz

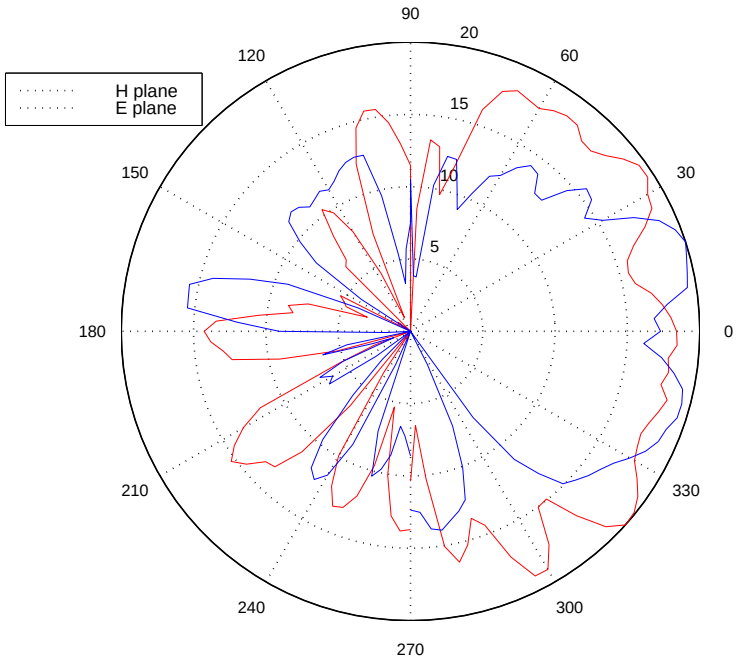

Figure 4.9. E and H patterns of Vivaldi Antenna on a substrate with a permittivity of 10.2. E-plane is shown in blue, and the H-plane in red. There are some large back lobes due to a radiating antenna feed. Also the pattern has some ripples in it, these are due to substrate modes, and will be "smoothed" in a phased array.

about 3 dB. In a phased array environment the ripples in the pattern of an individual element would be averaged with those of its neighboring elements, this would lead to an overall smoothing of the antenna pattern.

The ripples in the pattern are due to substrate modes, which arise on account of the high dielectric constant of the material. We fabricated an antenna using the same microstrip-to-slotline transition, but used a polystyrene substrate for the radiation portion of the antenna. This was completed to see if the ripples could be removed using a lower dielectric substrate, while still using the high dielectric substrate for the transition. The pattern was much better, as seen in Figure 4.10, and there are no ripples in the pattern. This antenna had a half power beam width of 60° in the H plane and 30° in the E plane. These beam widths are different in the two antennas because the current distribution changes when the substrate

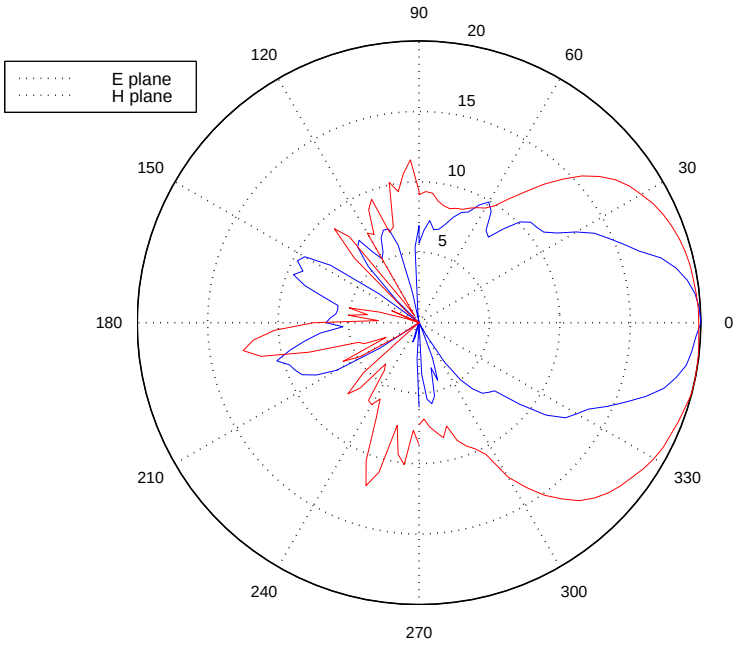

Figure 4.10. Measured E and H plane patterns of Vivaldi antenna with the radiating portion built on polystyrene. Polystyrene was used to minimize the ripples in the pattern of the antenna with a high permativity substrate.

is removed. The side lobes were also smaller for the polystyrene backed antenna, less than -10 dB, compared to -5 dB for the $10.2\epsilon_r$ antenna. There is one relatively large back-lobe -7 dB down from the main beam, which is still better then the -4 dB back-lobes for the substrate antenna.

4.5 Improved Vivaldi with broadband feed

The next antenna design used the radial stub transition, in hopes of improving the bandwidth of the antenna. The 5.0 GHz radial stub, Section 4.2 was used in the new antenna design. The improved antenna were built on a 50 mil, $\varepsilon_r = 10.2$ substrate for the feed, air for the radiating part of the antenna. Copper radiating elements are soldered to the ground-plane on both sides of the slot, being the radiating portions of the antenna. The -10 dB bandwidth of the antenna is from 3.0 GHz to 7.8 GHz an 89% bandwidth (2.5:1), Figure 4.11. The return loss of the

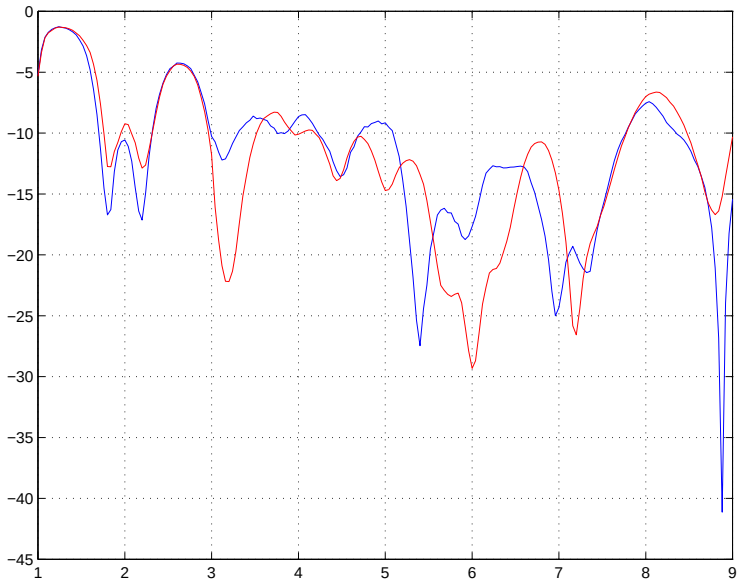

Figure 4.11. Measured return loss of two Vivaldi antennas with a broadband radial stub feed. Two antennas were built to measure the coupling between them. Also to test how sensitive the design was to fabrication errors

antenna is below -10 dB from 1.8-2.3 GHz, and again from 4.0 -7.8 GHz, but has a larger return loss from 2.3-3.0 GHz. The larger return loss for this small region of the bandwidth was present in all of the earlier designs. It was not until we performed multiple simulations, and frequency sweeps of all the Vivaldi antenna parameters that we fully understood where this came from, see Section 5.4.

The radiation pattern of the antenna was measured for 3,4,5,6,7,and 8 GHz, in both the E-planes and H-planes. The beam width of the antenna varies from 40° at 3 GHz to 25° at 6 GHz for the E-plane, Figure 4.12 and 60° at 3 GHz to 50° 6 GHz for the H-plane, Figure 4.13. The patterns of the E-plane are to narrow for the horizon to horizon scanning that needs to be performed with SKA. The beam-width of a Vivaldi can be controlled by changing the shape of the exponential taper, so the design of the taper will have to be changed to increase the beam-width.

4.5.1 Coupling In a phased antenna array, the coupling between the elements is of critical importance. It can affect the scan-performance, (Section 6.2)

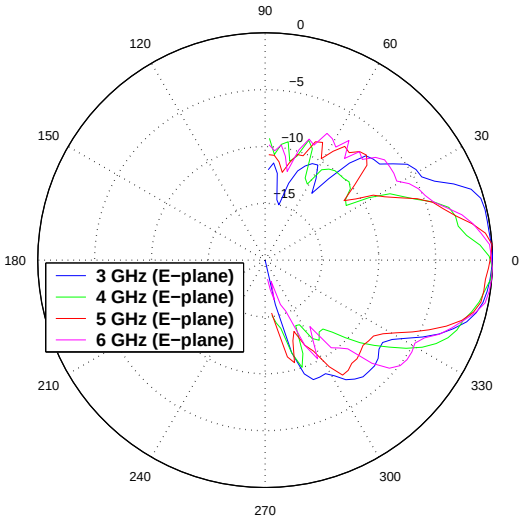

Figure 4.12. Measured E-plane patterns of the Vivaldi antenna with no substrate for the radiating portion of the antenna. The frequencies that were measured are 3,4,5 and 6 GHz.

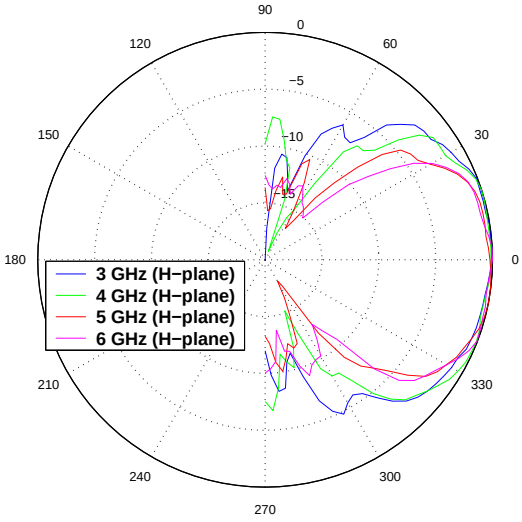

Figure 4.13. Measured H-plane patterns of new Vivaldi antenna with an no substrate for the radiating portion of the antenna. The H-plane beamwidth are wider then those of the E-plane.

as well as the noise performance, of the array (to be discussed in Section 6.5). The antenna's coupling was measured both co-polarized and cross-polarized. The was done using two identical antennas, antenna (A) and (B). These were the higher frequency Vivaldi antennas discussed in Section 4.5. Antenna A was connected to a sweeper at 4.0 GHz and 0 dBm output power, antenna B was connected to a power meter. The antennas were then moved with respect to each other and the power received was recorded for each position, Figure 4.14. The numbers along the Y and X axis are in millimeters, the Z-axis is power in dBm. In the Figure 4.15, the red surface corresponds to the co-polarized measurements, and the blue to the cross-polarized measurements. The coupling factor (S_{12}) is -20 dB at its highest value; this corresponds to when the antennas are almost touching. The cross-pol coupling is larger then the co-pol coupling when the fin of one antenna is lined up with the slot of the other. These measurements have not been calibrated, and the loss of the coax line has not been taken into account. This could raise the coupling figure slightly by about 3 dB.

We feel that these measurements show another benefit of the Vivaldi antenna, namely that the low coupling allows for smaller spacing of the antennas, which leads to a more efficient use of space, as well as a more optimal array spacing.

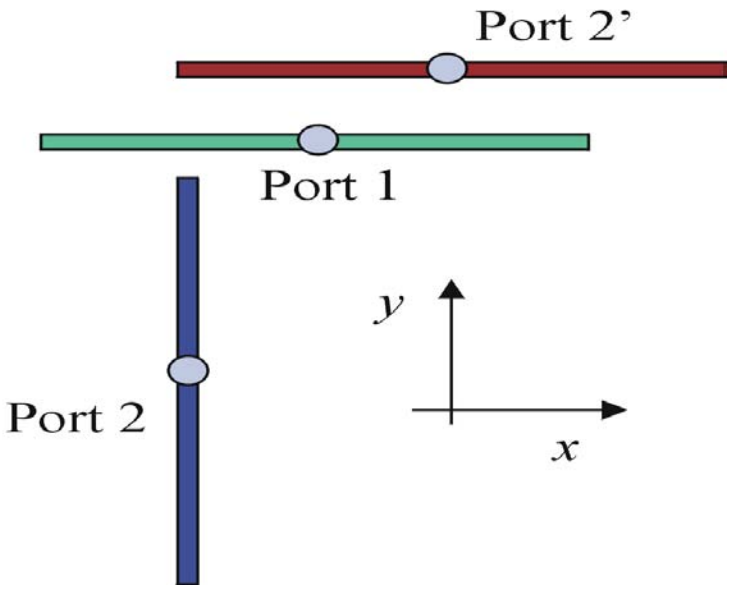

Figure 4.14. The layout of the Vivaldi antennas, that was used to measure the coupling between the two antennas. Antenna 1 was fixed, and antenna 2 and 2' were moved. The coupling was then measured and plotted as a function of the distance.

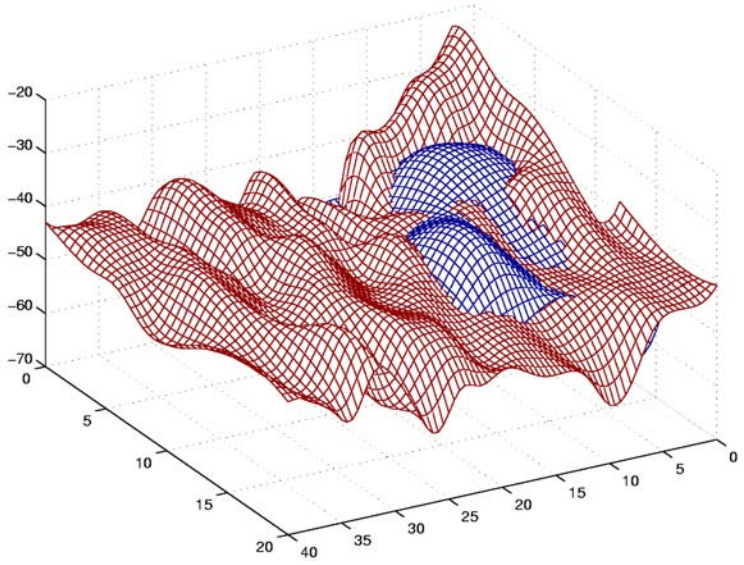

Figure 4.15. Coupling coefficient between two Vivaldi antennas, the X-axis and Y-axis are distances in cm, the Z-axis is S_{21} in dB. The red surface is the co-polar coupling, when the antennas were co-polarized. The blue surface is the cross-polar coupling. The maximum coupling between the antennas was -20 dB.

CHAPTER 5

ANTIPODAL SLOT FED VIVALDI ANTENNA

5.1 Introduction

In theory, the bandwidth of an ideal Vivaldi antenna is infinite, and the only limitation of the bandwidth is the finite physical size of the antenna. In practice, the bandwidth of a Vivaldi antenna is limited by the microstrip-to-slotline transition. In the slotline fed Vivaldi this limitation was solved by using a broadband transition. Another problem with the slotline fed Vivaldi is the high dielectric constant that is required for low impedance slotline. High dielectric substrate is expensive ($900cm^2$ of Duroid RT®RT1040 costs 300$). Also an antenna built using a high dielectric substrate can have ripples in the radiation patterns, Section 4.4, caused by substrate modes. One solution that was proposed by [23] is to use an antipodal-slotline transmission line as the feed. Unlike the asymmetric slotline that has metalization on only one side of the substrate, an antipodal-slot line is a balanced line with metalization on both sides of the substrate.

5.2 Antipodal Antenna

The antipodal-slot transmission line consists of a substrate with metalization on both sides, Figure 5.1. Studies and experiments of the antipodal slotline have been made in [24] [25] [26] [27]. There are two semi-infinite ground planes on either side of the substrate. The line-parameters are defined by the height of the substrate and the gap between the slots. In the antipodal-slotline the gap can have

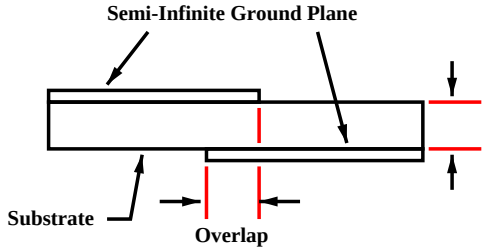

Figure 5.1. A symmetric double sided slot line (antipodal-slotline) can be easily designed to have a low impedance even on a low dielectric constant substrate. By varying the overlap, the impedance can be changed. The bigger the overlap, the lower the impedance of the line. (The overlap can be negative for a very high-impedance line)

a *negative* distance which corresponds to an overlap of the two semi-infinite ground planes.

A benefit of the antipodal-slotline is that it does not require the high dielectric substrate that is needed for the slotline fed Vivaldi. In a one-sided-slotline, the substrates dielectric constant must generally be large ($\epsilon \geq 9$) for a transmission line with low impedance ($Z_o \approx 50\Omega$). In the antipodal-slotline this can be done with a substrate which has a lower dielectric constant.

An antipodal-slot transmission line thus has a wider range of operating impedances. Because there can be an overlap of the ground planes as well as a gap between them. By increasing the overlap between the conductors in the antipodal-slotline, the capacitance between them is also increased, and the impedance of the line is lowered, because the impedance of a transmission line is:

$$Z_{Qslot} = \sqrt{\frac{L_{Qslot}}{C_{Qslot}}}. \tag{5.1}$$

Antipolal-slotline fed Vivaldi antennas, also called an antipodal Vivaldi antennas, have been built with bandwidths up to 18:1 [23]. Because the two radiating elements of the antenna are in different planes, the antipodal antennas have poor cross-pol performance at higher frequencies [28]. The radiating portion of the Vivaldi antenna, for a frequency f_o, is at the point on the radiating arms where the distance

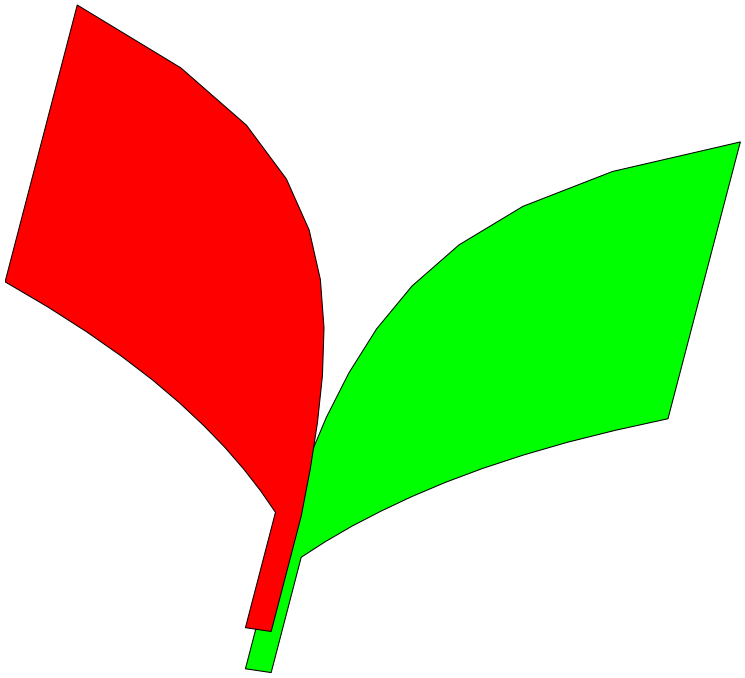

Figure 5.2. A sketch of an antipodal Vivaldi antenna. The antipodal antenna has two radiating arms on a separate side of the substrate, this makes it easier to feed the antenna since it does not require a microstrip-to-slotline transition.

between the two conductors is $\lambda_o/2$. As the frequency of operation of the antenna increases, the radiating portion of the antenna moves closer to the feed. Because the radiating arms are on different sides of the substrate, the E-field skews as the frequency increases (Figure 5.3). The angle of the skew is determined by the height of the substrate, the frequency, and the guide wavelength λ_g. The angle of the skew at a frequency f_o is $\sin^{-1}(2h_{sub}/\lambda_g)$. The skew is smaller at lower frequencies since the ratio of the thickness of the dielectric substrate to the width of the radiating part of the antenna is smaller than at higher frequencies. This leads to a shift in the cross-polar isolation over the frequency of the antenna. For SKA, the upper range of the operating frequency of the antenna is 2.0 GHz if a 50 mil substrate is used. In that case, the maximum skew would be less then 1°.

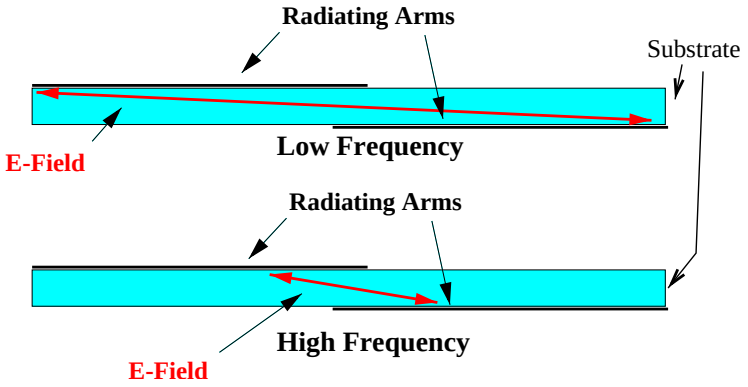

Figure 5.3. A sketch of the shift in the polarization of the antipodal Vivaldi antenna. Looking down the antenna, the two radiating ears of the antenna are represented by the two horizontal lines. A low frequency wave will be received by parts of the antenna that are farther apart, resulting in a lower shift in polarization then the for the higher frequencies, bottom figure.

5.3 Design and Fabrication of the Antipodal Vivaldi Antenna

Four different antipodal antennas were designed and built. Two of the designs were built on low-cost substrates, the first on ComClad (an automotive plastic); and the second on polycarbonate (a type of Plexiglas used for fabrication in the lab). We felt that it was important to test low-cost materials for the SKA project, because the cost of the antennas is an important design criterion when the area of the array is as large as 1km^2. The second two antennas were built using Rogers RT/Duriod®5880, a substrate with a dielectric constant of $\epsilon_r = 2.2$. This substrate was used because it was easier to work with than the low-cost substrates. The antipodal antennas were designed and simulated using two different MoM (Method of Moment) codes, *GEM* and *IE3D's Zeland*.

5.3.1 Four Element Linear Array

A four element, linear antipodal array was built using the ComClad substrate. ComClad is a high frequency circuit material that employs a commercial plastic as the base dielectric [29]. This plastic was first used in dashboards of automobiles, and later found to have good electrical properties at microwave frequencies. The ComClad substrate is 1.57 mm thick, with

a permittivity of $\epsilon_r = 3.6$ and a $\tan\delta = 0.0025$. Mechanically the substrate can be formed, molded, bent, and even over insert-molded via conventional plastic injection processes, making it an ideal candidate for a mass-produced antenna array like SKA. The main drawback of the substrate is its low melting temperature, making it difficult to solder.

The antennas is fed using an SMA-microstrip connector. An exponential balun is used for the microstrip-to-printed-twinline transition. The transition uses an exponential taper for the ground plane, which transitions in to the bottom of the printed-twinline (Figure 5.5). The exponential balun is used to transition from the balanced printed-twinline to the unbalanced microstrip line. This transition was proposed by [30]. The printed twinline then transitions into the antipodal-slotline which becomes the radiating portion of the antenna.

To test the microstrip-to-printed-twinline transition two different transmission line circuit were etched onto the ComClad substrate. The first circuit was a microstrip-to-exponential-balun-printed-stripline transition. The second circuit was a microstrip-to-printed-stripline transition. This line did not use a balun, but instead used an instantaneous change between the two transmission lines. The transition that used the balun had a -0.25 dB loss per transition and the abrupt transition had a loss as high as -1.0 dB per transition. The loss of the substrate was 0.03 dB/cm at 2.0 GHz and 0.13 dB/cm at 6.0 GHz. The ComClad antenna was optimized for bandwidth, using *GEM*. The design of the antenna is shown in Figure 5.6. Each element is 6.5 cm wide, and the element spacing is 7.0 cm. The simulated and measured return loss is shown in Figure 5.7. The standing wave at the higher frequency is possibly due to the method of calibration of the network analyzer, which did not calibrate the coax to twin line transition. The antenna has a 4:1 -10 dB bandwidth, with the operating range from 3.0 to 12.0 GHz. There is excellent agreement between the measured and simulated return loss from 1.0-6.0 GHz. At the higher frequencies

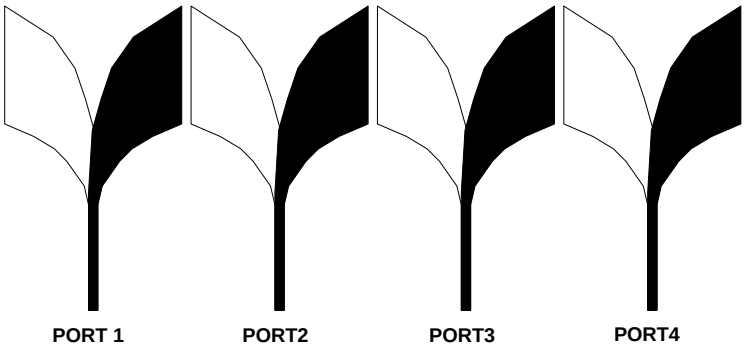

Figure 5.4. Sketch of linear four element sub-array, the array was built on a 1.57 mm thick $\epsilon_r = 3.6$ ComClad substrate. The antennas are 6.5 cm wide with a spacing of 0.5 cm.

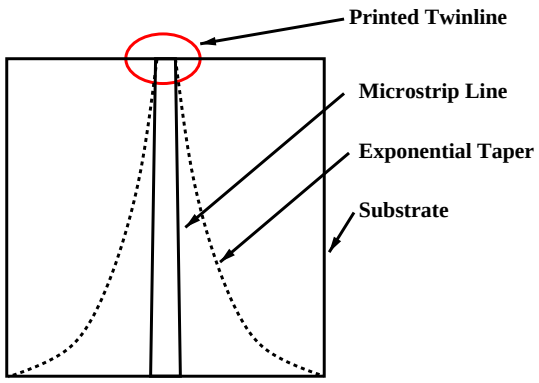

Figure 5.5. An exponential microstrip to printed-twinline balun. In the drawing the dotted lines denote the copper that is on the back side of the substrate.

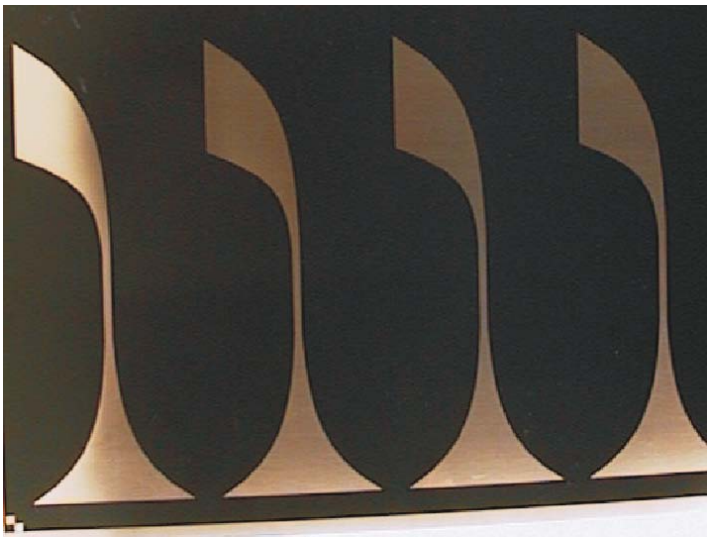

Figure 5.6. Picture of one side of a four element linear antipodal-slot Vivaldi antenna array, fabricated by the NFRA. The array was made using ComClad, a low cost plastic that was first used in the automotive industry.

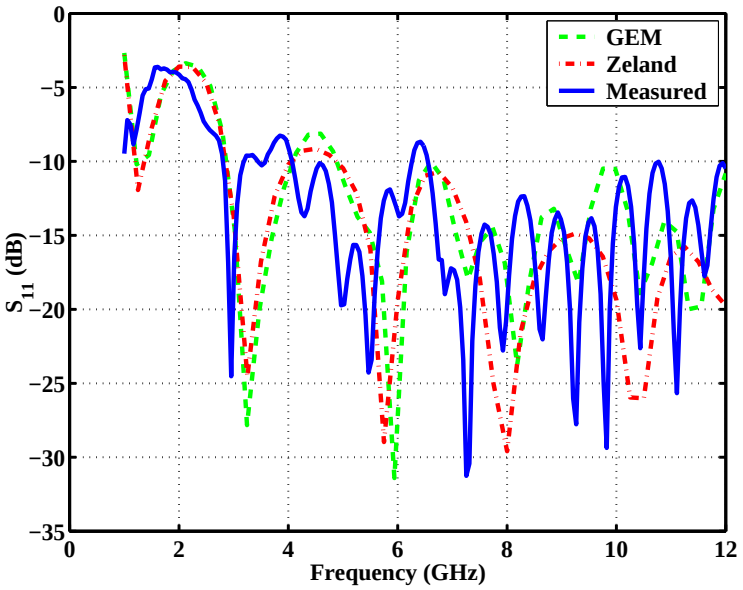

Figure 5.7. The measured return loss of a center element of the 4×4 antipodal Vivaldi array. The bandwidth (2:1 VSWR) of the array is from 3-12 GHz. There is good agreement between the simulated arrays and the measured arrays, especially at the lower frequencies.

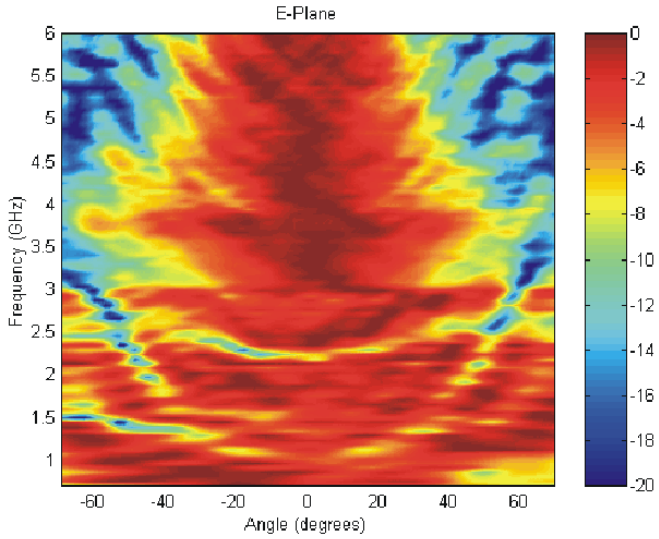

Figure 5.8. The measured radiation pattern of a single element of the four element array in the E-plane. The X-axis is the incident angle, the y-axis is the frequency (GHz). The radiation pattern of the antenna below 2.5ĠHz is almost omni-directions, above 2.5 GHz the radiation pattern narrows as the frequency is increased.

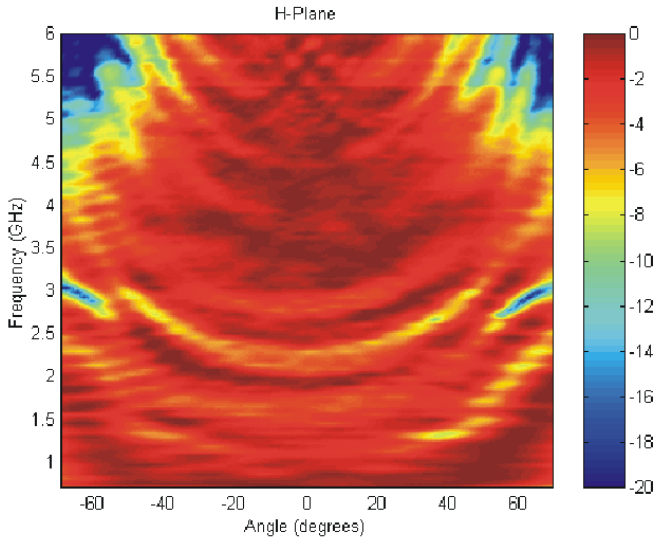

Figure 5.9. The measured radiation pattern of a single element of the four element array in the H-plane. The X-axis is the incident angle, the y-axis is the frequency (GHz). The H-plane is considerably broader then the E-plane. It is also an omni-directional radiator for the low-frequencies of operation.

of operation $f_o > 6.0\,\text{GHz}$ there is a standing wave in the s_{11} measurements, caused by using a coaxial-calibration instead of a TRL calibration. The element size at the lowest frequency of operation, $f_{low} = 3.0\,\text{GHz}$, is $0.65\,\lambda_o$, a spacing which would cause grating lobes in an array pattern.

The E-plane radiation pattern of the ComClad antenna is shown in Figure 5.8 and the H-Plane is shown in Figure 5.9. The 3 dB beam-width in the H-plane of the antenna at 6.0 GHz is 80°, and in the E-plane the beamwidth is 50°. As the frequency is lowered, the beam-width increases, because the electrical size of the antenna becomes smaller at the lower frequencies. At 3.0 GHz the H-plane beam-width is 140° and the E-plane's is 100°. These radiation patterns are not broad enough for horizon-to-horizon scanning of the main beam, which is one of the goals for SKA. The antenna's radiation pattern was also measured at frequencies lower then the impedance-matched bandwidth of the antenna. At these low-frequencies the antennas radiation pattern becomes extremely broadband, with a beam-width of 180° at the lowest frequencies, broad enough for horizon-to-horizon scanning.

The ComClad antenna was shown to have a large bandwidth of 4:1, and the simulation of the antenna agreed well with the measured results. The radiation pattern of the antenna is too narrow at the operating frequencies of the antenna and the pattern is broadbeam and uniform below the operating frequency.

5.3.2 Interconnected Arrays The ComClad array demonstrated a large bandwidth (4:1), however the size of the elements was is too large for a phased array environment, since a spacing of greater then $\lambda_o/2$ would lead to grating lobes in the array pattern. One of the goals for the next antenna design is a broadband element where the size of the antenna is less then $\lambda_\circ/2$ at the lowest frequency of operation. One method of achieving this is to increase the coupling of the elements at the lower frequencies. When the coupling is high in an array, neighboring elements in an array will load each other, thereby potentially lowering the return loss. One

drawback to this type of solution is that if the coupling is increased too much, the scan and noise performance of the array can be degraded (Section 6.2).

The coupling of the neighboring elements can be increased by decreasing the spacing of the antennas, or by physically connecting them. We chose to connect the arrays, since in the ComClad array the spacing was already very small, and the low-frequency performance was not improved. The connection can be either a short, capacitor, inductor or a resistor. For SKA a resistor cannot be used since it would degrade the noise performance of the array. The method that was used to increase the coupling was to physically connect neighboring elements of the array. In the coupled array, the antennas are physically connected by attaching the *right ear* of one Vivaldi to the *left ear* of its neighbor. The elements were connected to each other by alternating the array elements. Since the antipodal antenna has a radiating element on different sides of the substrate, if every other element is rotated the radiating elements will line up, as can be seen in Figure 5.10. By electrically connecting the antennas, the current, at low frequencies, can flow into the neighboring antennas radiating arm. This makes the antennas seem bigger at the low-frequencies of operation, distributing the current of a single antenna amongst its neighbors.

The exponential taper of the interconnected array is the same as that of the ComClad array, except that the size has been scaled by a factor of two. The measured return loss and coupling between two of the elements of the antenna is shown in Figure 5.11. The lowest operating frequency of the antenna is 0.8 GHz. The size of the antenna is $0.4\,\lambda_\circ$ at the lowest frequency vs $0.65\,\lambda_o$ for the ComClad array.

5.3.3 Interconnected Dual Polarization A dual polarized version of the interconnected antenna was also made, where each array element is again attached to the other elements, including its cross-pol neighbors. One connected

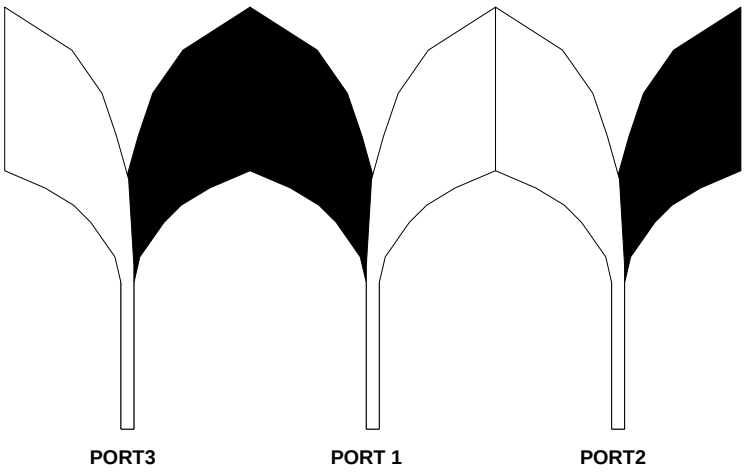

Figure 5.10. A sketch of the interconnected array, the solid colored radiating elements are on one side of the dielectric, the white ones are on the other. This antenna has a better low frequency performance because the neighboring antennas increase the effective size of the antenna

Figure 5.11. Measured return loss and coupling of the interconnected array. The 2:1 VSWR bandwidth of the antenna is from 800 MHz to 2.5 GHz. The coupling between neighboring elements is less then -20 dB from 1.0-2.5 GHz but increase to about -12 dB at the lowest frequency of operation of the antenna.

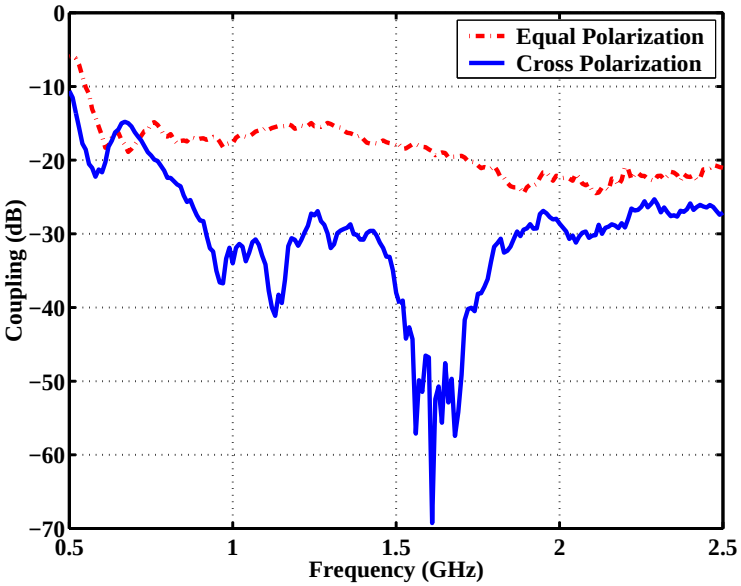

Figure 5.12: Measured coupling of dual-pol Vivaldi antenna array C.

element has the same polarization, and the other two are of an orthogonal polarization. The measured coupling between two elements is shown for both polarizations in Figure 5.12. The coupling between two co-polarized elements is lower -15 dB over the entire operating range of the antenna, dropping below -20 dB above 1.7 GHz. The cross-polar coupling is -15 dB from 0.7-0.8 GHz, but drops to below -25 dB over the rest of the operating range of the antenna. The return loss of the interconnected co-polarized array is the same as that of the linear interconnected array.

5.4 Antipodal dual frequency Array

In the previous section two antenna arrays were presented. They were both very broadband and were easy to construct. The ComClad antenna was too large for a phased array, but this problem was fixed in the interconnected array. The interconnected version showed that by combining the antennas into an array and using the neighboring antennas to load the elements, the low frequency performance of an array can be improved. The interconnected antenna's electrical size at the

lowest frequency is $0.4\lambda_{low}$. For an antenna with a 10:1 bandwidth, a spacing of $0.4\lambda_{low}$ at the low frequency would still be $4\lambda_{hi}$ at the highest frequency. This large spacing at the highest frequency will cause grating lobes in the main pattern. The solution that was proposed in Chapter 2 was to use a fractal layout, but it is not clear how to build a interconnected Vivaldi array using a fractal layout. The ComClad antenna is too big at $0.65\lambda_{low} = D$ to fit in a fractal array, because the spacing of a fractal array the size of an element should be about 0.5λ or less. We therefore decided to try to design another antenna using a different exponential taper to try and improve the low frequency performance of the array.

The first Vivaldi antennas that we made used an exponential taper design that was similar to those in the literature [20],[28],[23]. The antennas that we designed started with this type of taper. Optimizations were then performed to maximize the bandwidth. The results of the optimizations were discouraging because the low frequency of operation f_{cut} of the Vivaldi antennas was always limited by the size of the antenna, $f_{cut} > 2c/d$ where d is the width of the antenna. In order for a fractal-array to use Vivaldi, or antipodal-Vivaldi antennas, a design would have to be found for which the antenna worked at frequencies below this cut-off frequency.

There are two quantities that determine the *shape* of the Vivaldi antenna, the taper quantity α and the aspect ratio R, which is the ratio of the antennas height to width. The Vivaldi antenna's exponential taper is defined by:

$$y = \beta(e^{-\alpha x} - 1) \tag{5.2}$$

The exponential taper is shown in Figure 5.13. Here the curve E_1 is the function $y = \beta(e^{-\alpha x} - 1)$; the values L_1 and L_2 determine the aspect ratio $R = L_1/L_2$, and the variable β is chosen such that the exponential curve E_1 fits inside the box defined by L_1 and L_2. The curve E_2 is the same as E_1, only it is rotated so that its slope at zero is 90°, this is the rotated exponential that is used for the antenna simulations.

As $\alpha \to 0$ the antenna approaches a straight line, while as $\alpha \to \infty$ the

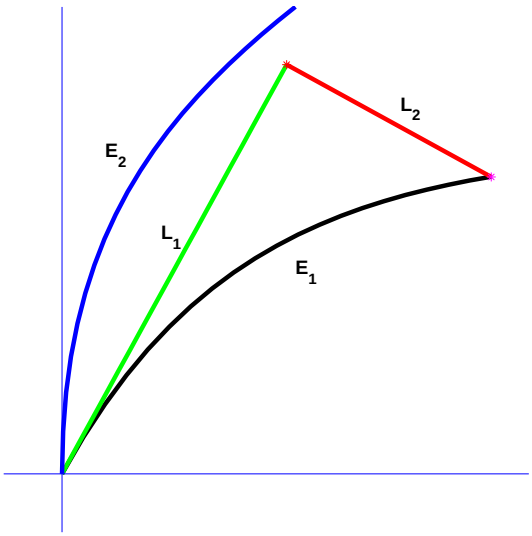

Figure 5.13. Exponential Taper of the Vivaldi Antenna. The amount of the taper was optimized for the antipodal antenna. L_1 is the height, and L_2 the width, the aspect ratio is L_1/L_2. The curve E_1 is the plot of the function $\beta(e^{\alpha x}-1)$, the curve E_2 is E_1 rotated so the slope at the origin is 90°.

exponential curve becomes a right angle. The variable α was swept from 25 to 2000, and for each value of α, an antipodal Vivaldi was simulated. An aspect ratio of 2 was chosen, with the width 8 cm and the height 16 cm. The antenna was simulated on a 20 mil substrate with a dielectric constant of ϵ_r=2.2. The frequency range of the simulations was from 0.5-3.5 GHz. For each value of α the return loss of the was antenna calculated.

The results of the parameter sweep are shown in Figure 5.14. In this figure α is plotted along the X-axis, and the frequencies are plotted along the y-axis. The color of the plot represents the return loss of the antenna and the black line represents the region of the antenna where the return loss is lower then -10 dB. From this figure it can be seen that the return loss of the antenna is below -10 dB for most of the higher frequencies of the antenna. There are two bands where the return loss is greater then -10 dB, the first starting at 2.5 GHz and $\alpha = 25$, and going up. The second band of greater return loss starts at 1.75 GHz and $\alpha = 200$, and these bands

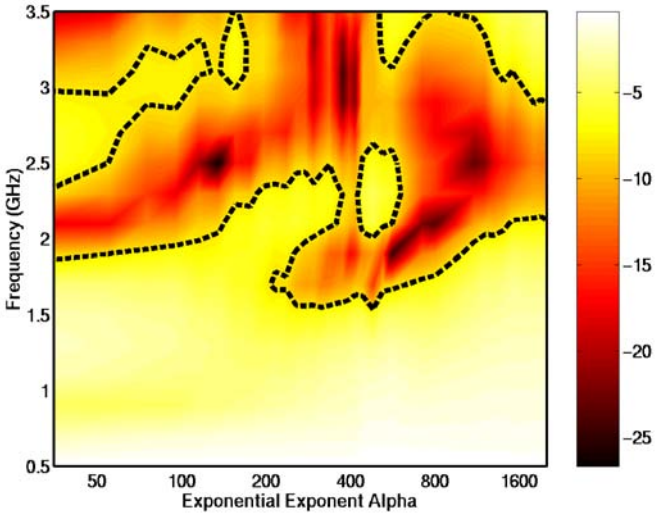

Figure 5.14. Exponential Taper of the Vivaldi Antenna. The amount of the taper was optimized for the antipodal antenna. The black line surrounds the -10 dB match

seem periodic with respect to α. These bands of poor return loss were seen in all the Vivaldi antennas that were built.

From the Figure 5.14 it can also be seen that there is a small window at the top of each of the bands where the return loss is lower then -10 dB. The second band has a rather large area where the antenna works well, from about $\alpha = 390$ to $\alpha = 410$ the antenna works over a very broad frequency range, from 1.5 GHz to over 3.5 GHz. This is a very narrow window in which the antenna works well: it has a large bandwidth and works well at the low-frequencies. The physical simulated size of the antenna at the lowest operating frequency is $0.4\lambda_{low}$.

This was a turning point in the study of the design of the antennas, because it showed the antenna's dependence on α. Up to this point the antennas that were built have had a values of alpha between 50 and 200, so when they were optimized, the value of alpha that would be found would be a local optimum between the two values, $\alpha = 150$. By performing the parameter sweep over all values of alpha, the global optimum value for α could be found, $\alpha = 400$.

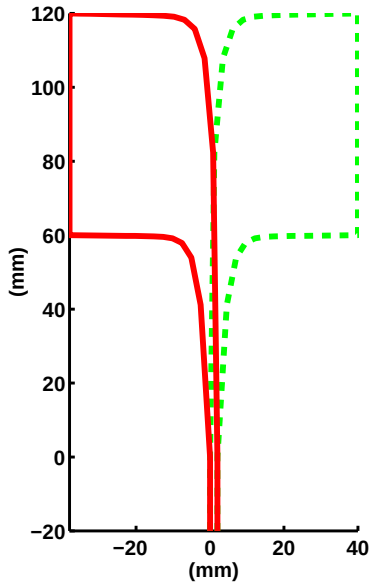

Figure 5.15. A sketch of the antipodal Vivaldi antenna. The solid line is the out line of the metalization on the front side of the substrate. The dashed line is on the backside of the substrate. The value of alpha for this plot was $\alpha = 400$, which was found to be the optimal value of alpha

5.4.1 Fabricated Improved Antipodal-Slot antenna An antenna was built using the optimized value of $\alpha = 400$, Figure 5.15. The antenna was built on a Duroid RT®/5440 substrate, h_{sub}=20 mil and $e_r = 2.2$. The return loss of the antenna is shown in Figure 5.16. The -10 dB bandwidth of the antenna is from 1.3-3.7 GHz. The size of the antenna at the lowest operating frequency is $0.35\lambda_{low}$, lower than even the interconnected Vivaldi array of the previous section.

The pattern of the new Vivaldi was measured over its entire frequency range. The E-plane plot is shown in Figure 5.17 and the H-plane in Figure 5.18. Because the physical size of the antennas is smaller, the beam-width of the antennas is larger. The E-plane 3 dB beam-width of the antenna is 120° at 1.5 GHz and tapers down to 40° at 3.5 GHz. The pattern of the H-plane is 180° from 1.5-2.7 GHz, and then narrows to 120° at 3.5 GHz. The radiation patterns at the low frequencies look very similar to those of a dipole antenna.

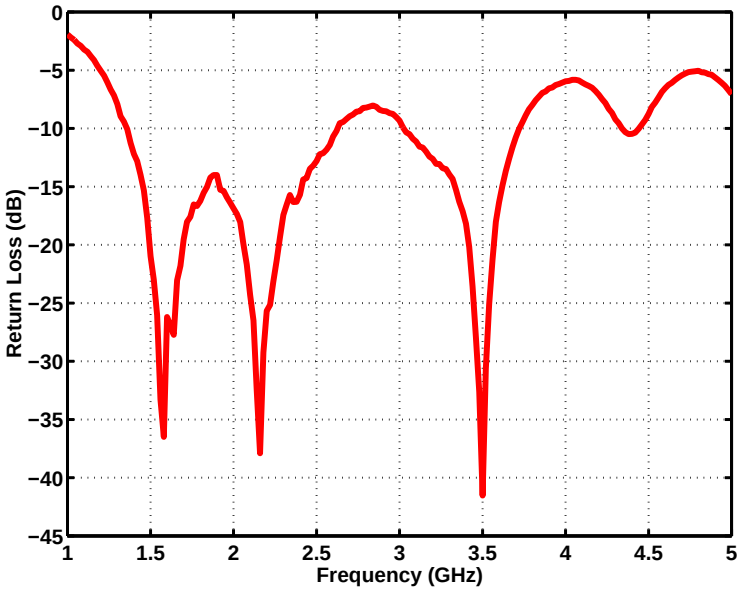

Figure 5.16. Return loss of the alpha-optimized antipodal Vivaldi antenna. The -10 dB bandwidth of the antenna is from 1.3-3.7 GHz. The size of the antenna at the lowest operating frequency is 0.35λ

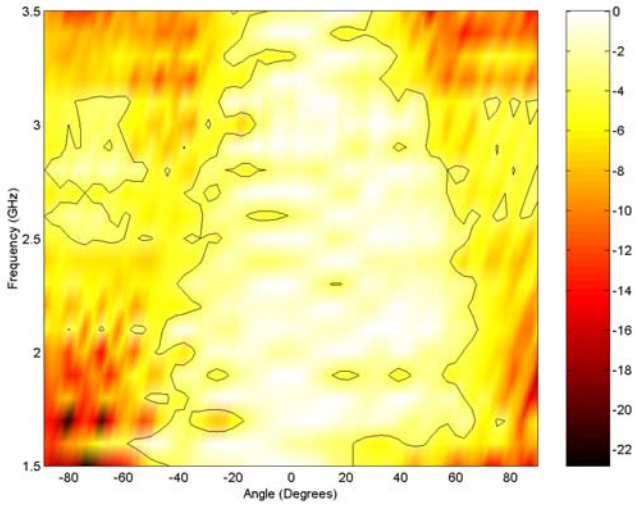

Figure 5.17. E-plane measurement of Vivaldi antenna from 2.0 GHz to 3.5 GHz. The black line denotes the 3 dB beam width.

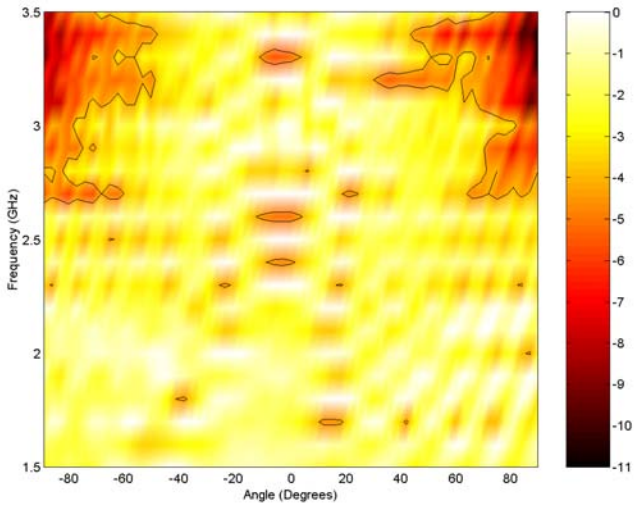

Figure 5.18. H-plane measurement of Vivaldi antenna from 2.0 GHz to 3.5 GHz. The black line denotes the 3 dB beam width.

5.4.2 Dual-Band Antipodal Antenna Array The antipodal antenna element designed in the previous section demonstrated the bandwidth and radiation pattern properties of a single element. The element must also be tested in an array so that its coupling between elements can be measured. The antenna was is used as the high-frequency element in a two level fractal array, consisting of 16 high-frequency elements, and four low-frequency elements, Figure 5.19. Both the low-frequency and high-frequency antennas were built over a ground-plane. A scaled antenna was used for the low-frequency antennas in the center of the array. The low frequency antenna was identical to the high-frequency antenna except that the dimensions of the radiating portion of the antenna were double the values of the high-frequency antenna. The low-frequency element was built on the same substrate as the high frequency element.

The return loss was measured for the antenna array, Figure 5.20. The -10 dB bandwidth of the large low-frequency element is from 750 MHz to over 5 GHz. The bandwidth of the small high-frequency element is from 1.3 GHz to 4.0 GHz,

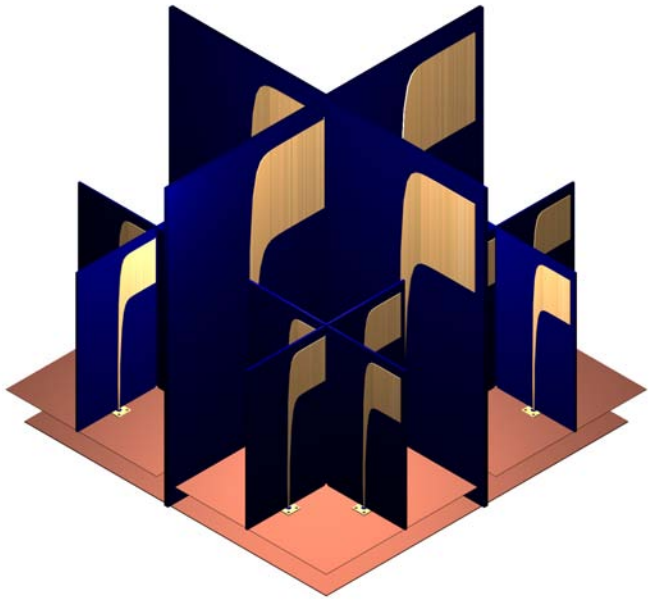

Figure 5.19. A drawing of a 20 element dual polarized two level fractal Vivaldi array. Each of the sub-arrays is above its own ground plane, so that it can be measured for different heights and spacings of the sub-arrays

meaning that the bandwidth of the large antenna is larger then that of the small antenna. This could be due to the scaling of the antennas, because the planar dimensions were scaled, while the substrate height was kept constant.

The small-antenna to small-antenna coupling and the large-antenna to large-antenna coupling is shown in Figure 5.21. The measured co-polar and cross-polar coupling of the small antenna is below -15 dB for the operating frequency of the small antenna. The co-polar and cross-polar coupling of the large antenna is also below -15 dB over the operating range of the antenna, and below -25 dB above 1.7 GHz.

The coupling between the large antennas and the small antennas was also measured, Figure 5.22. The co-polar coupling between the high-frequency antenna and the high-frequency antenna is below -20 dB over most of the frequency range of the antenna. There are two small points were the coupling rises to -18 dB at 0.95 GHz and 1.5 GHz. The cross-polar coupling is also very low, with a maximum

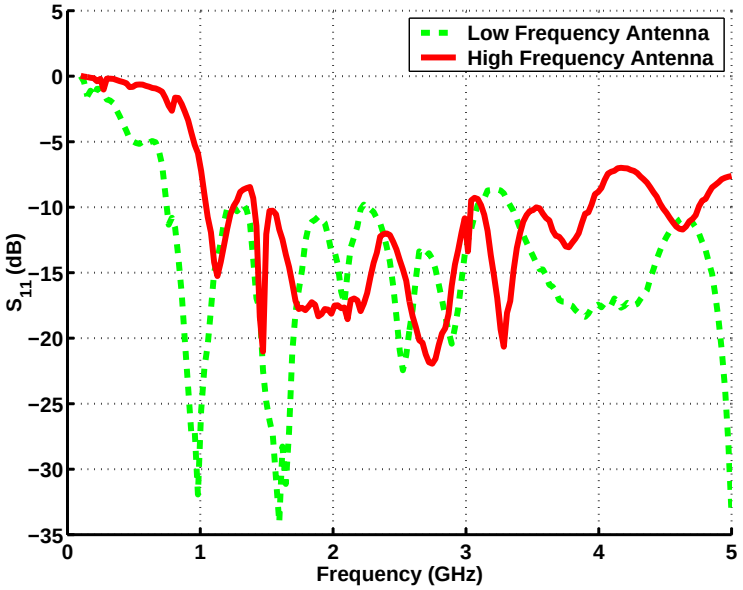

Figure 5.20. Measured Return loss of a dual band antipodal array. The low-frequency of operation of the large antenna is 0.75 GHz, and of the small antenna is 1.5 GHz. The upper limit of operation of the larger antenna is actually higher then of the small antenna.

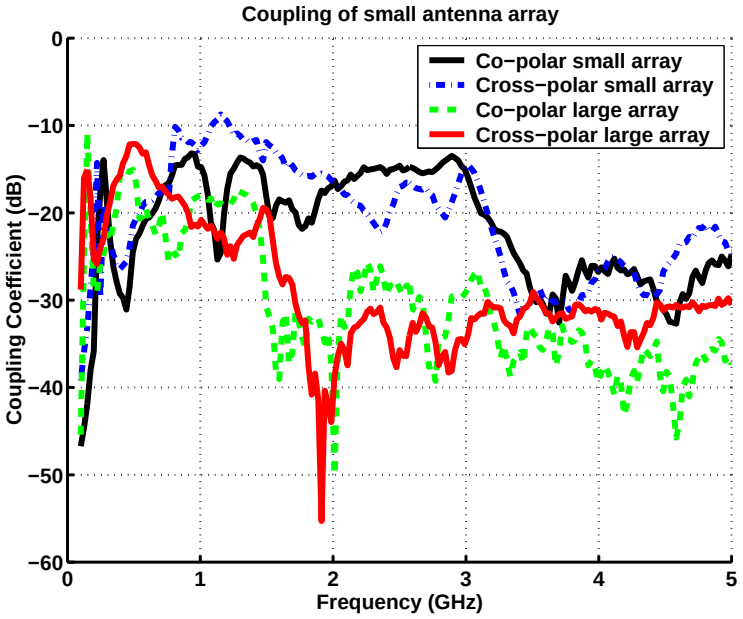

Figure 5.21. Measured co-polar and cross-polar coupling of the two frequency bands of the array. The coupling is less the -15 dB for each antenna in its operating frequency band, for both the co-polar and cross-polar coupling.

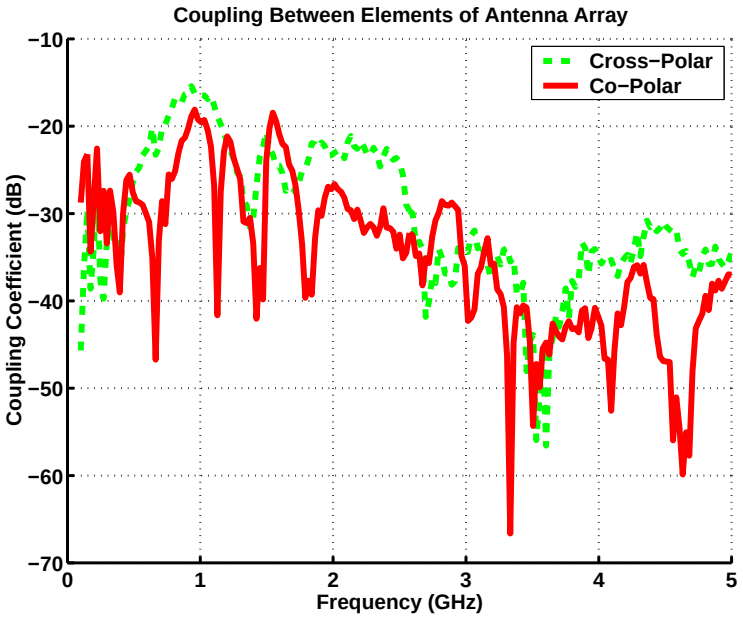

Figure 5.22. The Coupling between the two different band antennas. The coupling is lower the 15 dB over the entire bandwidth

of -15 dB at 1.0 GHz and below -20 dB over the rest of the bandwidth. It will be shown in the following chapter that a low amount of coupling not only improves the scan performance, but also improves the noise performance of the array.

Antipodal antennas were demonstrated to have a very large bandwidth. It was shown that by optimizing the tapper of the antipodal antenna, the low-frequency performance of the antenna could be improved. The antennas have a broad radiation pattern, due to their small size. The antennas are proved to have low coupling when placed in an array. The fractal array was also found to have a low coupling, both cross-pol and co-pol, as well as coupling between the different banded elements of the array.

CHAPTER 6

NOISE COUPLING IN ACTIVE ANTENNA ARRAYS

6.1 Introduction

In the Westerbork radio-telescope array in the Netherlands a two-element dipole array was used as the feed in a 25 m parabolic dish. When the dish was pointed to a dark (low-noise) region of the sky, a larger than expected noise temperature was measured [5]. This problem is attributed to noise coupling between the receiving dipoles and the LNAs. Noise that was generated at the input port of an LNA at one antenna feed was coupled through to the other antenna, and then amplified by the second LNA. The noise is coupled through the electromagnetic coupling between the array elements. The higher the coupling between the elements, the larger the potential noise coupling problem.

In phased array antennas, the spacing of the antenna elements is on the order of $\lambda_o/2$ at the operating frequency of the antenna. The close spacing of the elements can lead to high electromagnetic coupling between them, especially if the antennas are electrically small and have a broad beam width. The coupling between the elements is a function of the scan angle of the array, Section 6.2. This means that it will vary as the main beam of the antenna is scanned, and therefore the noise coupling will also be a function of the scan angle of the array.

In this chapter the noise performance of an array will be analyzed, first using a commercial microwave CAD tool, Agilent's Advanced Design System 1.3 (ADS 1.3), and secondly using an analytical approach. The analytical approach

includes the variations in the noise coupling that occur when the main beam of the array is scanned. In order to perform the analytical analysis of the noise, the scan reflection coefficient of the array must first be derived, which is done in the following section. The chapter uses many different variables and a list of them is given in Table A.1 and Table A.2 for clarity.

6.2 Scan Reflection Coefficient of an Array

For a phased array the S-parameters do not give a full description of the array as they do not describe how the array performs when it is scanned. The scan reflection coefficient is a parameter that characterizes the performance of an array as a function of the scan angle of the main beam.

6.2.1 Passive Reflection and Coupling Parameters There are two types of wave variables that are defined for a port i in a microwave network, the incident wave a_i, and the reflected wave b_i. At the i-th port of a multi-port network, the incident and reflected waves variables are given by:

$$a_i = \frac{V_{i+}}{\sqrt{2Z_{oi}}} \tag{6.1}$$

$$b_i = \frac{V_{i-}}{\sqrt{2Z_{oi}}}, \tag{6.2}$$

where V_{i+} and V_{i-} are forward and backward propagating (peak) voltage waves at the n-th port of a multi port network. The impedance Z_{oi} is the characteristic impedance of the n-th port. The average power delivered to the i-th port is:

$$P_i = \frac{1}{2}|a_i|^2 - \frac{1}{2}|b_i|^2, \tag{6.3}$$

the power going into the port, $|a_i|^2/2$, minus the power leaving the port, $|b_i|^2/2$.

A scattering matrix can then be used to relate the incident and reflected waves at all ports as:

$$S\vec{a} = \vec{b} \tag{6.4}$$

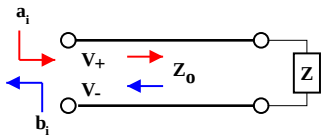

Figure 6.1. The definition of a wave variable in terms of the in-going and out-going voltages and the characteristic impedance. In this figure the wave variables are defined as voltages, however, they can also be defined for systems in which voltages cannot be defined, eg. Waveguides.

where $\vec{a}$ and $\vec{b}$ are column vectors composed of the wave variables Eq.6.1 and Eq.6.2 respectively. The elements of the matrix, S, are defined as:

$$s_{i,m} = \frac{b_m}{a_i} \tag{6.5}$$

where:

$$a_l = 0 \text{ for } l \neq m. \tag{6.6}$$

The scattering parameters of a microwave network can be found numerically using a standard microwave simulation package, or they can be measured using a network analyzer. The scattering parameters of a microwave network are measured with all non-excited ports terminated with their characteristic impedance, so that Eq.6.6 is satisfied..

6.2.2 Characteristics of a Scanning Array Scattering parameters are passive, they are measured with only one port excited, Eq.6.6, and all the other ports terminated in Z_{on}. A phased array can also be analyzed using a forced excitation, Figure 6.2.2 [31]. In the forced excitation, all the ports are excited with incident waves. The out-going waves are then measured at all the ports to find the *scan coupling parameters*. The scan coupling parameters are also some times called the active coupling parameters, but throughout this chapter they will be referred to as scan coupling parameters. The scan coupling parameters, specifically the scan reflection coefficient, are used to analyze the characteristics of a phased array under scanning of the main beam. The *scan reflection coefficient* characterizes an element

in a phased array under scanning conditions. Incident waves with a given amplitude and phase are applied at all the elements of the array such that the antenna has a main beam in a given direction.

Like the standard reflection coefficient, the scan reflection coefficient, also called the active reflection coefficient, of an array is the ratio of the outward traveling wave to the input wave at a port i. For the scan reflection coefficient, $\Gamma(\theta, \phi)$, the elements of the array are excited with incident waves such that the main beam of the antenna is oriented in the direction (θ, ϕ). The scan reflection coefficient can be defined at each element of the array. Generally, it is defined relative to the center element of an array, or for an infinite array. In a finite array, the scan reflection coefficient can be calculated from the passive scattering parameters of the array (S). For an infinite array the scan reflection coefficient can be calculated by taking a limit.

For a phased array to have a beam in the direction (θ, ϕ), each element of the N-element transmitting array needs to be excited by a phase (β_i) and amplitude (γ_i). These input waves can be written combined in the vector $\vec{a}(\theta, \phi)$, which is a function of θ and ϕ:

$$\vec{a}(\theta, \phi) = \begin{bmatrix} \gamma_1 j\beta_1 \\ \gamma_2 j\beta_2 \\ \vdots \\ \gamma_i j\beta_i \end{bmatrix}. \tag{6.7}$$

The values of the amplitude are generally chosen so that $\gamma_i = \gamma_k = 1$, as this insures that unique phases β_i's can be found for each scan angle of the main beam. If the amplitudes are left free, then there is no unique solution for a beam in a given direction, and there is no unique scan reflection coefficient for a fixed scan angle of the array. The reflected waves $\vec{b}$ at all of the antenna ports (elements) are

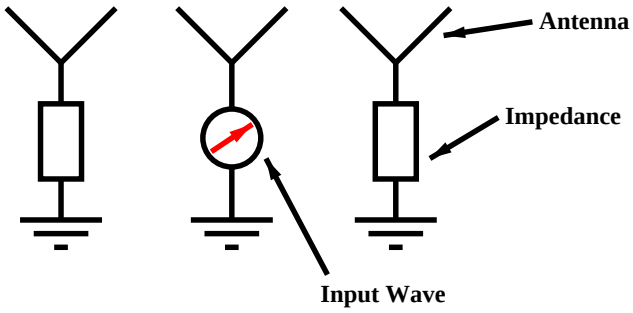

(a)

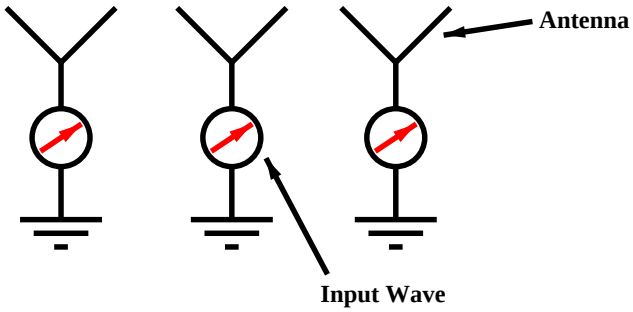

(b)

Figure 6.2. A drawing of two ways in which to analyze an antenna array. (a) The passive method, in which all ports are terminated in Z_o and only one port is excited for each measurement. (b) The forced excitation, in which all elements are excited with waves.

$$\vec{b}(\theta,\phi) = S\vec{a}(\theta,\phi) = \begin{bmatrix} s_{1,1} & s_{1,2} & \cdots & s_{1,m} \\ s_{2,1} & s_{2,2} & \cdots & s_{2,m} \\ \cdots & \cdots & \cdots & \cdots \\ s_{k,1} & s_{k,2} & \cdots & s_{k,m} \end{bmatrix} \begin{Bmatrix} e^{j\beta_1} \\ e^{j\beta_2} \\ \vdots \\ e^{j\beta_m} \end{Bmatrix}. \tag{6.8}$$

The vector $\vec{b}$ is a function of θ and ϕ, the scan angle of the array.

The scan reflection coefficient of the i-th element of a m element array is:

$$\Gamma_i(\theta,\phi) = \frac{b_i(\theta,\phi)}{a_i(\theta,\phi)}, \tag{6.9}$$

where b_i is :

$$b_i = \sum_{l=1}^{m} S_{i,l} a_l. \tag{6.10}$$

The value $b_i(\theta,\phi)$ is equal to the inner product of the ith row of the matrix S, denoted by $S(i,:)$, with the vector $\vec{a}(\theta,\phi)$. This gives the short hand notation of the scan reflection coefficient at element i as:

$$\Gamma_i(\theta,\phi) = \frac{< S(i,:), \vec{a}(\theta,\phi) >}{e^{j\beta_i}} \tag{6.11}$$

The denominator of the fraction in Eq.6.11, has a magnitude of one, so the norm of the scan reflection coefficient is given by the norm of the inner product.

$$|\Gamma_i(\theta,\phi)| = | < S(i,:), \vec{a}(\theta,\phi) > | \tag{6.12}$$

An array performs well under scanning when the scan reflection coefficient has a small amplitude, i.e., when the near-field coupling between elements is low for all scan angles. Angles for which the scan reflection coefficients are high, are called the blind scan angles of the array. This occurs when the ratio of the energy coupled to the energy transmitted by an element is large.

6.3 Noise in Microwave Circuits

The signals that are detected by radio telescopes are very low in power, and often the spectral power densities of the incoming waves that are measured are

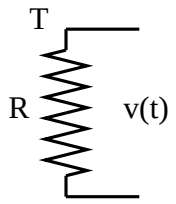

Figure 6.3. A sketch of a resistor where the noise voltage between the terminals is a function of the bandwidth, temperature, frequency and resistance.

on the order of micro-Jansky's, where a Jansky is 10^{-26}Watt/(m^{2}Hz). If there were no noise present, then it would be possible to detect any signal no matter how low the power, simply by amplifying the signal. Noise however, is present in all antennas and receivers. To improve the receiving capabilities of an antenna, the sources of the noise must be understood and analyzed. There are many sources of noise for a radio telescope, including man-made noise such as broadcast television, radio, cell phones and satellite communications. There is also noise which is generated by the active elements of the array, amplifiers, phase shifters and analog to digital converters, as well as the noise that is produced by lossy elements, such as transmission-lines and lossy antennas [32]. These internal sources of noise will lower the sensitivity of the antenna array.

In LNAs the primary source of noise is shot noise [33], which is noise due to the random fluctuations of charge carriers. Flicker noise or $1/f$ noise is also present, but in lower power levels. Most quantities of noise in active devices are related to the noise of a resistor, since this noise is well understood. The noise voltage of a resistor, Figure 6.3, can be calculated using Planck's black body radiation law. The average voltage is zero, but the RMS voltage has a value given by:

$$v = \sqrt{\frac{4hfBR}{e^{\frac{hf}{k_bT}} - 1}}. \tag{6.13}$$

The values of the constants are given in Table.6.3, if the the value $hf/kt << 1$ then this can be simplified using using the first two terms of the Taylor series of e^x, the

Variable	Value	Units	Name
h	6.546×10^{-34}	$J/dotS$	Planck's constant
k_b	1.308×10^{-23}	J/K	Boltzmann's constant
T	-	Kelvin	Degrees Kelvin
B	-	Hertz	Bandwidth of The Noise
f	-	Hertz	Frequency
R	-	Ω	Resistance

Table 6.1. Definition of the quantities that are used to calculate the noise power in a resistor

equation to:

$$v = \sqrt{4k_bTBR}. \tag{6.14}$$

This is known as the *Rayleigh-Jeans approximation*. Using this approximation the maximum noise power that can be delivered to a load is

$$P = \left(\frac{v}{2R}\right)^2 R = k_bTB. \tag{6.15}$$

The SNR of a microwave circuit is the ratio of the desired component of the signal to the noise. The ratio of SNR at the input of a 2-port network to the SNR at the output, is called the noise figure of a microwave network, defined as:

$$NF = \frac{E_i/NS_i}{E_o/NS_o}, \tag{6.16}$$

where E_i and E_o are the signal powers and NS_i and NS_o are the noise powers at the input and output ports respectively. For an amplifier with a gain of G, this simplifies to:

$$NF = \frac{NS_o}{GNS_i}. \tag{6.17}$$

For a noiseless network, the output noise NS_o is the product of the gain and the input noise. No noise is added by the system, so the noise figure is unity or 0 dB. For a noisy network the noise figure will always be larger than one. By definition NS_i is taken to be the noise generated by a matched resistor at room temperature $T_o = 290K$. LNAs are also characterized using a temperature instead of the noise

figure. The noise temperature is frequently used in low noise applications, like radio-astronomy receivers. The effective temperature T_e is the temperature of the matched resistor that would have the same noise power as the LNA at its output port. The relationship between effective temperature and noise figure is given by:

$$T_e = (NF - 1)T_o \tag{6.18}$$

For a noiseless network T_e would be 0K.

The noise figure of a microwave network is often measured using the Y-parameter method. In this method the network is connected to two noise sources, a hot source with a noise temperature of T_{hot}, and a cold source with a temperature T_{cold}. The output power of the system is then measured for the two different sources:

$$P_{hot} = (Gk_bT_{hot} + Gk_bT_e)B \tag{6.19}$$

$$P_{cold} = (Gk_bT_{cold} + Gk_bT_e)B. \tag{6.20}$$

The ratio of the two powers is the Y-factor:

$$Y = \frac{P_{hot}}{P_{cold}} = \frac{T_{hot} + T_e}{T_{cold} + T_e}, \tag{6.21}$$

and solving for T_e gives:

$$T_e = \frac{T_{hot} - YT_{cold}}{Y - 1}. \tag{6.22}$$

This method only works when Y is sufficiently large or when the hot source is much hotter then the cold source $T_{hot} >> T_{cold}$. In Figure 6.4 several error curves are plotted, where the horizontal axis is the ratio of the temperature of the hot source to the cold source, T_{hot}/T_{cold} ,and the vertical axis is the relative error calculated temperature $(\tilde{T}_e - T_e)/T_e$. The different curves represent different measurement errors for the Y-factor. From the graph it can be seen that as the ratio of the temperature of the hot source to that of the cold source increases the error decreases. The acceptable ratio of the noise sources depends on the amount of error in the measurement of the Y-factor.

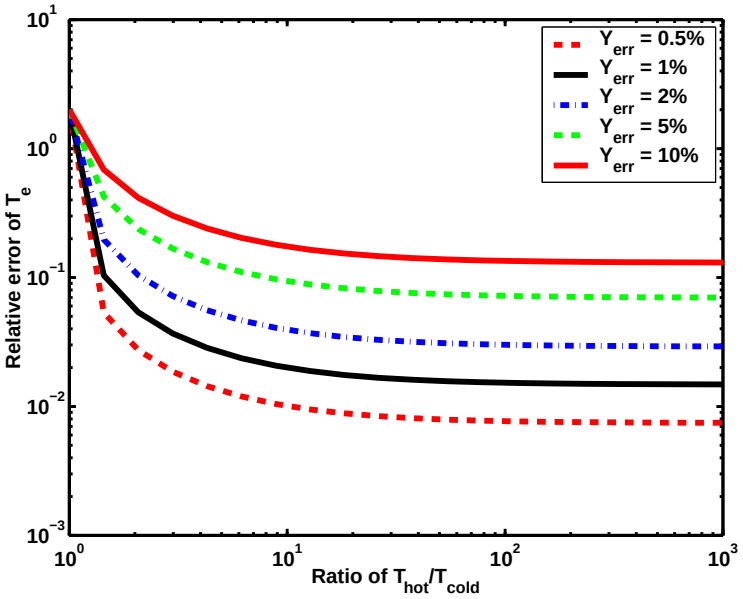

Figure 6.4. A calculation of the errors that are made when using the Y-Factor method to find the effective noise temperature. The five different lines represent different percentage errors that are made when the Y-factor was calculated. The vertical axis is the ratio of the hot-to-cold source, and the horizontal axis is the relative error made in the calculation of the effective temperature. From the graph it can be seen that as the ratio temperatures of the noise sources increases, the amount of error decreases.

6.4 Characterization of Noise Using Noise Waves

The standard definition of the scattering parameters given in Eq.6.4, does not include a way of characterizing noise in a microwave circuit. The use of scattering parameters can be extended by adding noise waves. A resistor, R, will produce thermal noise over the entire spectrum, which can be written as a random variable $v(t)$. If the noise is confined to a small bandwidth Δf, around a fixed frequency $\overline{f}_o$, it can be written in phasor notation, using $\overline{\omega} = 2\pi\overline{f}_o$, and the mean propagation constant $\overline{k}$ at the frequency $\overline{f}_p$. Where the bar denotes the mean within the bandwidth Δf. The noise phasor, at a port i, is:

$$v_{i-}(t) = C(t)e^{j\phi(t)}e^{j\overline{k}z}. \tag{6.23}$$

The random variables $C(t)$ and $\phi(t)$ describe the RMS amplitude and phase of the wave envelope. If $\Delta f << \overline{f}_o$, the functions $v_{i-}(t)$ and $C(t)$ will become slowly varying functions. A normalized noise wave can then be defined as:

$$c_i = c_i(t) = \frac{v_{n-}(t)}{\sqrt{Z_o}}, \tag{6.24}$$

where the minus sign denotes travel in the $-z$ direction. The noise wave c_i is the time average of the noise voltage normalized by the square root of the characteristic impedance. The power of a noise wave is given by $|c|^2$, where the time average power $\overline{|c|^2}$is given by:

$$\overline{|c|^2} = \lim_{t\to\infty} \frac{1}{2t} \int_{-t}^{+t} |C(\tau)|^2 d\tau. \tag{6.25}$$

A representation of a microwave network with noise waves or indeed any impressed sources can be written as:

$$\vec{b} = S\vec{a} + \vec{c}. \tag{6.26}$$

The vector $\vec{c}$ represents the noise waves emanating from the ports of a noisy microwave network. In Eq.6.26 the noise wave $\vec{c}$ can be thought of as the noise radiating from the device when there is no input power, $\vec{a} = 0$. This is not technically correct since it ignores the noise radiated by the terminating ports.

The noise waves are time-varying complex random variables characterized by a correlation matrix COR_m given by [34]:

$$COR_m = \begin{pmatrix} \overline{|c_1^2|} & \overline{c_1 c_2^*} & \dots & \overline{c_1 c_m^*} \\ \overline{c_2 c_1^*} & \overline{|c_2|^2} & \dots & \overline{c_2 c_m^*} \\ \vdots & \vdots & \vdots & \vdots \\ \overline{c_m c_1^*} & \overline{c_m c_2^*} & \dots & \overline{|c_m|^2} \end{pmatrix} \tag{6.27}$$

where the $\overline{c_i c_l^*}$ components of the matrix are:

$$\overline{c_i c_l^*} = \lim_{t\to\infty} \frac{1}{2t} \int_{-t}^{+t} c_i(\tau) c_j^*(\tau) d\tau. \tag{6.28}$$

The over-bar represents a time averaging, with an implicit assumption of ergodicity and jointly wide-sense stationary processes [35].

The benefit of noise wave analysis is that it brings noise and noise analysis into a framework that is familiar to most microwave engineers. By using noise waves along with scattering parameters we can create simple solutions to complicated noise problems. The ability to accurately measure the scattering parameters improves the accuracy of the noise models. In the next section an extensive analysis of noise coupling in phased arrays will be made using the noise wave characterization of the noise generated by LNAs.

6.5 Noise Coupling

The mechanism of noise coupling in active antenna arrays is described schematically in Figure 6.7. Noise is generated by an LNA both at its input and output ports. The noise that is generated at the input port of the LNA radiates and couples to the other antenna elements, contributing to their total received noise power. The noise coupling coefficients, $N_c(\theta, \phi)$, are a function of the scan angle, since the relative phase between elements changes as the array is scanned. In this section, we show that the noise coupling is proportional to the scan reflection coefficient $\Gamma(\theta, \phi)$ of the array. This conclusion is reached using both physical and mathematical arguments. The usefulness of the conclusion lies in the fact that $\Gamma(\theta, \phi)$ is an easily measurable quantity, so the noise coupling for antenna arrays can now be calculated.

6.6 Noise models using commercial Microwave Software

Most commercial microwave-CAD (Computer Aided Design) packages contain tools for the simulation of noise. The method that these packages use to simulate the noise uses either a current or voltage source for a noise generator. The noise that

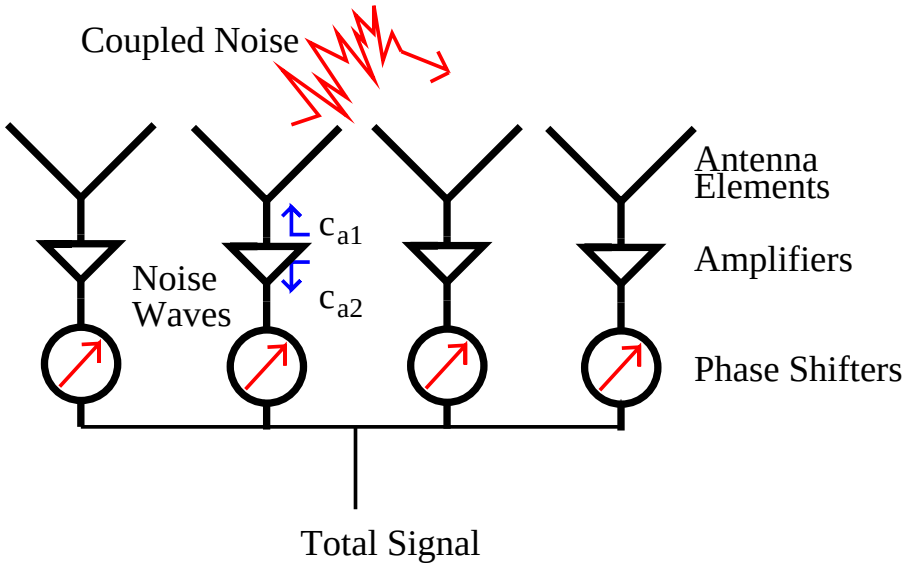

Figure 6.5. Illustration of noise coupling in the receive part of a phased array antenna. The noise waves at each LNA input and output are c_1 and c_2, respectively. The incident and scattered waves, a_i and b_i, are used to define the scan reflection coefficient.

is generated by the noise sources is cascaded through the network using circuit analysis techniques. Many times the method of the noise analysis is not published, and it is not clear what type of noise characterization is used. Agilent's ADS 1.3 (Advanced Design System), was used to model the noise coupling between two antenna elements. Three different noise models were used to model the noise: an S-parameter model; a current model; and a large signal circuit model.

These models were used in a simulation of a two-element dipole array. One element of the array was attached to a noisy LNA, the second to a noiseless LNA. The simulation then calculated the noise at the output of the noiseless LNA. Since this LNA did not generate any noise, all noise present at this port must be due to the coupling of the noise from the first LNA. The two-element antenna array was replaced with an S-parameter representation of the array. The noise coupling was then calculated for two different matching networks, a power match and a noise match.

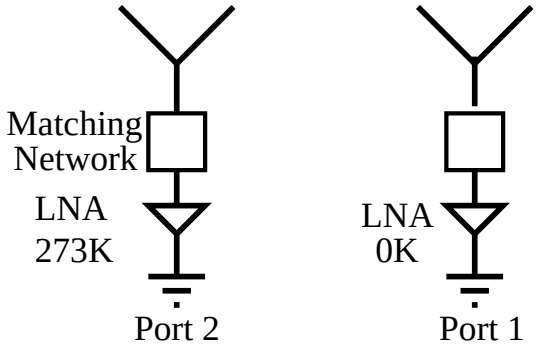

Figure 6.6. A schematic representing the noise simulation. Two amplifiers are placed in a two-element dipole array, one of the LNAs is noisy (273 K), the second produces no noise (0 K)

LNAs were attached to each port of the scattering matrix of the antenna one LNA being noisy (273 K) and one noiseless (0 K), Figure 6.6. The noises at the output port of the noiseless LNA and noisy LNA were simulated. By finding the ratio of the noise voltages at the two output ports of the LNAs we could determine the amount of noise that was coupled from one antenna to the other.

6.6.1 S-Parameter Models The first model that was used was an S-parameter model. This model uses the scattering parameters of an LNA, as well as the noise parameters Γ_{opt}, R_{min} and NF_{min}. These parameters are available from the specification sheets of most LNAs, making this type of model easy to use. The method that ADS uses to calculate the noise is not given, most likely this is proprietary. This was one of the reasons for using different noise models.

6.6.2 Current and MOS-FET Models The second method used to calculate the noise coupling was a FET noise model derived by Philips [36], *PML-ED02AH*. This model used two correlated current noise sources added to the S-parameter model of a FET. This noise model uses noiseless S-parameters and two noise generators I_g and I_d, as well as three noisy resistors, the drain resistance R_d, the gate resistance R_g and the source resistance R_s. The values of the noise sources are functions of both the physical and electrical parameters of the LNA. The current

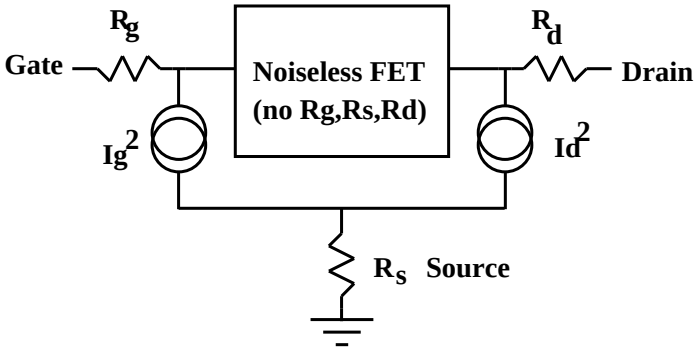

Figure 6.7. Illustration of the current noise model (PML ED02AH) this model used two correlated current noise sources, along with a noiseless S-parameter model. The model is used in ADS to simulate the noise of an LNA.

source I_g obeys:

$$\bar{i_g^2} = Q_{in} W f^2 + 2qI_{gs}10^{-3}\Delta f, \tag{6.29}$$

where the value of Q_{in} is:

$$Q_{in} = 4k_b T_o \Delta f \mathcal{A}_i 10^{-23} \left[1 + \frac{X}{\mathcal{B}_i}\right]. \tag{6.30}$$

The value of current source I_d is:

$$\bar{i_d^2} = Q_{out} W + \frac{\mathcal{K}_f}{[Ids10^{-3}]^{\mathcal{A}_f}} f, \tag{6.31}$$

where the value of Q_{out} is:

$$Q_{out} = 4k_b T_o \Delta f \sqrt{X\mathcal{A}_o 10^{-3} + X^2 \mathcal{B}_o 10^{-6}}. \tag{6.32}$$

The values of all of the variables of the preceding equations are given in Table.6.6.2. The script letters denote the unit-less parameters that were provided by the model specifications. There is no available information to explain how this model is derived, or to describe some of the values of the unit-less parameters in the second column of Table.6.6.2.

6.6.3 MOS-FET model The third model used in the noise simulation was a large signal model for a MOS FET LNA, seen in Figure 6.8. This model was written by the NFRA to model the noise of a MOS-FET. Like the current source

General Parameters		*PML-ED02AH* Specific parameters	
f	operating frequency (Hz)	$\mathcal{A}_i$	2.0
W	total gate width in mm	$\mathcal{B}_i$	120
T_o	Temperature in K	$\mathcal{A}_o$	0.8
k_b	Boltzmann's Constant	$\mathcal{B}_o$	4.0
q	Electron Charge (C)	$\mathcal{A}_f$	1.0
X	ids/W (mA/mm)	$\mathcal{K}_f$	10^{-11}
Δf	Bandwidth (Hz)	ids	DC source current

Table 6.2. The values of the parameters in the definition of the current noise sources in Eq.6.29 and Eq.6.31

noise model, the MOS-FET model of the noise contains many parameters which are not generally known for specific LNAs.

6.6.4 Results of the commercial Simulation Tools The results of the three different types of noise models are shown in, Table 6.6.4, P1 is the noise at the output port of the noiseless LNA, while P2 is the noise at the output port of the noisy LNA. The simulations were performed using both a power matched network as well as a noise matched LNA. The values of the noise voltages, P1 and P2, are given in $nV/\sqrt{Hz}$. The values of the noise-coupling ratio (NCR) differ significantly for the three models, from high of -5 dB for the noise matched S-parameter model to -23 dB

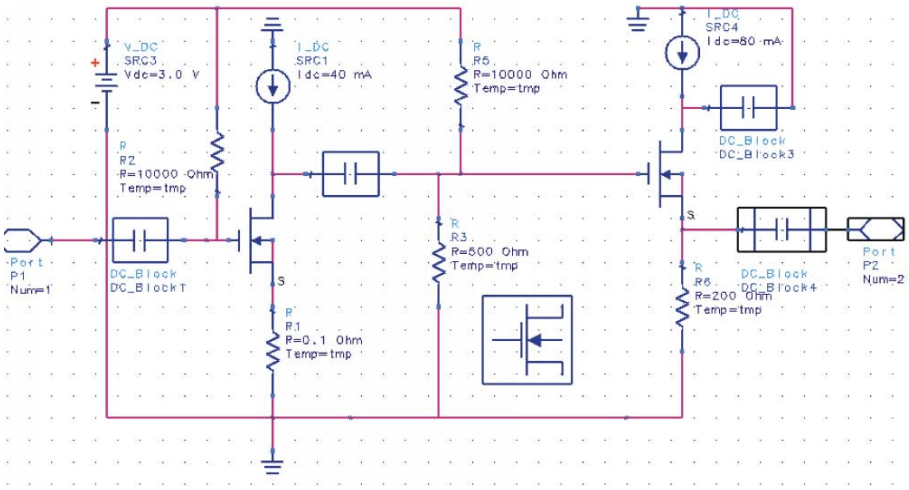

Figure 6.8. A schematic of a large signal model of a MOS-FET. This model was designed by the NFRA.

		S-Parameter	Noise Source Model	MOS model
Noise Matched	P1	0.50	0.10	0.24
	P2	1.30	1.42	0.72
	NCR	-5 dB	-23 dB	-15 dB
Power Matched	P1	0.87	0.15	0.35
	P2	1.80	1.44	0.80
	NCR	-6.3 dB	-19 dB	-7 dB

Table 6.3. Noise coupling in a two element dipole array, P1 and P2 are the noise in $nV/\sqrt{Hz}$ at ports one and two. P1 is the noiseless LNA, P2 is the noisy LNA. The Power Matched uses a matching circuit that optimizes the Gain of the LNA, the noise match optimizes the SNR ratio. The CNR is the coupled noise ratio.

for the current source noise matched model. The amount of noise that was coupled in the noise match case was lower in all three simulations. Since all three models gave different results for the amount of noise coupling and for the NCR, we felt that a more systematic theoretical approach was needed. Such an approach would allow us to control what models are used, and what simplifications are made.

6.7 Analytical Analysis of the Noise

In this section an analytical method will be used to calculate the noise coupling of a phased array under scanning. Two different approaches will be used. The first will assume that the LNA is matched to the antenna, whereas the second will not assume a match. The noise will be calculated for an N-element array with arbitrary spacing, Figure 6.9. The LNAs are assumed to have a noise wave c_1 at the input port and c_2 at the output port.

6.7.1 Noise in a Gain-Matched Array The goal of this section is to find the Noise Coupled Ratio (NCR), which is the ratio of the coupled noise to the non-coupled noise. One element of the array will be noisy, the rest will be noiseless (0 K), as shown in Figure 6.9. For most arrays the noisy element is placed in the center of the array, the i-th element. A noise wave is inserted into the array at the i-th element, and its coupling to the other elements are found from the scattering

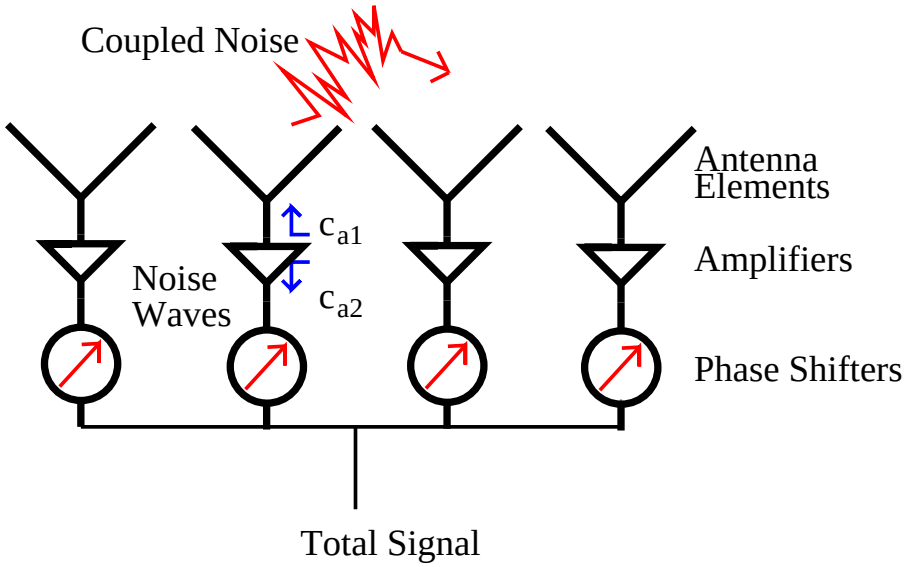

Figure 6.9. A sketch of the noise coupling of a phased array, the LNAs are modeled with two noise waves, the noise wave at the input port c_{a1} of the LNA and the wave at the output port c_{a2}. The noisy LNA is connected to the ith antenna element, with all other antenna elements connected to noiseless LNAs.

matrix:

$$\vec{c^c} = S \begin{bmatrix} 0 \\ \vdots \\ c_{a1} \\ \vdots \\ 0 \end{bmatrix}. \tag{6.33}$$

The vector $\vec{c^c}$ represents the out-going noise waves at each array elements feed, this is the noise coupled from the noisy LNA at port i. The noise waves $\vec{c^c}$ are then amplified by the LNAs. Assuming that all LNAs have equal voltage gains, G, the coupled noise vector at the output of the LNAs is $GS(i,:)c_{a1}$ at the output the ports of the LNAs.

After the LNAs, the received signal and the noise must be phase shifted to steer the main beam. For a main beam in the direction (θ, ϕ) a phase β_k is added to all waves incident on the kth element. Note that the phase shifts added to the

noise waves are the same as those of the input wave $\vec{a}$ used for the calculation of the active reflection coefficient, Eq.6.1. The coupled noise wave at the output of the i-th phase shifter:

$$c_i^c(\theta,\phi) = c_{a2} + Gc_{a1}S_{i,n}e^{j\beta_n} \tag{6.34}$$

The coupled noise waves at the output of all the phase shifters are then combined into a single signal, c_{tot}, which is written as:

$$\begin{aligned} c_{tot}(\theta,\phi) &= c_{a2} + \sum_{k=1}^{N} Gc_{a1}S_{i,k}e^{j\beta_k} && (6.35)\\ &= c_{a2} + Gc_{a1} < S(i,:), \vec{a}(\theta,\phi) > . && (6.36) \end{aligned}$$

Substituting Eq.6.11 for the active reflection coefficient gives

$$c_{tot}(\theta,\phi) = c_{a2} + Gc_{a1}\Gamma_i(\theta,\phi). \tag{6.37}$$

The total noise coupling as a function of the scan angle is directly proportional to the active reflection coefficient. The proportionality constant is given by c_{a1} and G, which are properties of the specific LNA, and can be calculated from the specification sheets provided by the manufacturer ($\Gamma_{opt}, R_n, NF_{min}$). The noise coupling ratio NCR is defined as the ratio of the noise due to c_{a1} to the noise due to c_{a2}:

$$NCR = \frac{N(c_{a1})}{N(c_{a2})}. \tag{6.38}$$

For a phased array with a main beam at (θ,ϕ), the noise coupling ratio is:

$$NCR = \frac{c_{a1}G\Gamma(\theta,\phi)}{c_{a2}}. \tag{6.39}$$

This relationship can be calculated from measurable quantities, thereby giving a method for calculating the noise coupling of an active antenna array.

6.7.2 Noise in a Noise-Matched Array In the previous section, the amplifiers were assumed to be power-matched to the antennas at the input, and the noise match was not taken into account. We now show that the noise coupling that was found in Eq.6.37 is a first order approximation to the rigorous solution. In the receive array with integrated LNAs, the noise characteristics of the array can be derived from the noise characteristics of the amplifier along with the s-parameters of the amplifier and array. To include the noise match in the active array, consider the N element array, Figure 6.10, where each of the elements is attached to an LNA. The N-port labeled S_A in the figure represents the antenna feeds. The feed ports are connected to N amplifier input ports. These amplifiers are not necessarily matched to the antennas; usually a noise match will be used. The N output ports of the LNAs are connected to the phase shifter network. The calculation of the scattering matrix of the active array S_{net}, is performed by cascading the scattering matrix of the antenna array S_A with that of the individual amplifiers S_{LNA}, where:

$$S_{LNA} = \begin{bmatrix} s_{11} & s_{12} \\ s_{21} & s_{22} \end{bmatrix}. \tag{6.40}$$

The scattering matrix of the N amplifiers can be rewritten as a $2N \times 2N$ block diagonal matrix S_{Amp}, where the diagonal blocks are S_{LNA}:

$$S_{Amp} = \begin{bmatrix} S_{LNA} & 0 & \cdots & \cdots \\ 0 & S_{LNA} & 0 & \cdots \\ \cdots & \cdots & \cdots & \cdots \\ \cdots & \cdots & \cdots & S_{LNA} \end{bmatrix}. \tag{6.41}$$

The fist step in calculating the noise of the cascaded system is to group the matrices of the two multi-ports into a single scattering matrix:

$$\begin{Bmatrix} \vec{b}_{Amp} \\ \vec{b}_A \end{Bmatrix} = \begin{bmatrix} S_{Amp} & 0 \\ 0 & S_A \end{bmatrix} \begin{Bmatrix} \vec{a}_{Amp} \\ \vec{a}_A \end{Bmatrix}. \tag{6.42}$$

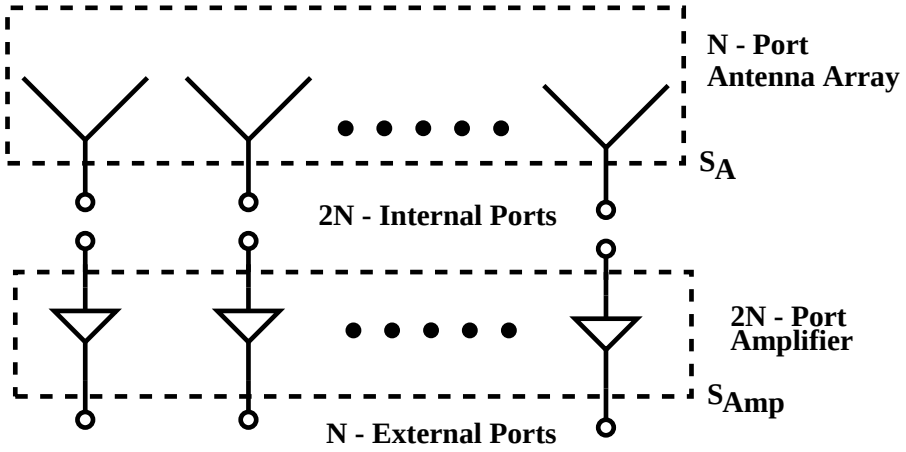

Figure 6.10. Multi-port representation of the connection of an N-element antenna array to N amplifiers. When evaluating the noise coupling, the internal ports are connected, reducing the size of the problem to $N \times N$.

The ports of the cascaded system can now be separated into internal and external ports. Internal ports are only connected to ports inside the system, and have no direct connection to the outside. External ports are not connected to internal ports, and only connect to the outside of the system. The internal and external ports of the active array are shown in Figure 6.10. The rearranged total scattering matrix, with internal and external ports separated is:

$$\begin{bmatrix} \vec{b}_E \\ \vec{b}_I \end{bmatrix} = \begin{bmatrix} S_{EE} & S_{EI} \\ S_{IE} & S_{II} \end{bmatrix} \begin{Bmatrix} \vec{a}_E \\ \vec{a}_I \end{Bmatrix}, \tag{6.43}$$

where the interior wave variables are defined as, shown in Figure 6.10:

$$\vec{a}_I = \begin{Bmatrix} \vec{a}_{I_1} \\ \vec{a}_{I_2} \end{Bmatrix} \tag{6.44}$$

and

$$\vec{b}_I = \begin{Bmatrix} \vec{b}_{I_1} \\ \vec{b}_{I_2} \end{Bmatrix} \tag{6.45}$$

as shown in Figure 6.11.

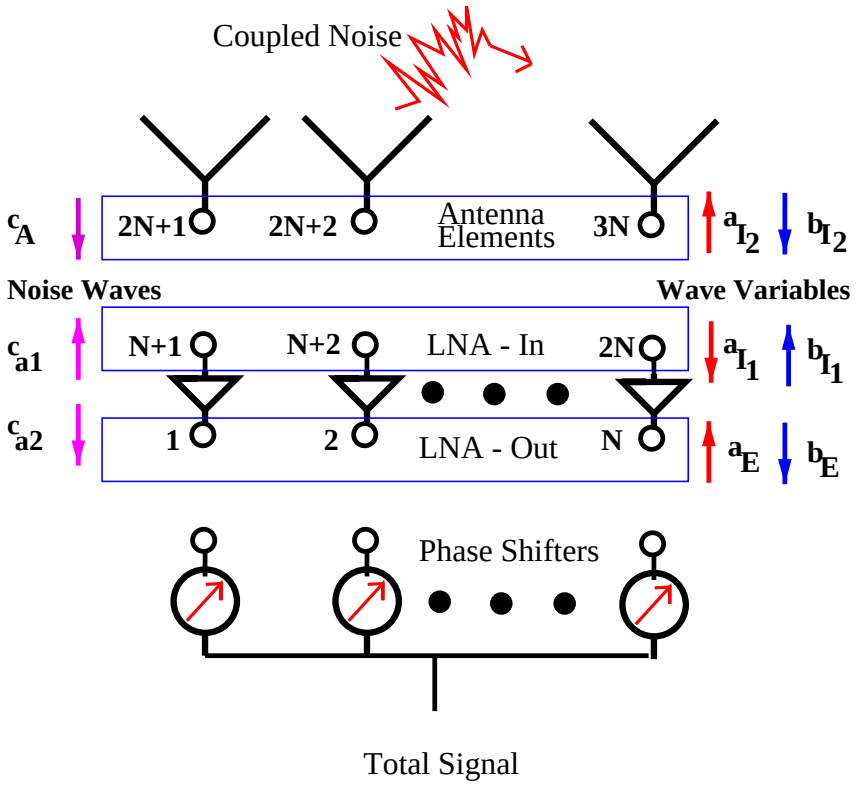

Figure 6.11: Figure describing the direction of the waves from Eq.6.43.

In Eq.6.43 the sub-matrices S_{II}, S_{EE}, S_{EI} and S_{IE} are:

$$S_{EE} = [s_{22}I] \in \mathcal{C}^{N\times N} \tag{6.46}$$

$$S_{II} = \begin{bmatrix} s_{11}I & 0 \\ 0 & S_A \end{bmatrix} \in \mathcal{C}^{2N\times 2N} \tag{6.47}$$

$$S_{IE} = \begin{bmatrix} s_{21}I \\ 0 \end{bmatrix} \in \mathcal{C}^{2N\times N} \tag{6.48}$$

$$S_{EI} = \begin{bmatrix} s_{12}I & 0 \end{bmatrix} \in \mathcal{C}^{N\times 2N} \tag{6.49}$$

$$\tag{6.50}$$

The values s_{11}, s_{12},s_{21} and s_{22} are from the scattering parameters of the LNA. The N port scattering matrix S_{net} for the N port active antenna array can now be derived

from the formula:

$$S_{net} = S_{EE} - S_{EI}(S_{II} - \Lambda)^{-1} S_{IE} \tag{6.51}$$

The noise coupling $\vec{c}_{net}$ is:

$$\begin{aligned} \vec{c}_{net} &= \left[\begin{array}{c|c} I & S_{EI}\left(\Lambda - S_{II}\right)^{-1} \end{array} \right] \left[\begin{array}{c} \vec{c}_E \\ \vec{c}_I \end{array} \right] && (6.52) \\ &= \vec{c}_E + S_{EI}\left(\Lambda - S_{II}\right)^{-1} \vec{c}_I && (6.53) \\ &= \vec{c}_E - S_{EI}\left(S_{II} - \Lambda\right)^{-1} \vec{c}_I && (6.54) \end{aligned}$$

Where Λ is the connection matrix with all elements zero except $\Lambda_{im} = 1 = \Lambda_{mi}$, when port m is connected to port i, for the active antenna. In other words, $\Lambda_{i,i+N} = 1 = \Lambda_{i+N,i}$. The elements of the connection matrix physically represent the waves at the internal ports. The connection matrix, Λ of the N-element array with N-amplifiers is:

$$\Lambda = \left[\begin{array}{cc} 0 & I \\ I & 0 \end{array} \right] \tag{6.55}$$

In Eq.6.52 the value of $\vec{c}_I$ is

$$\vec{c}_I = \left[\begin{array}{c} \vec{c}_{a1} \\ \vec{c_A} \end{array} \right], \tag{6.56}$$

a combination of the noise at the input ports of the LNAs, and the noise of the antenna array, Figure 6.11. The antennas will be assumed to be perfectly conducting, and therefore will have zero noise so $\vec{c}_I$ is:

$$\vec{c}_I = \left[\begin{array}{c} \vec{c}_{a1} \\ \vec{0} \end{array} \right]. \tag{6.57}$$

The equation for C_{net}, Eq.6.52 includes the inverse of the matrix $(S_{II} - \Lambda)$. This matrix can be written in block form as:

$$(S_{II} - \Lambda) = \left[\begin{array}{cc} s_{11} I & -I \\ -I & S_A \end{array} \right]. \tag{6.58}$$

To find the inverse of this matrix, we solve the following equation:

$$\begin{bmatrix} s_{11}I & -I \\ -I & S_A \end{bmatrix} \begin{bmatrix} B_1 & B_2 \\ B_3 & B_4 \end{bmatrix} = \begin{bmatrix} I & 0 \\ 0 & I \end{bmatrix}. \tag{6.59}$$

After calculating the matrix product, we have four equations with four unknowns:

$$s_{11}B_1 - B_3 = I \tag{6.60}$$

$$s_{11}B_2 - B_4 = 0 \tag{6.61}$$

$$S_AB_3 - B_1 = 0 \tag{6.62}$$

$$S_AB_4 - B_2 = I. \tag{6.63}$$

Solving these equations for the values of the B_is we have:

$$B_1 = S_A(s_{11}S_A - I)^{-1} \tag{6.64}$$

$$B_2 = (s_{11}S_A - I)^{-1} \tag{6.65}$$

$$B_3 = (s_{11}S_A - I)^{-1} \tag{6.66}$$

$$B_4 = s_{11}(s_{11}S_A - I)^{-1}. \tag{6.67}$$

Substituting the values for B_i into Eq.6.52 and simplifying:

$$\vec{c}_{net} = \vec{c}_{a2} - \begin{bmatrix} s_{21}I & 0 \end{bmatrix} \begin{bmatrix} B_1 & B_2 \\ B_3 & B_4 \end{bmatrix} \begin{bmatrix} \vec{c}_{a1} \\ \vec{0} \end{bmatrix} \tag{6.68}$$

$$= \vec{c}_{a2} - B_1\vec{c}_{a1} \tag{6.69}$$

$$= \vec{c}_{a2} - S_A(s_{11}S_A - I)^{-1}\vec{c}_{a1}, \tag{6.70}$$

where $\vec{c}_{a1}$ and $\vec{c}_{a2}$ represent N input and output amplifier noise waves, respectively. This is now a complete solution for the noise at the output ports of the active antenna array. For the case of a gain-matched amplifier, $s_{11} = 0$, Eq.6.52 simplifies to $\vec{c}_{net} = \vec{c}_{a2} + s_{21}S_A\vec{c}_{a1}$, the same value derived using the approximate approach from Section.6.7.1.

For the noise-matched LNA, the inverse of $I - s_{11}S_A$ is still present in Eq.6.52. Since S_A represents a passive network, the eigenvalues of S_A satisfy $\hat{\lambda}_i \leq 1$. Because the reflection coefficients at the input of the amplifier, s_{11}, are also less then one, the eigenvalues of the matrix $s_{11}S_A$ must satisfy $\lambda_i << 1$ and therefore:

$$[I - s_{11}S_A]^{-1} = I + s_{11}S_A + s_{11}^2 S_A^2 + \cdots , \tag{6.71}$$

which combined with Eq.6.52 gives:

$$\vec{c}_{net} = \vec{c}_{a2} + s_{21}S_A \left[I + s_{11}S_A + s_{11}^2 S_A^2 \cdots \right] \vec{c}_{a1}. \tag{6.72}$$

Therefore, for small values of the input mismatch, Eq.6.72 reduces to Eq.6.36 in the first approximation, validating the simple approach of calculating noise coupling presented in the previous section.

6.8 Example of Noise Coupling in a 49-Element Dipole Array

As an illustration of the usefulness of the presented noise coupling theory, consider a 7×7 half-wave dipole array. The full scattering matrix of the array is calculated with a Method of Moment (MoM) integral equation solver [7]. The array consists of 49 half wavelength dipoles above a ground plane in a rectangular 7×7 grid with a $0.55\lambda_0$ period. The scan reflection coefficient is calculated as described in Section.6.2.

As observed from Eq.6.39, the LNA noise figure, noise resistance and optimal noise match directly affect the noise coupling coefficients. For this example, we assume that a Hewlett Packard MGA-82563 low-noise amplifier is connected to each of the 49 dipoles. The noise parameters for this LNA at 1.0 GHz are, $NF_o = 2.10$dB, $\Gamma_{opt} = 0.15\angle 45^o$ and $R_N = 6.0$, and the gain is 14. dB. Using formulas given in [37], magnitudes of the noise waves are found to be $|c_1| = 5.4023 \cdot 10^{-11}\,\mathrm{V}/\sqrt{Z_o}$ and $|c_2| = 3.2690 \cdot 10^{-10}\,\mathrm{V}/\sqrt{Z_o}$, and the ratio $|c_1/c_2| = 0.1653$ [35].

An interesting figure of merit is the amount of coupling that produces a 50% increase in the noise power at the output of the array. To find the minimum amount of coupling that would give the noise ratio of −3dB, we set:

$$10 \log \frac{|\Gamma(\theta, \phi) G c_1|^2}{|c_2|^2} = -3 \text{ dB}. \tag{6.73}$$

Using Eq.(6.36) we can solve for the minimum scan reflection coefficient that would give a noise coupling ratio of greater then -3 dB. The voltage gain of the LNA is 5.0, and the ratio of the noise waves is 0.17. We then solve

$$\Gamma G c_1 / c_2 = -3\text{dB}, \tag{6.74}$$

which yields $\Gamma = 0.86$ or -1.4 dB. This is not very hard to achieve practically, however gain larger than 14 dB is usually of interest. An LNA with a higher gain would have a significantly lower threshold of acceptable Γ_i that would yield a coupling ratio of less then 3 dB. A row of the magnitudes of the scattering matrix S_A is shown in Fig.6.12, showing the level of coupling between the elements as calculated by the MoM. Figure 6.13 shows the scan reflection coefficient, and therefore the noise coupling of the center element of the array. The light areas in the plot show high coupling for the corresponding scan angle, indicating that practical scanning is limited in the E-plane to a relatively small field of view.

The scan reflection was also calculated for a 7×7 dipole array with an array spacing of λ_0. In this case, as expected, the noise coupling is much smaller, and for low noise coupling one should choose an array with larger element spacing. Unfortunately, this will limit the scan angle due to grating lobes. For example, for a beam scanned in the E-plane to 45^o, the half-wavelength spacing array has no grating lobes and a noise coupling ratio of 0.64. However, an array with full wavelength spacing and a noise coupling ratio of 0.3 will have a grating lobe at -15^o when the main beam is scanned to 45^o. Therefore, there is a tradeoff in designing low-noise scanning arrays: when the noise coupling is low, the scan angle is limited, and

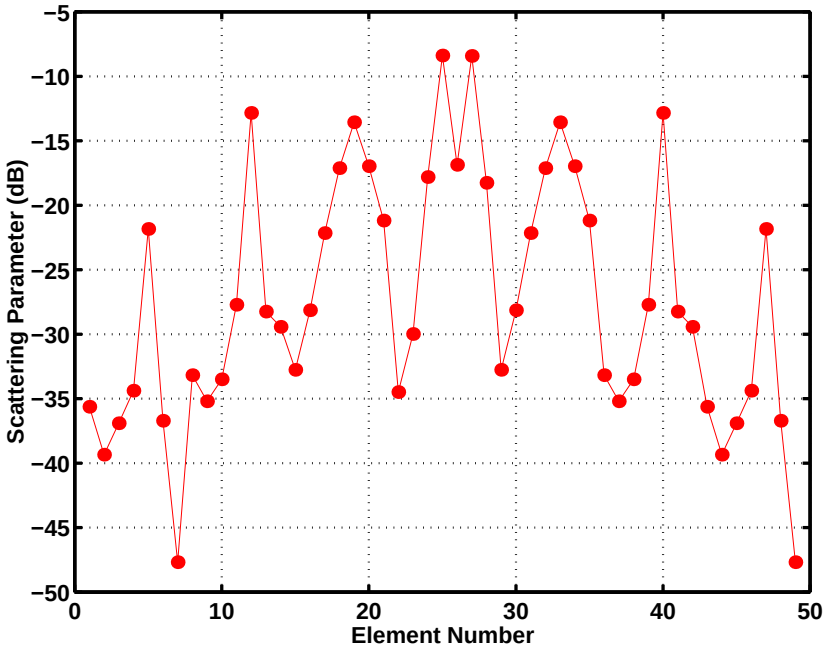

Figure 6.12. Magnitude of elements in a single row of the scattering matrix S_A of a 7×7 dipole array as calculated by a MoM code. The relative magnitudes indicate levels of near-field coupling between elements.

when the scan angle is wide, there can be significant noise coupling at the large scan angles. Design parameters that can be adjusted for minimizing the noise coupling are the antenna element radiation pattern, LNA properties, and array lattice.

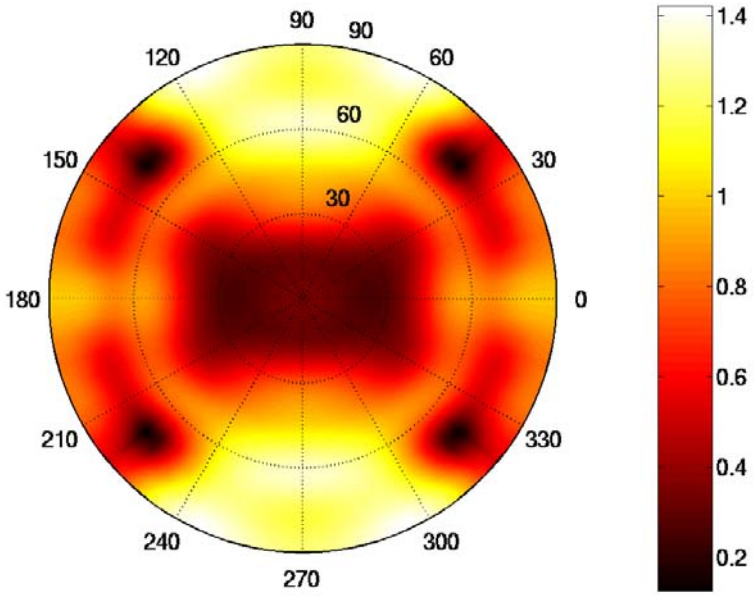

Figure 6.13. Plot of the magnitude of the scan reflection coefficient for the center element of a 7×7 dipole array with a $\lambda_0/2$ spacing. The polar plot represents the scan angles as azimuth (represented as the angle from 0-360) and elevation (represented as the radius of the circle). The dipole is oriented in the 180^o-0^o direction.

CHAPTER 7

CONCLUSION

7.1 The Fractal Array

The fractal array has been demonstrated to be a good candidate for a large bandwidth phased array. It has cost benefits over an array of small antenna elements. The fractal was shown to have a low element-to-element coupling and optimal array spacing for each frequency band. The fractal array has been shown to be a good compromise between using small elements and using large elements. The fractal array makes most efficient use of the available space, it does not populate the area with small elements with poor radiation efficiency. It also allows for all elements to be spaced at the optimal distance in each frequency band. Because the elements are space $\lambda/2$ apart at each frequency, the coupling of a fractal array is also lower then of a small element array.

7.1.1 Printed Log-Periodic Array The Printed Log-Periodic Dipole Array (LPDA) demonstrated a large simulated bandwidth, 1.5-2.5 GHz. The radiation patterns of the printed LPDA have a broad-beamwidth and are uniform over the frequency range of the antenna. The LPDA provides an ideal way to integrate an LNA, using the antenna itself as both the gate and drain bias, this is important because the bias lines often increase coupling between antenna elements. The antenna also has cost benefits over the wire version of the Log-periodic antenna, because it can be etched onto a low cost substrate, and mass-produced.

7.1.2 Slot Fed Vivaldi Antenna The slot fed Vivaldi antenna has a broadband width 4.0-7.8 GHz, as well as a broad beamwidth, 60^o, antenna. Different methods of feeding the antennas were studied, with the best type of feed found to be a radial slot feed. The antennas have a low coupling when placed in an array. The feed of the antennas was found to be the limiting factor in the bandwidth of the antennas.

7.1.3 Antipodal Vivaldi Antennas In order to improve the feed of the Vivaldi antenna, as well as use a lower dielectric constant substrate, the antipodal antenna arrays were studied. The first antipodal antenna array that was built used a low-cost plastic substrate. This antenna had a very large bandwidth 3.0-12.0 GHz, but the antenna size was 0.67λ at the lowest frequency. This large a spacing would lead to grating lobes in a phased array. To improve the banwidth of the antennas the coupling between neighboring elements was increased. This was done so that neighboring elements could load an antenna element, there by improving the low frequency performance. By connecting neighboring elements, the size of the antennas at the low operating frequency was reduced to 0.4λ.

A new antipodal antenna was designed. This antenna was designed using a parameter sweep from α=25 to 200. The variable α determines the *curvature* of the exponential taper $y = \beta(e^{\alpha x} - 1)$. It was found that there is a small window where the antenna has an optimal performance, that is, where the antenna is electrically small and still has a large bandwidth. The new antipodal antenna had a bandwidth from 1.3-4.0 GHz, and its size at the lowest frequency of operation was 0.35λ. The antipodal antenna also demonstrated a large beamwidth, 120^o in the E-plane and 180^o in the H-plane.

A two tier fractal array was built using the new element. The fractal array demonstrated a low coupling between all the elements, for both the co-polar coupling and the cross-polar coupling.

7.2 Noise Coupling in Phase Arrays

In the chapter on noise coupling, a new concept of noise coupling was introduced. Noise coupling occurs in a phased array when the noise at the input port of an LNA is radiated by the antenna, and received by the other antenna elements of the array. This noise is then amplified and added back into the signal. We attempted to model the noise coupling using commercially available CAD software, but were unsuccessful. Each of the three un-successful models used predicted different behavior for the noise coupling.

We the proposed a method of characterizing the noise based on analytical techniques. We showed that the noise coupling ratio in a phased array is proportional the active reflection coefficient of the array, when the LNAs are power matched to the antenna. We also derived and analytical approximation to the noise coupling if the antennas are not matched to the LNAs. It was shown that the case where the LNAs are matched to the antennas is a first order solution to the non-matched case.

7.3 Future Work

We felt that the reason that the LPDA did not work as designed was due to the limitations of the fabrication process that we have in the laboratory. Different methods of fabrication of the printed LPDA should be studied, to improve its bandwidth. This antenna seems very promising for a broadband array element, since it has a broadbeam and a broadband width. The ease of integration of LNAs also makes it an ideal candidate of the SKA antenna.

Future work on this project would include the integration of LNAs into the fractal-antipodal antenna array. When the NFRA placed LNAs into the array of small Vivaldi antennas, it started to oscillate. It is not clear whether this is due to the coupling between the elements or if it is due to the antenna impedance being outside of the region of stability of the LNA.

Future work on the noise coupling work would involve testing the theory in an actual array. The problem with experimentation is that it would be exceedingly difficult to measure the noise performance of a large phased array. The benefit of the theory is that it allows for the prediction of the noise coupling before the array is built, and therefore it can be used to optimize the noise performance of a phased antenna array.

BIBLIOGRAPHY

[1] John D. Kraus, **Radio Astronomy**, Cygnus-Quasar Books, Powell, OH, 1986.

[2] Arnold van Ardenne, "The SKA technical R&D program at NFRA," **NFRA Newsletter**, , no. 15, pp. pp 1–7, September 1998.

[3] Kristen Rohlfs, **Tools of Radio Astronomy**, pp. 132–134, Springer-Verlag, Berlin, 1986.

[4] Arnold van Ardenne, "Concepts of the square kilometre array; toward the new generation radio telescops," **IEEE Trans. Ant. and Prop.**, vol. 1, pp. 158–161, 2000.

[5] Bert Woestenburg and Jaap Bergman, **Private Communications**, Netherlands Foundation for Reasearch in Astronomy, 1999.

[6] Daniel H. Schaubert and Tan-Huat Choi, "Wideband vivaldi arrays for large aperature antenna," **Perspectives on Radio Astronomy: Technologies for Large Antenna Array**, pp. 49–58, 1999.

[7] B. D. Popović, **CAD of wire antennas and related radiating structures**, John Wiley & Sons, Inc., New York, 1991.

[8] Branislave Notaros, B. D. Popovic, Jan Peeters Weem, Robert Brown, and Zoya Popovic, "Efficient large-domain MoM solution to electrically large practical em problems," **IEEE Trans. Microwave Theory Tech.**, vol. 49, pp. 151–159, Jan 2001.

[9] version 7.01 Zeland Software Inc, **Integral Equation 3D**, Fremont CA, 2000.

[10] Harold A Wheeler, "Fundamental limitations of small antennas," **Proceedings of the I.R.E**, vol. December, pp. 1479–1484, 1947.

[11] Henrik Holter, Tau-Haut Choi, and Daniel H Schaubert, "Eperimental results of 144-element dual-polarized endfire tapered-slot phased arrays," **IEEE Trans. Ant. and Prop.**, vol. 48, pp. 1707–1718, 2000.

[12] **Matlab, version 5.3.0**, The Mathworks, 2000.

[13] S. Saoudy and M. Hamid, "Rigorous solution of a dipole antenna with lumped impedance loading," **Canadian Journal of Physics**, vol. 64, pp. 1537–1545, March 1986.

[14] B. D. Popovic, "theory of frequency-independent impeadance-loaded thin conical antenna," **Journal of Engineering Physics**, May 1975.

[15] Constantine A. Balanis, **Antenna Theory**, p. 542, John Wiley & Sons, Inc, New York, 1982.

[16] Constantine A. Balanis, **Antenna Theory**, p. 135, John Wiley & Sons, Inc, New York, 1982.

[17] Carl Edwin Smith, **Log Periodic Antenna Design Handbook**, pp. 1–10, Smith Electronics, Cleveland, Ohio, 1966.

[18] Warren L. Stutzman and Gary A. Thiele, **Antenna Theory and Design**, pp. 259–270, John Wiley & Sons, Inc, New York, 1998.

[19] Branislave Notaros, B. D. Popovic, Robert Brown, and Zoya Popovic, "Large-domain MoM solution of complex electromagnetic problems," **IEEE MTT-S Int. Microwave Symp. Dig.**, pp. 1665–1669, June 1999.

[20] P. J. Gibson, "The Vivaldi aerial," **European Microwave Conf**, pp. 101–105, 1979.

[21] Elio A. Mariani, Charles P Heinzman, John P Agrios, and Seymour B Cohn, "Slot line charicteristics," **IEEE Trans. Microwave Theory Tech.**, vol. 17, pp. 1091–1096, 1969.

[22] M. M. Zinieris, R. Sload, and L. E. Davis, "A broadband microstrip-to-slot-line transition," **Microwave and Optical technology letters**, vol. 18, no. 5, pp. 339–342, August 1998.

[23] Ehud Gazit, "Improved design of the Vivaldi antenna," **IEE Procedings Part H**, vol. 135, no. 2, pp. 89–92, April 1988.

[24] R. Janasevamy, "Wiluer-hopf analyses of the asymmetric slotline," **Radio Science**, vol. 25, pp. 699–706, 1990.

[25] V. I Gvozdev, "Use of the unbalanced slotted line in shf microcircuits," **Radio Eng. Electron Physics**, vol. 27, pp. 42–47, 1982.

[26] V. I Gvozdev, "A nonsymmetrical slotted line, theory and experiment," **Soviet Journal Commum Technol Electron**, vol. 30, no. 9, pp. 49–56, 1985.

[27] A. Kuzayev, "Quasistatic model of a ribbed nonsymmetrical slotted line," **Radio Eng. Electron Physics**, vol. 28, no. 12, pp. 137–138, 1983.

[28] J. D. S. Langley, P.S Hall, and P. Newman, "Novel ultrawide-bandwidth vivaldi antenna with low crosspolarisation," **Electron. Lett.**, vol. 29, no. 23, pp. 2004–2005, November 1993.

[29] Sheldahl Materials, **Sheldahl Product Catalog**, Northfield, MN, 2000.

[30] J. H. B. Van Heuven, "A new integrated waveguide - microstrip transition," **IEEE Trans. Microwave Theory Tech.**, pp. 144–146, 1976.

[31] R. C. Hansen, **Phased Array Antennas**, pp. 215–272, John Wiley & Sons, Inc, New York, 1998.

[32] Merrill Ivan Skolnik, **Introduction to Radar Systems**, pp. 361–370, McGraw-Hill, New York, NY, 2001.

[33] David M. Pozar, **Microwave Engineering**, John Wiley & Sons, INC, New York, NY, 1998.

[34] H. Bosma, "On the theory of linear noisy systems," **Philips Research Reports Supplements**, , no. 10, pp. 1–189, 1967.

[35] Scott W. Wedge and David B Rutledge, "Wave techniques for noise modeling and measurement," **IEEE Trans. Microwave Theory Tech.**, vol. 40, no. 11, pp. 2004–2012, 1992.

[36] Philips Semiconductors, **Philips Internal Document**, Philips Semiconducators, Nijmegen The Netherlands, 1998.

[37] Scott William Wedge, **Computer-Aided Design of Low Noise Microwave Circuits**, Ph.D. thesis, California Institute of Technology, Pasadena, California, 1991.

APPENDIX A

VARIABLES USED IN CHAPTER 6

Variable	Name
i, m, l	integers
N	Size of Array
k_b	Boltzman's Constant
k	propogation Constant (1/m)
T	Temerature (Kelvin)
f	Frequency (Hz)
R	Resistance (ohms)
Z	Impedance (ohms)
h	Plank's Constnat
B	Band width (Hz)
a	Wave Variable (in going)
$\vec{a}$	Wave Vector (in going)
b	Wave Variable (out going)
$\vec{b}$	Wave Vector (out going)
P	Power
V	Voltage
$V_{+/-}$	Voltage wave in $(+/-)z$ direction
S	Scatering Matrix
$s_{i,l}$	element of S
E	Signal Power
NS	Noise Power (in Signal)
NF	Noise Figure
β	Phase
c	Noise Wave
c_i	Noise Wave at i-th port
c_i^c	Coupled Noise at i-th port
$C(t)$	RMS amplitude of Noise Wave

Table A.1: Variables used throughout chapter 6

Variable	Name
c_{tot}	Total Coupled Noise
c_{a1}	Noise wave at input of LNAs
c_{a2}	Noise wave at output of LNAs
$\vec{c}_{a1}$	Nx1 Noise Vector LNA input
$\vec{c}_{a2}$	Nx1 Noise Vector LNA output
$\vec{c}$	Noise Wave Vector
NCR	Noise Coupling Ration
G	Gain of LNA
Γ	Reflection Coefficient
$\Gamma(\phi, \theta)$	Scan Reflection Coefficient
Λ	Connection Matrix
λ	Eigenvalue
ϕ	Coordinate
θ	Coordinate
e	Natural Number
γ	Phase Shift Amplitude
ω	Angular Frequency
t	Time (seconds)
τ	Time (variable of integration)
COR_m	Noise Corolation of m-port
E	Exterior Port (sub script)
I	Interior Port (sub script)
Γ_{opt}	Optimal Noise Match
R_{min}	Noise Resistance
NF_{min}	Minimum Noise Figure

Table A.2: Variables used throughout chapter 6